

# Economic Geology

## Elevated magmatic sulfur and chlorine contents in ore-forming magmas at the Red Chris porphyry Cu-Au deposit, Northern British Columbia, Canada

--Manuscript Draft--

<b>Manuscript Number:</b>	SEG-D-18-00013R2
<b>Full Title:</b>	Elevated magmatic sulfur and chlorine contents in ore-forming magmas at the Red Chris porphyry Cu-Au deposit, Northern British Columbia, Canada
<b>Article Type:</b>	Regular Paper
<b>Corresponding Author:</b>	Jing-Jing Zhu, Ph.D Laurentian University Sudbury, Ontario CANADA
<b>Corresponding Author Secondary Information:</b>	
<b>Corresponding Author's Institution:</b>	Laurentian University
<b>Corresponding Author's Secondary Institution:</b>	
<b>First Author:</b>	Jing-Jing Zhu, Ph.D
<b>First Author Secondary Information:</b>	
<b>Order of Authors:</b>	Jing-Jing Zhu, Ph.D Jeremy Peter Richards Chris Rees Robert Creaser Andrew DuFrane Andrew Locock Joseph Petrus Jürgen Lang
<b>Order of Authors Secondary Information:</b>	
<b>Abstract:</b>	<p>The Red Chris porphyry Cu-Au deposit is located in the Stikinia island-arc terrane in northwest British Columbia. It is hosted by the Red Stock, which has four phases of porphyry intrusions: P1, P2E, P2L, and P3. New U-Pb dating of zircon shows that these intrusions were emplaced at <math>211.6 \pm 1.3</math> Ma (MSWD = 0.85), <math>206.0 \pm 1.2</math> Ma (MSWD = 1.5), <math>203.6 \pm 1.8</math> Ma (MSWD = 1.5), and <math>201.7 \pm 1.2</math> Ma (MSWD = 1.05), respectively. The ore-forming event at Red Chris was a short-lived event at <math>206.1 \pm 0.5</math> Ma (MSWD = 0.96; weighted average age of three Re-Os analyses), implying a duration of &lt;1 m.y., as defined by the uncertainty range. This mineralization age coincides with the emplacement age of the P2E porphyry, and is consistent with cross-cutting relationships that suggest P2E was the main syn-mineralization intrusion. Zircons from P1 to P3 porphyry rocks have consistently high EuN/EuN* ratios (mostly &gt; 0.4), indicating that their associated magmas were moderately oxidized. The magmatic water contents estimated from plagioclase and amphibole compositions suggest H<sub>2</sub>O contents of ~5 wt. %. Taken together, the P1 to P3 porphyries are interpreted to be moderately oxidized and hydrous.</p> <p>The four phases of porphyries are differentiated by sulfur and chlorine contents. The SO<sub>3</sub> contents of igneous apatite microphenocrysts from the mineralization-related P2 porphyries are higher (P2E: <math>0.30 \pm 0.13</math> wt. %, n = 34; P2L: <math>0.29 \pm 0.18</math> wt. %, n = 100) than those from the pre-mineralization P1 (<math>0.11 \pm 0.03</math> wt. %, n = 34) and post-mineralization P3 porphyries (<math>0.03 \pm 0.01</math> wt. %, n = 13). The chlorine contents in apatite grains from the P2E and P2L porphyries are <math>1.18 \pm 0.37</math> (n = 34) and <math>1.47 \pm 0.28</math> wt. % (n = 100), also higher than those from P1 (<math>0.51 \pm 0.3</math> wt. % Cl, n = 34) and P3 (<math>0.02 \pm 0.02</math> wt. % Cl, n = 17). These results imply that the sulfur and chlorine</p>

contents of the P2E and P2L magmas were higher than in the P1 and P3 magmas, suggesting that elevated magmatic S-Cl contents in the P2 porphyries may have been important for ore-formation. Although the process that caused the increase in sulfur and chlorine is not clear, reverse zoning seen in plagioclase phenocrysts from the P2 porphyry, and the occurrence of more mafic compositions in P2L suggest that recharge of the deeper magma chamber by a relatively S-Cl-rich mafic magma may have triggered the ore-forming hydrothermal event.

Dear Editor,

Thank you again for giving us the opportunity to improve our paper entitled “Elevated magmatic sulfur and chlorine contents in ore-forming magmas at the Red Chris porphyry Cu-Au deposit, Northern British Columbia, Canada” (ID: SEG-D-18-00013R1). Particularly, we appreciate the very careful review on this manuscript by the Associated Editor, David R. Cooke.

We agree with the comments by Dr. David Cooke and all the corresponding corrections have been done following his instructions. To facilitate review of our revised paper, the version with marked changes is given. We hope our manuscript could be accepted soon.

With thanks and regards,

Jing-Jing Zhu for the co-authors.

1  
2  
3  
4 **1 Elevated magmatic sulfur and chlorine contents in ore-forming magmas at the Red**  
5  
6 **2 Chris porphyry Cu-Au deposit, Northern British Columbia, Canada**

7  
8  
9 3 Jing-Jing Zhu<sup>1, 2, 3\*</sup>, Jeremy P. Richards<sup>1, 2</sup>, Chris Rees<sup>4</sup>, Robert Creaser<sup>2</sup>, S. Andrew  
10  
11 DuFrane<sup>2</sup>, Andrew Locock<sup>2</sup>, Joseph A. Petrus<sup>1</sup>, and Jürgen Lang<sup>2</sup>

12  
13  
14 5 <sup>1</sup> *Harquail School of Earth Sciences, Laurentian University, 935 Ramsey Lake Road,*  
15  
16 *Sudbury, ON, Canada P3E 2C6*

17  
18  
19 7 <sup>2</sup> *Department of Earth and Atmospheric Sciences, University of Alberta, Edmonton,*  
20  
21 *Alberta, Canada T6G 2E3*

22  
23  
24 9 <sup>3</sup> *State Key Laboratory of Ore Deposit Geochemistry, Institute of Geochemistry, Chinese*  
25  
26 *Academy of Sciences, Guiyang 550081, PR China*

27  
28  
29 11 <sup>4</sup> *Imperial Metals Corporation, 200-580 Hornby Street, Vancouver, B.C., Canada V6C*  
30  
31 *3B6*

32  
33  
34  
35  
36 13 *\*Corresponding author e-mail: [jzhu4@laurentian.ca](mailto:jzhu4@laurentian.ca); [zhujingjing-1103@163.com](mailto:zhujingjing-1103@163.com)*

37  
38  
39 **14 Abstract**

40  
41  
42 15 The Red Chris porphyry Cu-Au deposit is located in the Stikinia island-arc terrane in  
43  
44 16 northwest British Columbia. It is hosted by the Red Stock, which has four phases of  
45  
46 17 porphyry intrusions: P1, P2E, P2L, and P3. New U-Pb dating of zircon shows that these  
47  
48 18 intrusions were emplaced at  $211.6 \pm 1.3$  Ma (MSWD = 0.85),  $206.0 \pm 1.2$  Ma (MSWD =  
49  
50 19  $1.5$ ),  $203.6 \pm 1.8$  Ma (MSWD = 1.5), and  $201.7 \pm 1.2$  Ma (MSWD = 1.05), respectively.  
51  
52 20 The ore-forming event at Red Chris was a short-lived event at  $206.1 \pm 0.5$  Ma (MSWD =  
53  
54 21  $0.96$ ; weighted average age of three Re-Os analyses), implying a duration of <1 m.y., as  
55  
56 22 defined by the uncertainty range. This mineralization age coincides with the emplacement  
57  
58  
59  
60  
61  
62  
63  
64  
65

1  
2  
3  
4 23 age of the P2E porphyry, and is consistent with cross-cutting relationships that suggest  
5  
6  
7 24 P2E was the main syn-mineralization intrusion.

8  
9 25 Zircons from P1 to P3 porphyry rocks have consistently high  $\text{Eu}_N/\text{Eu}_N^*$  ratios (mostly >  
10  
11 26 0.4), indicating that their associated magmas were moderately oxidized. The magmatic  
12  
13  
14 27 water contents estimated from plagioclase and amphibole compositions suggest  $\text{H}_2\text{O}$   
15  
16 28 contents of ~5 wt. %. Taken together, the P1 to P3 porphyries are interpreted to be  
17  
18  
19 29 moderately oxidized and hydrous.

20  
21 30 The four phases of porphyries are differentiated by sulfur and chlorine contents. The  
22  
23  
24 31  $\text{SO}_3$  contents of igneous apatite microphenocrysts from the mineralization-related P2  
25  
26 32 porphyries are higher (P2E:  $0.30 \pm 0.13$  wt. %,  $n = 34$ ; P2L:  $0.29 \pm 0.18$  wt. %,  $n = 100$ )  
27  
28  
29 33 than those from the pre-mineralization P1 ( $0.11 \pm 0.03$  wt. %,  $n = 34$ ) and post-  
30  
31 34 mineralization P3 porphyries ( $0.03 \pm 0.01$  wt. %,  $n = 13$ ). The chlorine contents in apatite  
32  
33 35 grains from the P2E and P2L porphyries are  $1.18 \pm 0.37$  ( $n = 34$ ) and  $1.47 \pm 0.28$  wt. %  
34  
35 36 ( $n = 100$ ), also higher than those from P1 ( $0.51 \pm 0.3$  wt. % Cl,  $n = 34$ ) and P3 ( $0.02 \pm$   
36  
37 37  $0.02$  wt. % Cl,  $n = 17$ ). These results imply that the sulfur and chlorine contents of the  
38  
39  
40 38 P2E and P2L magmas were higher than in the P1 and P3 magmas, suggesting that  
41  
42  
43 39 elevated magmatic S-Cl contents in the P2 porphyries may have been important for ore-  
44  
45 40 formation. Although the process that caused the increase in sulfur and chlorine is not  
46  
47  
48 41 clear, reverse zoning seen in plagioclase phenocrysts from the P2 porphyry, and the  
49  
50  
51 42 occurrence of more mafic compositions in P2L suggest that recharge of the deeper  
52  
53 43 magma chamber by a relatively S-Cl-rich mafic magma may have triggered the ore-  
54  
55 44 forming hydrothermal event.

56  
57  
58 45

1  
2  
3  
4  
5  
6  
7  
8  
9  
10  
11  
12  
13  
14  
15  
16  
17  
18  
19  
20  
21  
22  
23  
24  
25  
26  
27  
28  
29  
30  
31  
32  
33  
34  
35  
36  
37  
38  
39  
40  
41  
42  
43  
44  
45  
46  
47  
48  
49  
50  
51  
52  
53  
54  
55  
56  
57  
58  
59  
60  
61  
62  
63  
64  
65

## Introduction

46  
47 Compared to the relatively long-lived magmatic systems represented by a composite  
48 batholith (up to 10 m.y.; Matzel et al., 2006; Walker et al., 2007; Harris et al., 2008;  
49 Schaltegger et al., 2009; Paterson et al., 2011; Rezeau et al., 2016), the life spans of  
50 porphyry magmatic-hydrothermal ore-forming events are much shorter, probably on the  
51 order of several hundred thousand years (up to 1 m.y.; Cathles et al., 1997; Hayba and  
52 Ingebritsen, 1997; Masterman et al., 2004; von Quadt et al., 2011; Weis et al., 2012;  
53 Chiaradia et al., 2013; Correa et al., 2016; Li et al., 2017). In many large magmatic  
54 systems, porphyry formation occurs at a relatively late stage in the system's evolution  
55 (Creasey, 1977; Titley and Beane, 1981; Candela, 1992; Richards, 2003; Rohrlach and  
56 Loucks, 2005; Yang et al., 2009; Correa et al., 2016).

57 Although the multiple phases of porphyry stocks are commonly broadly cogenetic,  
58 they may be derived from packets of magma that evolved at different crustal levels over  
59 the history of the larger magmatic system (Annen et al., 2006). Understanding why ore-  
60 formation is only associated with a specific intrusive suite within these broader systems,  
61 and at discrete, commonly singular times, is a focus of this study.

62 It is recognized that magmas with high sulfur (>1000 ppm), chlorine (>3000 ppm),  
63 and water (>4 wt. %) contents as well as relatively high oxidation states (higher than the  
64 fayalite-magnetite-quartz buffer,  $\Delta\text{FMQ}$ , by 1–2 log  $f\text{O}_2$  units) are fertile for the  
65 generation of magmatic-hydrothermal porphyry Cu deposits (Burnham, 1979; Candela,  
66 1992; Richards, 2003, 2009, 2011, 2015; Wallace, 2005; Chambefort et al., 2008; Simon  
67 and Ripley, 2011; Chiaradia et al., 2012; Loucks, 2014; Hou et al., 2015; Lu et al., 2015,  
68 2016; Chelle-Michou and Chiaradia, 2017). These ingredients are essential for the

1  
2  
3  
4 69 transport of Cu (and Au) both in the magma (Zajacz et al., 2012) and in exsolved high  
5  
6 70 temperature, SO<sub>2</sub>-rich, saline magmatic fluids (Candela and Holland, 1984; Zajacz et al.,  
7  
8  
9 71 2011). However, whereas many magmas achieve such compositions, ore formation is a  
10  
11 72 relatively rare and discrete event in such systems.

13  
14 73 Various mechanisms have been proposed that might trigger an ore forming event  
15  
16 74 from a fertile magma source, including recharge of the magma chamber by hot, sulfur-  
17  
18 75 rich melts (Hattori, 1993; Keith et al., 1997; Larocque et al., 2000; Hattori and Keith,  
19  
20  
21 76 2001; Halter et al., 2005; Stern et al., 2007; Nadeau et al., 2010, 2016; Wilkinson, 2013;  
22  
23 77 Tapster et al., 2016; Zhang and Audétat, 2017), fluxing by sulfur gases (Blundy et al.,  
24  
25  
26 78 2015), or increasing the water and oxidation state of magmas during long-term  
27  
28 79 fractionation in deep magma chambers (Ballard et al., 2002; Wang et al., 2014a, 2014b;  
29  
30  
31 80 Dilles et al., 2015; Lu et al., 2015, 2016). The Red Chris porphyry Cu-Au deposit  
32  
33 81 provides an opportunity to test these hypotheses, because ore-formation occurred at a  
34  
35  
36 82 discrete and relatively late stage in the ~10 m.y. history of the associated magmatic  
37  
38 83 system.

39  
40  
41 84 The Red Chris deposit is located in northwest British Columbia, and contains  
42  
43 85 measured and indicated resources of 1,035 million metric tonnes of ore grading 0.35%  
44  
45 86 Cu and 0.35 g/t Au (Gillstrom et al., 2012). Pre-, syn-, and post-mineralization porphyry  
46  
47  
48 87 intrusions have been recognized based on detailed core logging and petrographic work  
49  
50  
51 88 (Rees et al., 2015), with mineralization occurring in a singular episode during this  
52  
53 89 magmatic history. In this paper, we present detailed geochronological and geochemical  
54  
55 90 data for the porphyry phases at Red Chris, and show that they have similar bulk  
56  
57  
58 91 compositions, including all being relatively hydrous and oxidized. However, the syn-

1  
2  
3  
4 92 mineralization porphyry is characterized by plagioclase with reverse zoning and apatite  
5  
6  
7 93 with relatively high sulfur and chlorine contents. We interpret these data to indicate that  
8  
9  
10 94 high magmatic S and Cl contents, in addition to high H<sub>2</sub>O contents and oxidation state,  
11  
12 95 were critical for Cu-Au ore-formation at Red Chris. We speculate that there was an  
13  
14 96 injection of relatively mafic (hotter, and more S- and Cl-rich) but cogenetic magma into  
15  
16 97 the mid–upper crustal source magma chamber approximately coincident with  
17  
18  
19 98 emplacement of the syn-mineralization porphyry.  
20  
21 99

## 23 100 **Geological Setting**

27 101 Red Chris is situated within the island-arc terrane of Stikinia in the Intermontane Belt  
28  
29 102 of the Canadian Cordillera of British Columbia (Fig. 1; Monger and Irving, 1980; Nelson  
30  
31 103 and Colpron, 2007; Nelson et al., 2013). Stikinia consists primarily of Mesozoic arc-  
32  
33 104 related igneous and sedimentary rocks, formed in response to subduction processes prior  
34  
35 105 to accretion to the ancestral North American margin in the Middle Jurassic (Gabrielse,  
36  
37 106 1991; Ricketts et al., 1992; Lang et al., 1995; Mihalynuk et al., 2004; Nelson and Colpron,  
38  
39 107 2007; Logan and Mihalynuk, 2014). In northwestern Stikinia, arc assemblages comprise  
40  
41 108 the Middle to Late Triassic Stuhini Group, unconformably overlain by Late Triassic and  
42  
43 109 Early to Middle Jurassic volcanic and sedimentary rocks of the Hazelton Group (Fig. 2;  
44  
45 110 Brown et al., 1991; Gabrielse, 1991; Marsden and Thorkelson, 1992; Dostal et al., 1999;  
46  
47 111 Gagnon et al., 2012; Nelson et al., 2013; Logan and Mihalynuk, 2014). The Hazelton  
48  
49 112 Group is overlain by sedimentary rocks of the syn- to post-accretion Middle Jurassic to  
50  
51 113 Early Cretaceous Bowser Lake Group.  
52  
53  
54  
55  
56  
57  
58  
59  
60  
61  
62  
63  
64  
65



1  
2  
3  
4 114 Several porphyry Cu±Au±Mo deposits occur in the region, hosted by Late Triassic to  
5  
6  
7 115 Early Jurassic arc-related plutons (Fig. 1), including Red Chris which formed in the Late  
8  
9 116 Triassic Red Stock. Collectively, these regional intrusions have ages ranging from ~222  
10  
11 117 Ma to ~180 Ma, recording much of the pre-accretionary history of Stikinia (Lang et al.,  
12  
13 118 1995; McMillan et al., 1995; Scott et al., 2008; Nelson et al., 2013; Logan and Mihalynuk,  
14  
15 119 2014). A significant percentage of the known porphyry Cu deposits, including Red Chris,  
16  
17 120 formed during a 6-m.y. pulse of magmatism between 206 and 200 Ma, with compositions  
18  
19 121 ranging from calc-alkaline to strongly alkaline (Lang et al., 1995; McMillan et al., 1995;  
20  
21 122 Nelson et al., 2013; Bissig and Cooke, 2014; Logan and Mihalynuk, 2014; Micko et al.,  
22  
23 123 2014; Pass et al., 2014).  
24  
25  
26  
27  
28  
29  
30 124  
31  
32

### 125 **Geology of the Red Chris Cu-Au deposit**

33  
34  
35  
36 126 The Red Chris Cu-Au deposit was discovered in the 1950s and explored  
37  
38 127 intermittently in subsequent decades, with mining beginning in 2015 (Ash et al., 1995,  
39  
40 128 1996; Newell and Peatfield, 1995; Baker et al., 1997; Gillstrom et al., 2012; Rees et al.,  
41  
42 129 2015). The deposit is hosted by the Red Stock, which is the largest of a suite of Late  
43  
44 130 Triassic to Early Jurassic stocks and dikes that intrude the Stuhini Group in the district  
45  
46 131 (Fig. 2; Friedman and Ash, 1997; Rees et al., 2015). The stock is tabular, elongate in an  
47  
48 132 east to northeast direction, and approximately 6.5 km long by 300 to 1500 m wide (Fig. 2;  
49  
50 133 Ash et al., 1995; Baker et al., 1997; Gillstrom et al., 2012). It has a steep northern contact  
51  
52 134 against Stuhini Group country rocks, but its southeastern margin against Hazelton and  
53  
54 135 Bowser Lake Group strata is poorly exposed, and has locally been truncated by the NE-  
55  
56  
57  
58  
59  
60  
61  
62  
63  
64  
65

1  
2  
3  
4 136 trending, steeply SE-dipping South Boundary fault (Fig. 2). This fault, and the East zone  
5  
6 137 fault within the stock, probably reflect a long-lived and deep structure which guided the  
7  
8  
9 138 emplacement of the intrusions, mineralization, and subsequent deformation of the Red  
10  
11 139 Stock.

14  
15 140 The Red Stock is a composite intrusion consisting of several phases of porphyritic  
16  
17 141 diorite to quartz monzonite. Mineralogically, the rocks consist of medium- to coarse-  
18  
19 142 grained amphibole, plagioclase, and minor biotite phenocrysts, with K-feldspar,  
20  
21  
22 143 plagioclase, and quartz in the groundmass. Based on compositional and textural  
23  
24 144 differences and crosscutting relationships, Rees et al. (2015) identified four distinct  
25  
26 145 porphyry phases, P1, P2, P3, and P4. The P1 porphyry is a pre-mineralization  
27  
28 146 leucodiorite which accounts for the main volume of the Red Stock, and is distinguished  
29  
30 147 by sparse anhedral to subhedral amphibole (~10%) and abundant plagioclase (30–40  
31  
32 148 vol. %) phenocrysts with lengths up to 4 mm. The groundmass is composed of fine-  
33  
34  
35 149 grained plagioclase and minor quartz (Fig. 3A).

36  
37  
38  
39  
40 150 The P2 porphyry is a syn-mineralization quartz monzonite intrusion which is largely  
41  
42 151 unexposed at surface but is observed in drill core to have intruded P1 at depth. It has been  
43  
44 152 subdivided by Rees et al. (2015) into early (P2E), intermediate (P2I), and late (P2L)  
45  
46 153 phases based on vein truncations and chilled margins. The P2 porphyries are generally  
47  
48 154 characterized by tabular subhedral to euhedral amphibole (10–15 vol. %) and plagioclase  
49  
50 155 (35–50 vol. %) phenocrysts. The amphibole crystals are mostly euhedral and larger than  
51  
52 156 in P1, with lengths up to 10 mm. The groundmass comprises K-feldspar, plagioclase, and  
53  
54  
55 157 quartz. In this paper, the P2 subphases are simplified to an early stage (P2E; Fig. 3B) and  
56  
57  
58 158 late stage porphyry (P2L, probably corresponding to P2I and P2L of Rees et al., 2015;  
59  
60  
61  
62  
63  
64  
65

1  
2  
3  
4 159 Fig. 3C). The P2E porphyry has a crowded plagioclase texture with slightly smaller  
5  
6 160 amphibole phenocrysts than P2L. In contrast, the P2L porphyry is relatively fresh and  
7  
8  
9 161 occurs only as small dikes (Fig. 4).

10  
11  
12 162 The post-mineralization P3 monzonite porphyry is much less abundant. It is texturally  
13  
14  
15 163 similar to the P2L porphyry with abundant amphibole phenocrysts (15–20 vol. %), but is  
16  
17 164 distinguished by the absence of quartz in the groundmass, which is mainly composed of  
18  
19  
20 165 K-feldspar and plagioclase (Fig. 3D). Although no crosscutting relationships between the  
21  
22 166 P3 and P2L porphyries have been found, the zircon U-Pb dating results (see below)  
23  
24  
25 167 confirm that P3 is younger. The P4 porphyry occurs as rare dikes and is typified by  
26  
27 168 sparse fine-grained amphibole phenocrysts (Rees et al., 2015). No P4 samples were  
28  
29  
30 169 included in this study.

31  
32  
33 170 Several younger basaltic to andesitic dikes with sparse amphibole phenocrysts cut the  
34  
35 171 Red Stock and the Stuhini Group host rocks (Figs. 3E and F). They postdate the  
36  
37  
38 172 porphyry-stage Cu-Au mineralization (Baker et al., 1997; Rees et al., 2015), but are  
39  
40 173 mildly to strongly altered (Figs. 3E and F) and are crosscut by late quartz-calcite-pyrite  
41  
42  
43 174 veins.

#### 44 45 175 *Hydrothermal alteration*

46  
47  
48  
49 176 Alteration at Red Chris has been described previously by Baker et al. (1997),  
50  
51 177 Gillstrom et al. (2012), Norris (2012) and Rees et al. (2015). The alteration assemblages  
52  
53  
54 178 are typical of calc-alkaline porphyry Cu systems (Lowell and Guilbert, 1970; Seedorff et  
55  
56  
57 179 al., 2005; Sillitoe, 2010), and consists of early stage potassic alteration, overprinted by  
58  
59 180 chlorite–sericite, sericitic (phyllic), intermediate argillic, and minor late stage propylitic

1  
2  
3  
4 181 alteration (see paragenetic diagram in Rees et al., 2015). Potassic alteration is expressed  
5  
6 182 by replacement of amphibole phenocrysts by secondary biotite, plagioclase replaced or  
7  
8  
9 183 rimmed by secondary K-feldspar, and by K-feldspar veins (Figs. 3B and 5A–C). It is best  
10  
11 184 preserved in the deeper levels of the deposit where it is spatially associated with the syn-  
12  
13  
14 185 mineralization P2E porphyry; however it locally extends into pre-mineralization P1  
15  
16 186 porphyry wall rocks (Fig. 4). The P2L and P3 porphyries were only weakly affected by  
17  
18  
19 187 potassic alteration (Rees et al., 2015).  
20  
21

22 188 Chlorite–sericite alteration is characterized by chlorite replacing secondary biotite  
23  
24 189 (Fig. 5C) and sericite replacing feldspar (Fig. 5D). At shallower levels in the system,  
25  
26  
27 190 potassic alteration is completely overprinted by phyllic and intermediate argillic  
28  
29 191 alteration (Gillstrom et al., 2012), characterized by sericite after plagioclase (phyllic; Fig.  
30  
31  
32 192 5D), and illite and kaolinite (intermediate argillic; Norris, 2012). This lower temperature  
33  
34 193 alteration overprint affects all the porphyry phases, but is less pervasive at depth.  
35  
36

37  
38 194 Propylitic alteration at Red Chris is mainly observed as minor chlorite and epidote in  
39  
40 195 the outer part of the Red Stock, and extends for 100 to 200 m into the Stuhini volcanic  
41  
42 196 country rocks (Gillstrom et al., 2012; Norris, 2012; Rees et al., 2015).  
43  
44

#### 45 197 *Vein styles and mineralization*

46  
47  
48

49 198 Detailed descriptions of vein styles at Red Chris have been given by Norris (2012)  
50  
51 199 and Rees et al. (2015). A-type quartz veins (Gustafson and Hunt, 1975) and stockworks  
52  
53 200 are associated with potassic alteration and host the bulk of the copper-gold mineralization.  
54  
55  
56 201 These veins are most intensely developed around the apex of the principal P2 porphyry  
57  
58  
59 202 body, but extend for hundreds of metres into the P1 wall rocks. Typical A veins contain  
60  
61  
62  
63  
64  
65

1  
2  
3  
4 203 K-feldspar, biotite, chalcopyrite, bornite, and magnetite, with K-feldspar alteration halos  
5  
6 204 (Figs. 5A–B and G). Copper sulfides also occur as disseminations in the host porphyry.  
7  
8  
9 205 Bornite is more abundant in the apex of P2E, and progressively decreases outwards  
10  
11 206 where chalcopyrite is the dominant Cu-sulfide (Norris, 2012; Rees et al., 2015). At  
12  
13 207 shallower depths in the preserved system, early bornite was sulfidized to chalcopyrite,  
14  
15 208 and pyrite becomes increasingly dominant. Rees et al. (2015) delineated a high-sulfur  
16  
17 209 contour (>4% S) in section above which total sulfide (dominantly pyrite) ranges from 4 to  
18  
19 210 10%. Microscopic native gold and electrum occur as inclusions in bornite (Rees et al.,  
20  
21 211 2015). The grades of Cu and Au are positively correlated with quartz vein density  
22  
23 212 (Gillstrom et al., 2012). In high-grade zones at depth (e.g., 4.12 % Cu and 8.83 g/t Au in  
24  
25 213 hole 09-350 from 540 to 692.5 m down-hole depth), vein abundance exceeds 80 vol. % in  
26  
27 214 sheeted arrays (Fig. 5G; Rees et al., 2015).  
28  
29  
30  
31  
32  
33

34 215 B- and D-type veins (Gustafson and Hunt, 1975) are relatively minor at Red Chris,  
35  
36 216 and host only minor amounts of Cu sulfides. B quartz veins are characterized by  
37  
38 217 relatively straight margins with sulfide centerlines (pyrite and minor chalcopyrite, and  
39  
40 218 locally molybdenite; Fig. 5E). Pyritic D veins have variable widths (1 to 10 mm; Fig. 5F).  
41  
42 219 Carbonate and minor chlorite veins cut all the earlier veins and are generally barren  
43  
44 220 (Norris, 2012).  
45  
46  
47  
48  
49

## 221 **Sampling and Analytical Methods**

50  
51  
52 222 Samples of the P1, P2E, P2L, and P3 porphyries were collected from drill core, and  
53  
54 223 descriptions and locations are listed in Digital Appendix Table A1; sampled drill hole  
55  
56 224 locations are also shown on Figure 2. Fourteen least-altered samples of the porphyry  
57  
58 225 intrusions and three samples of late basaltic to andesitic dikes were selected for whole-  
59  
60  
61  
62  
63  
64  
65

1  
2  
3  
4 226 rock geochemical analysis. Eight of these samples were selected for determination of Nd-  
5  
6 227 Sr isotopes. Three samples of quartz-carbonate-pyrite-molybdenite-chalcopyrite veins  
7  
8  
9 228 (Fig. 5H) were collected for Re-Os dating. Four samples of the P1 (RC13-40), P2E  
10  
11 229 (RC13-107), P2L (RC13-33), and P3 (RC13-78) intrusions were selected for zircon U-Pb  
12  
13  
14 230 dating, Hf isotopic, and trace element analyses. Details of analytical methods are  
15  
16 231 provided in Appendix 1.  
17  
18  
19 232

20  
21 233 *Electron microprobe analyses*  
22

23  
24 234 Primary igneous minerals such as plagioclase and amphibole in the porphyry rocks  
25  
26 235 are widely altered to K-feldspar, sericite, and chlorite (Figs. 3A–B and 5C–D). However,  
27  
28 236 a few least-altered samples of the P2E, P2L, and P3 porphyries contained unaltered  
29  
30  
31 237 plagioclase and amphibole grains. In addition, igneous apatite grains were typically  
32  
33 238 preserved as inclusions within plagioclase and amphibole phenocrysts. Compared with  
34  
35  
36 239 hydrothermal apatite (acicular crystals intergrown with other hydrothermal minerals such  
37  
38 240 as quartz, sericite, chlorite, and sulfides), igneous apatite grains typically showed stubby  
39  
40  
41 241 prismatic habits, as described by Richards et al. (2017). Detailed analytical methods are  
42  
43 242 described in Appendix 1.  
44  
45  
46 243

47  
48 244 *Re-Os molybdenite dating*  
49

50  
51 245 Three samples of molybdenite from quartz-carbonate-pyrite-molybdenite-chalcopyrite  
52  
53 246 veins were collected from the Gully zone (RC13-88 and RC13-103), and the East zone  
54  
55 247 (RC13-82; Digital Appendix Table A1; Fig. 2). A molybdenite mineral separate was  
56  
57  
58 248 produced for each sample by metal-free crushing followed by gravity and magnetic  
59  
60  
61  
62  
63  
64  
65

1  
2  
3  
4 249 concentration methods. Dating was conducted at the Canadian Centre for Isotopic  
5  
6  
7 250 Microanalysis at the University of Alberta, Canada, using methods described in  
8  
9 251 Appendix 1.

10  
11 252

12  
13  
14 253

## Geochronological Results

15  
16 254 *Zircon U-Pb ages of the Red Stock*

17  
18  
19 255 Zircon U-Pb results are presented in Digital Appendix Table A2 and illustrated in  
20  
21 256 Figure 6; all ages are illustrated and reported with  $2\sigma$  errors. All the zircons show  
22  
23  
24 257 oscillatory zoning under BSE imaging. Sample RC13-40 was collected from P1  
25  
26 258 leucodiorite porphyry (Digital Appendix Table A1). Analyzed zircon grains form a  
27  
28  
29 259 tightly clustered age population, mostly with low common lead contents. Except for one  
30  
31 260 inherited or xenocryst zircon (apparent  $^{206}\text{Pb}/^{238}\text{U}$  age =  $261 \pm 12$  Ma), the twenty-seven  
32  
33  
34 261 grains yielded an intercept age of  $211.6 \pm 1.3$  Ma (MSWD = 0.85; Fig. 6A), similar to the  
35  
36 262 weighted mean  $^{206}\text{Pb}/^{238}\text{U}$  age of  $211.8 \pm 1.3$  Ma (MSWD = 0.8).

37  
38 263 Sample RC13-107 was collected from P2E quartz monzonite porphyry (Digital  
39  
40  
41 264 Appendix Table A1). One xenocrystic zircon grain yielded an older age (apparent  
42  
43 265  $^{206}\text{Pb}/^{238}\text{U}$  age =  $316 \pm 10$  Ma), but the other twenty-nine zircons contained low amounts  
44  
45  
46 266 of common lead and intersected the concordia line at  $206.0 \pm 1.2$  Ma (MSWD = 1.5; Fig.  
47  
48 267 6B), in good agreement with the weighted mean  $^{206}\text{Pb}/^{238}\text{U}$  age of  $205.9 \pm 1.5$  Ma  
49  
50  
51 268 (MSWD = 1.5).

52  
53 269 Sample RC13-33 was collected from P2L quartz monzonite porphyry (Digital  
54  
55  
56 270 Appendix Table A1). Two xenocryst grains were found among thirty-one analyzed  
57  
58 271 zircons, with  $^{206}\text{Pb}/^{238}\text{U}$  ages of  $298 \pm 16$  Ma and  $441 \pm 13$  Ma. The remaining twenty-

1  
2  
3  
4 272 nine zircon grains had low common lead contents and yielded an intercept age of  $203.6 \pm$   
5  
6 273  $1.8$  Ma (MSWD = 1.5; Fig. 6C), similar to the weighted mean  $^{206}\text{Pb}/^{238}\text{U}$  age of  $203.3 \pm$   
7  
8  
9 274  $1.5$  Ma (MSWD = 1.04).

10  
11 275 Sample RC13-78 was collected from P3 monzonite porphyry (Digital Appendix Table  
12  
13 276 A1). Thirty-two zircons with low common lead contents yielded an intercept age of  $201.7$   
14  
15  
16 277  $\pm 1.2$  Ma (MSWD = 1.05; Fig. 6D), and a weighted mean  $^{206}\text{Pb}/^{238}\text{U}$  age of  $201.6 \pm 1.2$   
17  
18 278 Ma (MSWD = 1.04).

19  
20 279 All of the zircons have magmatic textures, and the intercept ages above are interpreted  
21  
22  
23 280 to be the crystallization ages of the individual intrusions. The ages are consistent with  
24  
25  
26 281 crosscutting relationships described by Rees et al. (2015), and define a 10 m.y. span of  
27  
28  
29 282 magmatism from  $211.6 \pm 1.3$  Ma (P1) to  $201.7 \pm 1.2$  Ma (P3). The relative ages of the  
30  
31 283 two samples of syn-mineralization P2 porphyry are consistent with crosscutting  
32  
33 284 relationships, but the dates (P2E:  $206.0 \pm 1.2$  Ma; P2L:  $203.6 \pm 1.8$  Ma) overlap within  
34  
35  
36 285 the  $2\sigma$  uncertainty. Hence the apparent 2.4 m.y. age difference is not statistically robust,  
37  
38  
39 286 and their true ages may in fact be closer as suggested by their close relationship with ore  
40  
41 287 mineral paragenesis.

42  
43 288

44  
45 289 *Re-Os molybdenite ages*

46  
47  
48 290 The Re-Os model ages for three samples are shown in Table 1. They have relatively  
49  
50  
51 291 high rhenium contents ranging from 497.8 to 1771 ppm, with common  $^{187}\text{Os}$  of 1078 to  
52  
53 292 3821 ppb. Although the three samples are from two different mineralization zones (i.e.,  
54  
55  
56 293 East and Gully zones; Fig. 2), they yielded indistinguishable model ages within  
57  
58 294 uncertainty:  $206.5 \pm 0.8$  Ma,  $205.7 \pm 0.9$  Ma, and  $205.9 \pm 1.1$  Ma ( $\pm 2$  s.d.). The small  
59  
60  
61  
62  
63  
64  
65



1  
2  
3  
4 295 grain size of the molybdenite (< 1 mm) minimizes the risk of decoupling between Re and  
5  
6 296 <sup>187</sup>Os in these samples (caused by diffusion: Selby and Creaser, 2004). The results  
7  
8  
9 297 yielded a weighted average age for all three samples of 206.1 ± 0.5 Ma (95% confidence  
10  
11 298 level with MSWD = 0.96; Fig. 7). This age is consistent with the age of the syn-  
12  
13  
14 299 mineralization P2E porphyry (206.0 ± 1.2 Ma).  
15

16 300

## 19 301 **Geochemical and Isotopic Results**

### 21 302 *Whole-rock major and trace elements*

23 303 Whole-rock major and trace element compositions for fourteen samples of the Red  
24  
25 304 Stock and three basaltic–andesitic dike samples are listed in Table 2. All the P1 to P3  
26  
27 305 porphyry intrusions have relatively homogeneous major element compositions, but have  
28  
29 306 moderate to high loss-on-ignition values (LOI: 2.3 to 10.9%) reflecting varying degrees  
30  
31 307 of potassic and sericitic alteration. On an LOI-free basis, they are mostly intermediate  
32  
33 308 composition (SiO<sub>2</sub> = 56.71–63.16 wt. %; Digital Appendix Table A3), and straddle the  
34  
35 309 boundary between granodiorite (diorite) and syenite on a Zr/Ti versus Nb/Y diagram (Fig.  
36  
37 310 8). The late basaltic–andesitic dikes have distinct compositions, and plot in the field of  
38  
39 311 diorite and gabbro on Figure 8. On Harker-type diagrams of SiO<sub>2</sub> versus selected major  
40  
41 312 elements, the alkali elements (K<sub>2</sub>O and Na<sub>2</sub>O; Figs. 9A–B) show significant scatter,  
42  
43 313 likely due to hydrothermal alteration, as confirmed by a rough correlation between alkali  
44  
45 314 contents and LOI. However, other elements such as Fe<sub>2</sub>O<sub>3</sub>, MgO, TiO<sub>2</sub>, and Al<sub>2</sub>O<sub>3</sub> show  
46  
47 315 roughly correlated trends with SiO<sub>2</sub> (Figs. 9E–F), suggesting a broadly cogenetic suite,  
48  
49 316 with the exception of the late basaltic to andesitic dikes, which do not plot on the same  
50  
51 317 trends for K<sub>2</sub>O and TiO<sub>2</sub>.  
52  
53  
54  
55  
56  
57  
58  
59  
60  
61  
62  
63  
64  
65

1  
2  
3  
4 318 On primitive mantle-normalized extended trace element and chondrite-normalized  
5  
6 319 rare earth element (REE) diagrams (Figs. 10A–B), the porphyritic rocks show largely  
7  
8  
9 320 indistinguishable patterns consistent with typical subduction-related igneous rocks  
10  
11 321 (Hawkesworth et al., 1993; Pearce, 1996), characterized by large-ion lithophile element  
12  
13 322 (LILEs: Rb, Ba, Th, U, K) and light rare earth element enrichments (LREE), low  
14  
15 323 concentrations of high field strength elements (HFSE: Nb, Ta, Zr, Hf, and Ti), relative  
16  
17 324 depletions in compatible elements and middle to heavy rare earth elements (MREE,  
18  
19 325 HREE; La/Yb =  $8.9 \pm 1.7$ , n = 14), and flat to listric-shaped patterns from MREE to  
20  
21 326 HREE. Such listric patterns likely reflect amphibole fractionation from hydrous magmas,  
22  
23 327 and are an indication of magma fertility for porphyry ore formation (Richards and  
24  
25 328 Kerrich, 2007). Most samples have flat or slightly positive Eu anomalies with  $Eu_N/Eu_N^*$   
26  
27 329 of  $1.1 \pm 0.15$  (n = 14; Fig. 10B), also likely reflecting amphibole fractionation and lack of  
28  
29 330 plagioclase fractionation.

30  
31  
32  
33  
34  
35  
36 331 Three samples of late basaltic to andesitic dikes show distinct trace element patterns,  
37  
38 332 especially for HFSE and REE, which are enriched relative to the porphyries; they are  
39  
40 333 clearly not cogenetic with the earlier porphyries.

41  
42  
43 334 Excluding two samples with high Sr values that may reflect calcite veining, the  
44  
45 335 porphyries have relatively high Sr/Y ( $53 \pm 23$ , n = 12) and V/Sc ratios ( $9.0 \pm 0.9$ , n = 14),  
46  
47 336 which overlap the range of fertile rocks for porphyry formation (Richards and Kerrich,  
48  
49 337 2007; Loucks, 2013, 2014).

50  
51  
52  
53 338

54  
55 339 *Whole-rock Nd-Sr isotopes*  
56  
57  
58  
59  
60  
61  
62  
63  
64  
65

1  
2  
3  
4 340 Nd and Sr isotopic compositions of the porphyritic rocks are very homogeneous (Table  
5  
6 341 4 and Fig. 11). They show a narrow range of initial Sr isotopic ratios from 0.7042 to  
7  
8 342 0.7047 ( $(^{87}\text{Sr}/^{86}\text{Sr})_t = 0.7044 \pm 0.0002$ ,  $n = 8$ ), with relatively high  $\epsilon_{\text{Nd}}(t)$  values from 2.4  
9  
10 343 to 3.6 (average =  $+3.1 \pm 0.4$ ,  $n = 8$ ), consistent with a mantle source with minor crustal  
11  
12 344 contamination. The single-stage Nd model ages ( $T_{\text{DM1}}$ ) calculated following the methods  
13  
14 345 of Goldstein et al. (1984) range from 0.74 to 0.88 Ga (average =  $0.80 \pm 0.05$  Ga,  $n = 8$ ),  
15  
16 346 and are indistinguishable for the different porphyry phases. Two basaltic–andesitic dike  
17  
18 347 samples show slightly lower Sr isotopic ratios ( $(^{87}\text{Sr}/^{86}\text{Sr})_t = 0.7042$  and  $0.7043$ ) and  
19  
20 348 higher  $\epsilon_{\text{Nd}}(t)$  ratios ( $+3.5$  and  $+3.9$ ) than the porphyry rocks (Fig. 11).  
21  
22  
23  
24  
25  
26

#### 27 *Zircon Hf isotopes*

28  
29 350 Zircon Hf isotopic results are listed in Digital Appendix Table A4, and illustrated in  
30  
31 351 Figure 12. The four zircon samples from porphyritic rocks show indistinguishable Hf  
32  
33 352 isotopic compositions and single-stage Hf model ages of  $375 \pm 52$  Ma (range = 264–527  
34  
35 353 Ma,  $n = 56$ ), with relatively high  $\epsilon_{\text{Hf}}(t)$  values of  $12.0 \pm 0.4$  (weighted mean value, 95%  
36  
37 354 confidence level; range = 8.1–14.8,  $n = 56$ ). These data suggest that the porphyries shared  
38  
39 355 a common primitive mantle source, consistent with their island arc origin.  
40  
41  
42  
43  
44  
45

#### 46 **Amphibole, Plagioclase, Zircon, and Apatite Compositions**

47  
48 358 The compositions of amphibole, plagioclase, zircon, and apatite from samples of least-  
49  
50 359 altered porphyritic rocks are listed in Digital Appendix Tables A5, A6, A7, and A8,  
51  
52 360 respectively. Based on these analyses, water and sulfur contents as well as oxygen  
53  
54 361 fugacity of the magma have been estimated qualitatively and quantitatively.  
55  
56  
57  
58  
59  
60  
61  
62  
63  
64  
65

1  
2  
3  
4 363 *Amphibole compositions*

5  
6 364 Amphibole compositions can be used to estimate magmatic oxidation state,  
7  
8  
9 365 crystallization temperatures and pressures, as well as water contents (e.g., Ridolfi et al.,  
10  
11 366 2010; Zhang et al., 2012; Wang et al., 2014b). However, fresh amphibole grains were  
12  
13  
14 367 only observed in the P2E and P2L porphyries. All of the analyzed grains are calcic  
15  
16 368 amphiboles, and two generations of amphibole were recognized in both P2E and P2L.  
17  
18 369 Early stage grains occur as phenocrysts and are characterized by higher Al contents  
19  
20  
21 370 (range = 9.35–12.86 and 8.79–13.46 wt. % Al<sub>2</sub>O<sub>3</sub> for P2E and P2L, respectively; Digital  
22  
23 371 Appendix Table A5); they are mostly classified as magnesio-ferri-hornblende and  
24  
25 372 magnesio-hastingsite (including potassic-magnesio-hastingsite; Fig. 13A). The late stage  
26  
27 373 grains were developed in the groundmass or as recrystallized phenocrysts, typified by  
28  
29 374 lower Al concentrations (range = 1.62–4.76 and 4.33–7.53 wt. % Al<sub>2</sub>O<sub>3</sub> for P2E and P2L,  
30  
31 375 respectively; Digital Appendix Table A5). They are classified as magnesio-ferri-  
32  
33 376 hornblende or rare actinolite (Fig. 13A). The early stage amphibole grains are intergrown  
34  
35 377 with plagioclase phenocrysts (Fig. 14), and igneous apatite crystals occur as inclusions  
36  
37 378 within amphibole (Fig. 14B). This indicates that these three minerals are broadly coeval.

38  
39  
40  
41 379 The crystallization temperature, magmatic water contents, and oxygen fugacities were  
42  
43 380 estimated for the two stages of amphiboles using the spreadsheet of Ridolfi et al. (2010),  
44  
45 381 and the crystallization pressures were calculated following the equation of Mutch et al.  
46  
47 382 (2016). The Al-in-hornblende geobarometer used is applicable to granitoids that contain  
48  
49 383 amphibole, plagioclase, quartz, and alkali feldspar, broadly consistent with the mineral  
50  
51 384 assemblage within P2 porphyry rocks. The calculated results are listed in Digital  
52  
53 385 Appendix Table A5 and illustrated in Figure 13 (B–C).  
54  
55  
56  
57  
58  
59  
60  
61  
62  
63  
64  
65

1  
2  
3  
4 386 Amphibole phenocrysts from the P2E and P2L porphyry samples have similar  
5  
6 387 compositions, with calculated crystallization pressures from 3.5 to 6.7 kbar (average =  
7  
8 388  $4.6 \pm 0.8$  kbar,  $n = 51$ ), temperatures from 855 to 983 °C (average =  $900 \pm 30$  °C,  $n = 51$ ),  
9  
10 389  $\Delta$ FMQ values from 0.5 to 1.8 (average =  $1.1 \pm 0.3$ ,  $n = 51$ ), and H<sub>2</sub>O contents in melts  
11  
12 390 from 4.0 to 6.1 wt. % (average =  $5.1 \pm 0.4$  wt. %,  $n = 51$ ).  
13  
14  
15

16 391 Late stage (low-Al) amphiboles in P2E porphyry samples yielded crystallization  
17  
18 392 pressures from 0.6 to 1.4 kbar (average =  $1.1 \pm 0.3$  kbar,  $n = 12$ ), temperatures from 637°  
19  
20 393 to 774 °C (average =  $719 \pm 34$  °C,  $n = 12$ ),  $\Delta$ FMQ values from 2.6 to 3.3 (average =  $3 \pm$   
21  
22 394  $0.2$ ,  $n = 12$ ), and magmatic water contents from 3.6 to 5.1 wt. % (average =  $4 \pm 0.4$  wt. %,  $n$   
23  
24 395 = 12). Low-Al amphibole grains from P2L samples yielded slightly higher crystallization  
25  
26 396 pressures ( $2.0 \pm 0.4$  MPa; range = 1.3–2.6 kbar,  $n = 8$ ) and temperatures ( $800 \pm 24$  °C;  
27  
28 397 range = 751–800 °C,  $n = 8$ ), slightly lower  $\Delta$ FMQ values ( $2.4 \pm 0.3$ ; range = 1.1–2.9,  $n =$   
29  
30 398 8), but similar H<sub>2</sub>O contents ( $4.0 \pm 0.2$ ; range = 3.7–4.4,  $n = 8$ ) to those calculated for  
31  
32 399 P2E.  
33  
34  
35  
36  
37  
38

39 400 There are clear trends of increasing oxidation state and decreasing crystallization  
40  
41 401 pressures, temperatures, and magmatic water contents from early to late stage amphiboles  
42  
43 402 in both P2E and P2L porphyries (Figs. 13B–D). These trends are consistent with the  
44  
45 403 high-Al amphibole phenocrysts having crystallized at depth before final crystallization of  
46  
47 404 the magma (and low-Al amphibole) after emplacement at shallow levels (e.g., Rutherford  
48  
49 405 and Devine, 2003). The decreasing magmatic water contents might be attributed to  
50  
51 406 degassing during ascent and crystallization, which can also result in a small increase in  
52  
53 407 oxygen fugacity (Mathez, 1984; Candela, 1986; Burgisser and Scaillet, 2007; Zimmer et  
54  
55 408 al., 2010; Bell and Simon, 2011; Dilles et al., 2015).  
56  
57  
58  
59  
60  
61  
62  
63  
64  
65

1  
2  
3  
4 409

5  
6 410 *Plagioclase compositions*

7  
8  
9 411 Plagioclase phenocrysts from all P1 porphyry samples studied have been altered, but  
10 partially unaltered phenocrysts were found in some P2 and P3 porphyry samples.

11  
12  
13 413 Analyses with  $K_2O > 1$  wt. % are interpreted to reflect potassic alteration and have been  
14 excluded. Plagioclase grains from the P2E porphyry (sample RC13-13) are classified as  
15 oligoclase ( $\geq An_{17}$ ) to labradorite ( $\leq An_{70}$ ), with an average anorthite (An) content of  $44 \pm$   
16  
17 414  
18 oligoclase ( $\geq An_{17}$ ) to labradorite ( $\leq An_{70}$ ), with an average anorthite (An) content of  $44 \pm$   
19  
20 415  
21 12 mol % ( $n = 28$ ). Nearly all these crystals exhibited reverse zoning in An content, with  
22  
23 416  
24 compositional ranges up to  $\sim 16$  mol %, and FeO contents that correlate positively with  
25  
26 417  
27  $X_{An}$  values (Digital Appendix Table A6; Fig. 14A). Plagioclase grains from the P2L  
28  
29 418  
30 porphyry (samples RC13-26 and RC13-33) have compositions similar to P2E (An mol %  
31  
32 419  
33 =  $48 \pm 5$ ,  $n = 38$ ), and also show reverse zoning with amplitudes up to  $\sim 19$  mol % An that  
34  
35 420  
36 correlate with FeO contents (Fig. 14B). Such reverse zoning with positive An-FeO  
37  
38 421  
39 correlations were observed both in partially altered (i.e., sericite alteration; Fig. 14A) and  
40  
41 422  
42 relatively fresh plagioclase crystals (Fig. 14B), indicating that it was not likely to have  
43  
44 423  
45 been generated by hydrothermal alterations. In contrast, plagioclase grains from the P3  
46  
47 424  
48 porphyry (RC13-78) display relatively uniform An compositions (An mol % =  $51 \pm 5$ ,  $n$   
49  
50 425  
51 =  $37$ ), with no clear zoning in  $X_{An}$  and FeO (Fig. 14C).

52  
53 426  
54 Plagioclase compositions (An proportions) are very sensitive to dissolved water  
55  
56 427  
57 content and temperature of the melt, and thus can be used as a hygrometer if corrected for  
58  
59 428  
60 temperature (Mathez, 1973; Lange, 2009; Waters and Lange, 2015). We used apatite  
61  
62 429  
63 saturation temperatures (AST) following the formula of Piccoli and Candela (1994) to  
64  
65 430  
66 calculate magma temperatures for P2 and P3 samples (Table 4; Digital Appendix Table

1  
2  
3  
4 432 A3). The whole-rock SiO<sub>2</sub> and P<sub>2</sub>O<sub>5</sub> values were assumed to approximate the melt  
5  
6 433 contents at the time of crystallization, although this assumption can be challenged  
7  
8  
9 434 (Piccoli and Candela, 1994, 2002). Nevertheless, the calculated temperatures are  
10  
11 435 reasonable for magmas of intermediate, hydrous composition, and are also in agreement  
12  
13  
14 436 with the estimated crystallization temperatures of early stage amphibole (Digital  
15  
16 437 Appendix Table A5): 932 °C for P2E (RC13-13), 892 °C (RC13-26) and 905 °C (RC13-  
17  
18 438 33) for P2L, and 928 °C for P3 (RC13-78; Table 4).

21 439 The updated spreadsheet of Waters and Lange (2015) has been used to calculate  
22  
23 440 magmatic water contents (Digital Appendix Table A9). The calculated values are  
24  
25 441 relatively uniform and indistinguishable between the different porphyry phases:  $5.2 \pm 0.2$   
26  
27 442 (n = 28) for P2E,  $5.5 \pm 0.2$  (n = 38) for P2L, and  $5.1 \pm 0.1$  wt. % (n = 37) for P3. For the  
28  
29 443 P2E and P2L porphyries, the magmatic water contents calculated from plagioclase and  
30  
31 444 early stage amphibole compositions agree well with each other (Digital Appendix Tables  
32  
33 445 A5 and A8).

#### 37 446

#### 40 447 *Zircon trace element compositions*

42 448 Twenty trace element spot analyses were obtained for zircons from samples of P1 to  
43  
44 449 P3 porphyries (Digital Appendix Table A7; Fig. 15). It is common to encounter small  
45  
46 450 mineral inclusions, especially of apatite, titanite, in zircon during LA-ICP-MS analyses  
47  
48 451 (e.g., Lu et al., 2016). We have taken Ca > 200 ppm or La > 0.3 ppm as an indication of  
49  
50 452 apatite contamination, and Ti > 20 ppm to reflect titanite contamination, and such data  
51  
52 453 were excluded (Digital Appendix Table A7). The remaining analyses have low LREE  
53  
54 454 and elevated HREE contents, with small negative Eu and strongly positive Ce anomalies  
55  
56  
57  
58  
59  
60  
61  
62  
63  
64  
65

1  
2  
3  
4 455 (Fig. 15). These REE patterns and total contents ( $\Sigma\text{REE} = 351\text{--}1125$  ppm), as well as  
5  
6 456 Th/U ratios above 0.1 (0.26–0.63) (Digital Appendix Table A7) are typical of igneous  
7  
8 457 zircons from relatively oxidized magmas (Hoskin and Schaltegger, 2003).

9  
10  
11 458 Zircon crystals from the P1 to P3 porphyries show slightly different calculated Ti-in-  
12  
13 459 zircon temperatures and Eu anomalies ( $\text{Eu}_\text{N}/\text{Eu}_\text{N}^* = \text{Eu}_\text{N}/(\text{Sm}_\text{N} \times \text{Gd}_\text{N})^{0.5}$ ; Fig. 16; Digital  
14  
15 460 Appendix Table A7). Titanium-in-zircon temperatures were calculated using the equation  
16  
17 461 of Ferry and Watson (2007), where it is assumed that  $\log a_{\text{SiO}_2} = 1$  because of the  
18  
19 462 existence of quartz in the host porphyries, and  $\log a_{\text{TiO}_2} = 0.7$  due to the presence of  
20  
21 463 titanite (a common accessory mineral in these rocks). Zircon crystals from the P2E  
22  
23 464 porphyry (sample RC13-107) have the highest calculated temperatures (average of  $760 \pm$   
24  
25 465  $29$  °C; range =  $723^\circ\text{--}819^\circ\text{C}$ ,  $n = 14$ ) with relatively uniform  $\text{Eu}_\text{N}/\text{Eu}_\text{N}^*$  values from 0.5 to  
26  
27 466 0.7 (average =  $0.6 \pm 0.1$ ;  $n = 14$ ). Zircon crystals from the P3 porphyry (sample RC13-78)  
28  
29 467 show the lowest calculated temperatures (average =  $726 \pm 24$  °C; range =  $693^\circ\text{--}758^\circ\text{C}$ ,  $n$   
30  
31 468 = 18) and lowest  $\text{Eu}_\text{N}/\text{Eu}_\text{N}^*$  ratios ( $0.5 \pm 0.1$ ; range = 0.3–0.6,  $n = 18$ ). Zircon crystals  
32  
33 469 from the P1 and P2L porphyries have intermediate calculated temperatures (P1:  $736 \pm$   
34  
35 470  $26$  °C, range =  $699^\circ\text{--}810^\circ\text{C}$ ,  $n = 16$ ; P2L:  $730 \pm 24$  °C, range =  $705^\circ\text{--}795^\circ\text{C}$ ,  $n = 17$ ),  
36  
37 471 and a similar wide range of  $\text{Eu}_\text{N}/\text{Eu}_\text{N}^*$  values (P1: 0.3–1.0, average =  $0.6 \pm 0.2$ ; P2L: 0.3–  
38  
39 472 0.9, average =  $0.6 \pm 0.1$ ).

40  
41  
42 473 Trace element compositions in zircon are sensitive to magmatic water content and  
43  
44 474 oxygen fugacity, and have been used to distinguish between fertile and infertile suites in  
45  
46 475 porphyry Cu  $\pm$  Au  $\pm$  Mo systems (Ballard et al., 2002; Liang et al., 2006; Qiu et al., 2014;  
47  
48 476 Wang et al., 2014b; Dilles et al., 2015; Shen et al., 2015; Lu et al., 2016; Xu et al., 2016;  
49  
50 477 Loader et al., 2017). In hydrous magmas, early plagioclase crystallization is suppressed  
51  
52  
53  
54  
55  
56  
57  
58  
59  
60  
61  
62  
63  
64  
65



1  
2  
3  
4 478 (Moore and Carmichael, 1998), leading to no pronounced depletion of Eu in melts ( $\text{Eu}^{2+}$   
5  
6 479 substitutes for  $\text{Ca}^{2+}$  in plagioclase). On the other hand, in oxidized magmas, Eu is  
7  
8  
9 480 predominantly present as  $\text{Eu}^{3+}$  and is partitioned into zircon along with other REE  
10  
11 481 (Ballard et al., 2002; Hoskin and Schaltegger, 2003; Trail et al., 2011; Dilles et al., 2015).  
12  
13  
14 482 Therefore, the small negative Eu anomalies in zircon samples (as indicated by  $\text{Eu}_N/\text{Eu}_N^*$   
15  
16 483 ratios  $>0.3$  and mostly  $> 0.4$ ; Fig. 16A), and slightly positive anomalies in whole rocks  
17  
18  
19 484 (Fig. 10) indicate relatively high magmatic water contents and/or oxidation states  
20  
21 485 (Ballard et al., 2002; Dilles et al., 2015; Lu et al., 2016).

22  
23  
24 486 Ballard et al. (2002) defined the zircon  $\text{Ce}^{4+}/\text{Ce}^{3+}$  ratio as an indicator of magmatic  
25  
26 487 oxidation state. However, Dilles et al. (2015) and Lu et al. (2016) argue that these values  
27  
28  
29 488 are difficult to estimate accurately because the abundances of the adjacent elements, La  
30  
31 489 and Pr, which are used as a baseline to calculate the magnitude of the Ce anomaly, are  
32  
33  
34 490 low and close to the analytical detection limit. Confirming this reservation,  $\text{Ce}^{4+}/\text{Ce}^{3+}$   
35  
36 491 ratios and  $f\text{O}_2$  values calculated for our samples using the equation of Trail et al. (2011)  
37  
38  
39 492 yielded unrealistic and widely variable  $\Delta\text{FMQ}$  values (-9 to +5).

40  
41 493

#### 42 43 494 *Apatite compositions*

44  
45  
46 495 The  $\text{SO}_3$ , Cl, and F analyses of igneous apatites are listed in Digital Appendix Table  
47  
48 496 A8 and illustrated in Figures 17 and 18. The results show that igneous apatites from the  
49  
50  
51 497 P2 porphyries have higher sulfur and chlorine concentrations than those from P1 and P3  
52  
53 498 rocks. The high  $\text{SO}_3$  contents in apatites from the P2 porphyries (P2E: 0.11 to 0.8 wt. %  
54  
55 499  $\text{SO}_3$ , average =  $0.30 \pm 0.13$  wt. %,  $n = 34$ ; P2L: 0.07 to 1.2 wt. %  $\text{SO}_3$ , average =  $0.29 \pm$   
56  
57  
58 500 0.18 wt. %,  $n = 100$ ) are similar to values from global porphyry Cu deposits (Streck and

1  
2  
3  
4 501 Dilles, 1998; Imai, 2002; Li et al., 2012; Pan et al., 2016; Richards et al., 2017). In  
5  
6 502 comparison, apatite crystals from the P1 porphyry (RC13-39) have lower sulfur contents  
7  
8 503 (0.05 to 0.19 wt. % SO<sub>3</sub>; average = 0.11 ± 0.03 wt. %, n = 34), whereas those from the P3  
9  
10 504 porphyry (RC13-78) have the lowest sulfur concentrations (from 0.05 wt. % to below the  
11  
12 505 analytical detection limit of SO<sub>3</sub>; average of analyses above limit of detection = 0.03 ±  
13  
14 506 0.01, n = 13). Although the ranges for P1 and P2L porphyries overlap at their outer limits,  
15  
16 507 a t-test shows that the two populations are significantly different (t = 5.87, p = 0).  
17  
18  
19  
20

21 508 Similarly, the Cl contents in apatite crystals from P1 and P3 porphyries are  
22  
23 509 significantly lower (0.51 ± 0.3 wt. %, n = 34, and 0.1 ± 0.06 wt. %, n = 17, respectively)  
24  
25 510 compared to values from the P2 porphyries (P2E: 1.18 ± 0.37 wt. %, n = 34; P2L: 1.47 ±  
26  
27 511 0.28 wt. %, n = 100). There is a rough positive correlation between sulfur and chlorine  
28  
29 512 contents of apatites from the four porphyries (Fig. 18A), with relatively constant molar  
30  
31 513 S/Cl ratios (P1: 0.13 ± 0.08, n = 34; P2E: 0.13 ± 0.08, n = 34; P2L: 0.10 ± 0.14, n = 100;  
32  
33 514 P3: 0.16 ± 0.09, n = 13; Table 4). Detailed analyses also show that single apatite crystals  
34  
35 515 are commonly zoned in sulfur, with decreasing core-to-rim SO<sub>3</sub> contents (and small  
36  
37 516 decreases in Cl; Fig. 17C), possibly reflecting progressive degassing of SO<sub>2</sub> (and Cl)  
38  
39 517 from the melt during crystallization (Richards et al., 2017).  
40  
41  
42  
43  
44

45 518 Fluorine contents in apatites from the P1 and P3 porphyries are similar (P1: 3.64 ±  
46  
47 519 0.48 wt. %, n = 34; P3: 3.6 ± 0.4, n = 17) and distinctly higher than in the P2E (2.33 ±  
48  
49 520 0.29 wt. %, n = 34) and P2L (2.32 ± 0.23 wt. %, n = 100) porphyries.  
50  
51  
52

53 521 Some hydrothermal apatite grains were also analyzed for comparison with igneous  
54  
55 522 grains, and they show wide variations in sulfur and chlorine content (Digital Appendix  
56  
57 523 Table A8), as observed by other researchers (e.g., Li et al., 2012; Richards et al., 2017).  
58  
59  
60  
61  
62  
63  
64  
65

1  
2  
3  
4 524 The sulfur partition coefficient between apatite and melt is jointly controlled by  
5  
6 525 temperature, oxygen fugacity, and the S content in the silicate melt (Peng et al., 1997;  
7  
8  
9 526 Parat and Holtz, 2005; Parat et al., 2011; Webster and Piccoli, 2015; Konecke et al.,  
10  
11 527 2017a, b), and no formula currently exists to accurately calculate magmatic sulfur  
12  
13  
14 528 concentrations from apatite SO<sub>3</sub> contents. However, two semi-quantitative formulae can  
15  
16 529 be used to estimate relative magmatic S content (Peng et al., 1997; Parat et al., 2011).  
17  
18  
19 530 Using the equation of Peng et al. (1997), the magmas related to the P2E and P2L  
20  
21 531 porphyry intrusions are calculated to have sulfur concentrations of 0.03 ± 0.01 wt. % (n =  
22  
23 532 34) and 0.02 ± 0.01 wt. % (n = 100), significantly higher than the corresponding S  
24  
25  
26 533 contents for P1 (0.010 ± 0.003 wt. % S, n = 34) and P3 magmas (0.003 ± 0.001 wt. % S,  
27  
28 534 n = 13; Table 4). The results calculated by the method of Parat et al. (2011) are more  
29  
30  
31 535 variable, and yielded lower absolute values than those from Peng et al. (1997). However,  
32  
33 536 they also support the conclusion that the P2E and P2L magmas had significantly higher  
34  
35  
36 537 sulfur contents than the P1 and P3 magmas (Table 4).

37  
38 538 The chlorine partition coefficient between apatite and melt is a complex function of  
39  
40  
41 539 magma composition and Cl concentration in the melt (Zhu and Sverjensky, 1991; Piccoli  
42  
43 540 and Candela, 1994; Mathez and Webster, 2005; Webster et al., 2009; Chelle-Michou and  
44  
45  
46 541 Chiaradia, 2017). Mathez and Webster (2005) proposed a value of 0.8 as the partition  
47  
48 542 coefficient (mass ratio) between apatite and basaltic melt (51.1 wt. % SiO<sub>2</sub>). Based on  
49  
50  
51 543 this semi-quantitative equation (and recognizing that these magmas were not basaltic), we  
52  
53 544 estimate Cl concentrations in the P2E and P2L magmas of 1.48 ± 0.46 wt.% (n = 34) and  
54  
55 545 1.83 ± 0.34 wt.% (n = 100), respectively, significantly higher than for P1 (0.63 ± 0.38  
56  
57  
58 546 wt.%, n = 34) and P3 (0.12 ± 0.07 wt.%; Table 4).

1  
2  
3  
4  
5  
6  
7  
8  
9  
10  
11  
12  
13  
14  
15  
16  
17  
18  
19  
20  
21  
22  
23  
24  
25  
26  
27  
28  
29  
30  
31  
32  
33  
34  
35  
36  
37  
38  
39  
40  
41  
42  
43  
44  
45  
46  
47  
48  
49  
50  
51  
52  
53  
54  
55  
56  
57  
58  
59  
60  
61  
62  
63  
64  
65

547

548 **Discussion**

549 *Magmatic duration and timing of ore formation at Red Chris*

550 Four phases of the Red Stock, P1, P2E, P2L, and P3, have been dated at  $211.6 \pm 1.3$   
551 Ma,  $206.0 \pm 1.2$  Ma,  $203.6 \pm 1.8$  Ma, and  $201.7 \pm 1.2$  Ma, respectively, spanning a period  
552 of ~10 m.y. (Fig. 6; Digital Appendix Table A2). These ages are consistent with  
553 crosscutting relationships described by Rees et al. (2015). Re-Os dating of molybdenite  
554 intergrown with chalcopyrite in quartz veins yielded a weighted mean age of  $206.1 \pm 0.5$   
555 Ma (Fig. 7), reflecting the timing of mineralization and in good agreement with the  
556 emplacement age of the mineralized P2E quartz monzonite porphyry. Ore formation  
557 occurred at a relatively late stage in the ~10 m.y. evolution of the Red Stock, and over a  
558 relatively brief period time (<1 m.y., as defined by the uncertainty on the average of three  
559 Re-Os analyses). This relatively late and short duration of mineralization is similar to the  
560 timing observed in many other porphyry deposits (e.g., Cathles et al., 1997; Masterman et  
561 al., 2004; von Quadt et al., 2011; Chiaradia et al., 2013; Correa et al., 2016; Li et al.,  
562 2017).

563 The age of mineralization at ~206 Ma is contemporaneous with the major pulse of  
564 mineralization in the Stikine and Quesnel terranes, representing a particularly fertile pre-  
565 accretionary magmatic event (Nelson and Colpron, 2007; Nelson et al., 2013; Logan and  
566 Mihalynuk, 2014).

567

568 *Igneous geochemistry and petrogenesis*

1  
2  
3  
4 569 Whole-rock major and trace element compositions of P1 to P3 porphyry rocks are  
5  
6 570 almost identical to each other, and show characteristics of subduction-related magmatic  
7  
8  
9 571 rocks with high LILE and low HFSE concentrations (Figs. 9 and 10; Hawkesworth et al.,  
10  
11 572 1993; Pearce, 1996). The high Sr/Y ratios ( $53 \pm 23$ ,  $n = 12$ ) and slightly positive Eu  
12  
13 573 anomalies ( $Eu_n/Eu_n^* = 1.1 \pm 0.15$ ;  $n = 14$ ) indicate the suppression of plagioclase  
14  
15 574 crystallization and early crystallization of amphibole from hydrous and oxidized magmas  
16  
17 575 (Richards and Kerrich, 2007; Loucks, 2014). Rees et al. (2015) concluded from their  
18  
19 576 analysis of petrochemistry that the Red Stock evolved from subalkaline (P1, P2) to  
20  
21 577 marginally alkaline (P3), and classified the overall system as high-K calc-alkalic.

22  
23  
24  
25 578 All the porphyritic rocks from P1 to P3 show mantle-like, relatively low ( $^{87}\text{Sr}/^{86}\text{Sr}$ )<sub>t</sub>  
26  
27 579 ( $0.7044 \pm 0.0002$ ) and high  $\epsilon_{\text{Nd}}(t)$  ( $+3.1 \pm 0.4$ ) values, and similar single-stage Nd model  
28  
29 580 ages ( $0.80 \pm 0.05$  Ga). Zircon crystals from these rocks yield positive zircon  $\epsilon_{\text{Hf}}(t)$  values  
30  
31 581 ( $+8.1$  to  $+14.8$ ) and single-stage Hf model ages of  $375 \pm 52$  Ma (Figs. 11 and 12). These  
32  
33 582 data indicate minimal involvement of ancient crustal components in the petrogenesis of  
34  
35 583 these magmas, as observed for other Mesozoic igneous rocks in the Stikine terrane, and  
36  
37 584 are consistent with an oceanic island arc setting (Samson et al., 1989; Logan and  
38  
39 585 Mihalynuk, 2014).

40  
41 586 Late basaltic to andesitic dikes have similar Nd–Sr isotopic compositions to the  
42  
43 587 porphyritic rocks, but show distinct trace element and REE patterns, and lower Sr/Y and  
44  
45 588 La/Yb ratios, suggesting that they are not cogenetic.

46  
47 589  
48  
49  
50  
51 590 *Oxygen fugacity and sulfur-chlorine-water contents of the porphyry magmas*

1  
2  
3  
4 591 Magmatic oxidation state, and sulfur, chlorine, and water contents are fundamental  
5  
6 592 factors for the formation of porphyry Cu deposits (e.g., Burnham, 1979; Candela, 1992;  
7  
8  
9 593 Richards, 2003; Loucks, 2014). It is difficult to measure the original magmatic oxidation  
10  
11 594 state in altered plutonic rocks, but normalized Ce and Eu anomalies in zircons can be  
12  
13  
14 595 used to provide qualitative estimates (Ballard et al., 2002; Dilles et al., 2015; Lu et al.,  
15  
16 596 2016). Zircon grains from the P1 to P3 porphyries display large positive Ce and small  
17  
18  
19 597 negative Eu anomalies ( $Eu_N/Eu_N^*$  mostly  $> 0.4$ ; Figs. 15 and 16), similar to zircons from  
20  
21 598 other mineralized porphyry systems worldwide (Wang et al., 2014b; Dilles et al., 2015;  
22  
23  
24 599 Lu et al., 2016). These data are also consistent with estimates of magmatic oxidation state  
25  
26 600 from early stage amphibole phenocrysts from the P2E and P2L porphyries, which yielded  
27  
28  
29 601  $\Delta FMQ$  values of  $1.5 \pm 0.2$  ( $n = 7$ ) and  $1.1 \pm 0.3$  ( $n = 44$ ). Consequently, we conclude that  
30  
31 602 the four phases of magma in the Red Stock were all at least moderately oxidized.

32  
33  
34 603 It is similarly difficult to estimate original magmatic water contents from altered  
35  
36 604 plutonic rocks. However, the presence of amphibole phenocrysts in the P1 to P3  
37  
38  
39 605 porphyries suggest that the magmas contained at least 4 wt. %  $H_2O$  (Burnham, 1979,  
40  
41 606 Naney, 1983; Merzbacher and Egglar, 1984; Rutherford and Devine, 1988; Ridolfi et al.,  
42  
43  
44 607 2010). This observation is supported by: (1) high whole-rock Sr/Y ratios ( $53 \pm 23$ ,  $n =$   
45  
46 608 12), which reflect the suppression of plagioclase relative to amphibole crystallization  
47  
48  
49 609 under hydrous conditions (Moore and Carmichael, 1998; Richards and Kerrich, 2007); (2)  
50  
51 610 high  $10000 \times (Eu_N/Eu_N^*)/Y$  ( $> 1$ ) and low Dy/Yb ( $< 0.3$ ) ratios in zircons (Digital Appendix  
52  
53  
54 611 Table A7; Lu et al., 2016); (3) high whole-rock V/Sc ratios ( $9.0 \pm 0.9$ ,  $n = 14$ ) (Loucks,  
55  
56 612 2014); and (4) estimates of magmatic water content from plagioclase phenocryst  
57  
58 613 compositions, which indicate values of  $\sim 5$  wt.%  $H_2O$ .

1  
2  
3  
4 614 The compositions of igneous apatite inclusions in plagioclase and amphibole  
5  
6  
7 615 phenocrysts have been used to estimate magmatic sulfur and chlorine contents. The  
8  
9 616 results suggest that apatite microphenocrysts from the P2E and P2L porphyries had  
10  
11 617 higher S and Cl contents than for P1 and P3 (Fig. 18). The SO<sub>3</sub> contents in apatite are  
12  
13  
14 618 controlled by both magmatic sulfur concentration and oxidation state (Peng et al., 1997;  
15  
16 619 Parat and Holtz, 2005; Webster and Piccoli, 2015). Sulfur occurs in the apatite structure  
17  
18  
19 620 mainly as S<sup>6+</sup> and its content will increase in relatively oxidized environments (Boyce et  
20  
21 621 al., 2010; Parat et al., 2011; Konecke et al., 2017b). The magmas associated with the four  
22  
23  
24 622 porphyry phases at Red Chris were all moderately oxidized, and therefore the differences  
25  
26 623 in apatite sulfur content likely mainly reflect variations in the sulfur fugacity in the  
27  
28  
29 624 associated melts. The data indicate that the P2E and P2L porphyry magmas contained  
30  
31 625 significantly higher S contents than the P1 and P3 magmas (Fig. 18). Models used to  
32  
33 626 estimate magmatic sulfur content in equilibrium with apatite (Peng et al., 1997) are not  
34  
35  
36 627 strictly accurate because of uncertainties in the details of exchange reactions (Streck and  
37  
38 628 Dilles, 1998; Mao et al., 2016) but are expected to be correct in relative terms. Our data  
39  
40  
41 629 yield higher values for the P2E and P2L porphyries (0.02–0.03 wt. % S) compared to  
42  
43 630 estimates for P1 (0.01 wt. % S) and P3 (0.003 wt. % S). Consequently, we conclude that  
44  
45  
46 631 the syn-mineral porphyry (P2E and P2L) magmas were more S-rich than the pre-  
47  
48 632 mineralization P1 and especially the post-mineralization P3 porphyry magmas.

49  
50 633 Similarly, the magmatic Cl contents calculated from apatite compositions in the P2E  
51  
52  
53 634 and P2L porphyries are also higher than in the P1 and P3 porphyries, whereas F contents  
54  
55 635 are lower (Table 4). Volatile species such as S, Cl, and F are differentially affected by  
56  
57  
58 636 degassing during ascent and crystallization of magmas: S and Cl will be preferentially

1  
2  
3  
4 637 lost to the vapor phase relative to F (Webster et al., 2014; Stock et al., 2016), leading to  
5  
6 638 high F/Cl and F/S ratios in degassed magmas. The data shown in Figure 18 suggest that  
7  
8  
9 639 the P2E and P2L were S-Cl-rich, whereas the P1 and P3 were S-Cl-poor but enriched in F.

10  
11 640 These differences could reflect either loss of volatiles from the source magma  
12  
13 641 chamber (presumed to be an underlying batholith) prior to emplacement of the P1 and P3  
14  
15 642 magmas but not in the case of P2, or conversely addition of a volatile phase or a volatile-  
16  
17 643 rich magma to the magma chamber immediately prior to emplacement of P2. Volatile  
18  
19 644 loss is expected to be a general condition of upper crustal magma emplacement, and this  
20  
21 645 may well be a factor contributing to the low Cl/F ratios in the late P3 magmas, as well as  
22  
23 646 the negatively correlated trend for F and Cl in P1. The P2 magma was emplaced after P1,  
24  
25 647 and so might be expected to be similarly degassed if this represents a comagmatic  
26  
27 648 sequence. However, the 6–8 m.y. age difference between P1 ( $211.6 \pm 1.3$  Ma) and P2  
28  
29 649 (P2E:  $206.0 \pm 1.2$  Ma; P2L:  $203.6 \pm 1.8$  Ma) indicates that P1 and P2 are not directly  
30  
31 650 comagmatic. One explanation is that the P2 event represents a pulse of S-Cl-rich magma  
32  
33 651 injected at a relatively late stage into the mid-crustal magma reservoir, leading to a pulse  
34  
35 652 of fluid exsolution and injection of P2 magma into the shallower level Red Stock, where  
36  
37 653 syn-P2, quartz-vein hosted mineralization formed the Red Chris Cu-Au deposit. The  
38  
39 654 post-mineralization P3 ( $201.7 \pm 1.2$  Ma) and P4 porphyries may represent the final stages  
40  
41 655 of intrusive activity emanating from the now degassed underlying magma chamber.

42  
43 656 Although both P2E and P2L porphyries are S-Cl-rich, apatites from P2L are  
44  
45 657 marginally the most enriched. Samples of P2L are also the most mafic ( $\text{SiO}_2$ -poor) in the  
46  
47 658 suite, and it is therefore tempting to speculate that the source magma chamber was  
48  
49 659 recharged with more mafic, S-Cl- $\text{H}_2\text{O}$ -rich magma during the P2 stage. The solubility of  
50  
51  
52  
53  
54  
55  
56  
57  
58  
59  
60  
61  
62  
63  
64  
65



1  
2  
3  
4 660 S and Cl is higher in oxidized mafic magmas compared to felsic melts (> 1000 ppm S  
5  
6 661 and > 3000 ppm Cl; Carmichael and Ghiorso, 1986; Webster, 1997; Webster et al., 1999;  
7  
8  
9 662 Hattori and Keith, 2001; Jugo et al., 2005; Jugo, 2009; Chelle-Michou and Chiaradia,  
10  
11 663 2017). Therefore, a key step in porphyry ore formation at Red Chris may have been  
12  
13  
14 664 recharge of the batholithic system by a less evolved, although broadly cogenetic, magma  
15  
16 665 (cf. Hattori and Keith, 2001; Steinberger et al., 2013; Large et al., 2018).

17  
18  
19 666 Support for this recharge model is provided by high magmatic temperatures  
20  
21 667 calculated from zircon grains from some P2 samples (Fig. 16), and reverse zoning  
22  
23  
24 668 observed in plagioclase phenocrysts from the P2E and P2L porphyries, but which is not  
25  
26 669 observed in P3 (Fig. 14C). In detail, zircons from the P2E porphyry show the highest Ti-  
27  
28 670 in-zircon temperatures and  $Eu_N/Eu_N^*$  values, and P3 the lowest values. This might reflect  
29  
30  
31 671 an influx of higher temperature melt during the evolution of the P2E magma, and greater  
32  
33 672 degrees of plagioclase fractionation from the late P3 magma. The compositional ranges  
34  
35  
36 673 of up to ~19 mol % An for plagioclase are higher than the upper limit caused by chemical  
37  
38 674 diffusion (~10 mol % An; Pearce and Kolisnik, 1990). Furthermore, these reverse zoning  
39  
40  
41 675 patterns are matched by FeO contents in the phenocrysts (Figs. 14A and 14B), which  
42  
43 676 suggests that the zonation reflects changes in magma composition (as opposed to simply  
44  
45  
46 677 changes in pressure, temperature, or water content; Ginibre and Wörner, 2007; Lange,  
47  
48 678 2009; Ustunisik et al., 2014; Waters and Lange, 2015). We therefore interpret these  
49  
50  
51 679 changes to reflect late-stage (rim) growth from a more mafic magma that mixed into a  
52  
53 680 more evolved resident magma.

54  
55 681

56  
57  
58 682

## Conclusions

1  
2  
3  
4 683 Zircon U-Pb ages indicate that the Red Stock was emplaced over a period of ~10 m.y.  
5  
6 684 ( $211.6 \pm 1.3$  Ma,  $206.0 \pm 1.2$  Ma,  $203.6 \pm 1.8$  Ma, and  $201.7 \pm 1.2$  Ma for the P1, P2E,  
7  
8 685 P2L, and P3 porphyries, respectively). The ore-forming event at Red Chris occurred  
9  
10 686 relatively late in this magmatic history, synchronous with P2E at  $206.1 \pm 0.5$  Ma, and  
11  
12 687 over a short period of <1 m.y. (as constrained by the error on the average of three Re-Os  
13  
14 688 analyses). The four phases of porphyry and their related magmas were chemically fairly  
15  
16 689 homogeneous and isotopically primitive, consistent with an island arc origin. The  
17  
18 690 magmas were all moderately oxidized and hydrous (~5 wt. H<sub>2</sub>O), but the P2 magmas had  
19  
20 691 distinctly higher S and Cl contents. Combined with evidence for reverse zonation in  
21  
22 692 plagioclase phenocrysts from P2 porphyries, and more mafic compositions in P2L, we  
23  
24 693 suggest that the deeper source magma chamber was recharged at the time of  
25  
26 694 emplacement of the P2 porphyries by injection of a more mafic S-Cl-rich magma. This  
27  
28 695 recharge process may have triggered ore formation by causing voluminous exsolution of  
29  
30 696 metalliferous hydrothermal fluids.  
31  
32  
33  
34  
35  
36  
37  
38  
39  
40

#### 41 **Acknowledgements**

42  
43 699 This research was funded by a Collaborative Research and Development Grant from  
44  
45 700 Natural Sciences and Engineering Research Council of Canada and the Red Chris  
46  
47 701 Development Company Ltd. (RCDC) to JPR, and a post-doctoral fellowship from China  
48  
49 702 Scholarship Council, University of Alberta, and Institute of Geochemistry, Chinese  
50  
51 703 Academy of Sciences to JJZ. RCDC provided access to the Red Chris mine by Jürgen  
52  
53 704 Lang to collect samples from drill core in 2014. Prof. Zhaochu Hu from China University  
54  
55 705 of Geosciences at Wuhan, China is thanked for help with in-situ zircon LA-ICP-MS Hf  
56  
57  
58  
59  
60  
61  
62  
63  
64  
65

1  
2  
3  
4 706 isotope analyses, which was funded by the National Natural Science Foundation Project  
5  
6 707 of China (41673049 and 41303040), and the National Key Research and Development  
7  
8 708 Program of China (2016YFC0600503) to JJZ. We particularly thank Steve Robertson and  
9  
10  
11 709 ‘Lyn Anglin from RCDC for support of this project. We thank David Cooke and Adam  
12  
13  
14 710 Bath for constructive reviews of the manuscript.  
15

16 711

17  
18  
19 712 **References**

- 20  
21 713 Annen, C., Blundy, J., and Sparks, R., 2006, The genesis of intermediate and silicic  
22 714 magmas in deep crustal hot zones: *Journal of Petrology*, v. 47, p. 505–539.  
23 715 Ash, C.H., Fraser, T.M., Blanchflower, J.D. and Thurston, B.G., 1995, Tatogga Lake  
24 716 project, north western British Columbia (104H/11, 12); in *Geological Field work 1994*,  
25 717 BC Ministry of Energy, Mines and Petroleum Resources, Paper 1995-1, p. 343–358.  
26 718 Ash, C.H., Stinson, P.K., and Macdonald, R.W.J., 1996, Geology of the Todagin plateau  
27 719 and Kinaskan Lake area, northwestern British Columbia (104H/12, 104G/9): B.C.  
28 720 Ministry of Energy, Mines and Petroleum Resources Paper 1996-1, p. 155–174.  
29 721 Baker, T., Ash, C., and Thompson, J., 1997, Geological setting and characteristics of the  
30 722 Red Chris porphyry copper-gold deposit, northwestern British Columbia: *Exploration*  
31 723 *Mining Geology*, v. 6, p. 297–316.  
32 724 Ballard, J. R., Palin, M. J., and Campbell, I. H., 2002, Relative oxidation states of  
33 725 magmas inferred from  $Ce^{(IV)}/Ce^{(III)}$  in zircon: application to porphyry copper deposits  
34 726 of northern Chile: *Contributions to Mineralogy and Petrology*, v. 144, p. 347–364.  
35 727 Bath, A. B., Cooke, D. R., Friedman, R. M., Faure, K., Kamenetsky, V. S., Tosdal, R. M.,  
36 728 and Berry, R. F., 2014, Mineralization, U-Pb geochronology, and stable isotope  
37 729 geochemistry of the lower main zone of the Lorraine deposit, north-central British  
38 730 Columbia: a replacement-style alkalic Cu-Au porphyry: *Economic Geology*, v. 109, p.  
39 731 979–1004.  
40 732 Bell, A. S., and Simon, A., 2011, Experimental evidence for the alteration of the  $Fe^{3+}/\Sigma Fe$   
41 733 of silicate melt caused by the degassing of chlorine-bearing aqueous volatiles:  
42 734 *Geology*, v. 39, p. 499–502.  
43 735 Bissig, T., and Cooke, D. R., 2014, Introduction to the special issue devoted to alkalic  
44 736 porphyry Cu-Au and epithermal Au Deposits: *Economic Geology*, v. 109, p. 819–825.  
45  
46  
47  
48  
49  
50  
51  
52  
53  
54  
55  
56  
57  
58  
59  
60  
61  
62  
63  
64  
65

1  
2  
3  
4  
5  
6  
7  
8  
9  
10  
11  
12  
13  
14  
15  
16  
17  
18  
19  
20  
21  
22  
23  
24  
25  
26  
27  
28  
29  
30  
31  
32  
33  
34  
35  
36  
37  
38  
39  
40  
41  
42  
43  
44  
45  
46  
47  
48  
49  
50  
51  
52  
53  
54  
55  
56  
57  
58  
59  
60  
61  
62  
63  
64  
65

737 Blundy, J., Mavrogenes, J., Tattitch, B., Sparks, S., and Gilmer, A., 2015, Generation of  
738 porphyry copper deposits by gas-brine reaction in volcanic arcs: *Nature Geoscience*, v.  
739 8, p. 235–240.

740 Boyce, J. W., Liu, Y., Rossman, G. R., Guan, Y., Eiler, J. M., Stolper, E. M., and Taylor,  
741 L. A., 2010, Lunar apatite with terrestrial volatile abundances: *Nature*, v. 466, p. 466.

742 Brown, D. A., Logan, J. M., Gunning, M. H., Orchard, M. J., and Bamber, W. E., 1991,  
743 Stratigraphic evolution of the Paleozoic Stikine assemblage in the Stikine and Iskut  
744 rivers area, northwestern British Columbia: *Canadian Journal of Earth Sciences*, v. 28,  
745 p. 958–972.

746 Brown, P., and Kahlert, B., 1986, Geology and mineralization of the Red Mountain  
747 porphyry molybdenum deposit, south-central Yukon: *Canadian Institute of Mining  
748 and Metallurgy, Special Volume 37*, p. 288–297.

749 Burgisser, A., and Scaillet, B., 2007, Redox evolution of a degassing magma rising to the  
750 surface: *Nature*, v. 445, p. 194–197.

751 Burnham, C.W., 1979, Magmas and hydrothermal fluids, in Barnes, H.L., ed.,  
752 *Geochemistry of hydrothermal ore deposits*, 2nd ed.: New York, John Wiley and Sons,  
753 p. 71–136.

754 Byrne, K., and Tosdal, R. M., 2014, Genesis of the Late Triassic southwest zone breccia-  
755 hosted alkalic porphyry Cu-Au deposit, Galore Creek, British Columbia, Canada:  
756 *Economic Geology*, v. 109, p. 915–938.

757 Candela, P. A., 1986, The evolution of aqueous vapor from silicate melts: effect on  
758 oxygen fugacity: *Geochimica et Cosmochimica Acta*, v. 50, p. 1205–1211.

759 Candela, P. A., 1992, Controls on ore metal ratios in granite-related ore systems: an  
760 experimental and computational approach: *Transactions of the Royal Society of  
761 Edinburgh, Earth Sciences*, v. 83, p. 317–326.

762 Candela, P.A., and Holland, H.D., 1984, The partitioning of copper and molybdenum  
763 between silicate melts and aqueous fluids: *Geochimica et Cosmochimica Acta*, v. 48, p.  
764 373–380.

765 Carmichael, I. S., and Ghiorso, M. S., 1986, Oxidation-reduction relations in basic  
766 magma: a case for homogeneous equilibria: *Earth and Planetary Science Letters*, v. 78,  
767 p. 200–210.

768 Cathles, L. M., Erendi, A., and Barrie, T., 1997, How long can a hydrothermal system be  
769 sustained by a single intrusive event?: *Economic Geology*, v. 92, p. 766–771

770 Chambefort, I., Dilles, J. H., and Kent, A. J. R., 2008, Anhydrite-bearing andesite and  
771 dacite as a source for sulfur in magmatic-hydrothermal mineral deposits: *Geology*, v.  
772 36, p. 719–722.

- 1  
2  
3  
4 773 Chelle-Michou, C., and Chiaradia, M., 2017, Amphibole and apatite insights into the  
5  
6 774 evolution and mass balance of Cl and S in magmas associated with porphyry copper  
7  
8 775 deposits: *Contributions to Mineralogy and Petrology*, v. 172, 105, doi:  
9  
10 776 <https://doi.org/10.1007/s00410-017-1417-2>  
11  
12 777 Chiaradia, M., Ulianov, A., Kouzmanov, K., and Beate, B., 2012, Why large porphyry Cu  
13  
14 778 deposits like high Sr/Y magmas?: *Scientific reports*, v. 2, 685.  
15  
16 779 Chiaradia, M., Schaltegger, U., Spikings, R., Wotzlaw, J.-F., and Ovtcharova, M., 2013,  
17  
18 780 How accurately can we date the duration of magmatic-hydrothermal events in  
19  
20 781 porphyry systems?—An invited paper: *Economic Geology*, v. 108, p. 565–584.  
21  
22 782 Correa, K. J., Rabbia, O. M., Hernández, L. B., Selby, D., and Astengo, M., 2016, The  
23  
24 783 timing of magmatism and ore formation in the El Abra porphyry copper deposit,  
25  
26 784 northern Chile: implications for long-lived multiple-event magmatic-hydrothermal  
27  
28 785 porphyry Systems: *Economic Geology*, v. 111, p. 1–28.  
29  
30 786 Creasey, S., 1977, Intrusives associated with porphyry copper deposits: *Bulletin of the*  
31  
32 787 *Geological Society of Malaysia*, v. 9, p. 51–66.  
33  
34 788 Devine, F. A. M., Chamberlain, C. M., Davies, A. G. S., Friedman, R., and Baxter, P.,  
35  
36 789 2014, Geology and district-scale setting of tilted alkalic porphyry Cu-Au  
37  
38 790 mineralization at the Lorraine deposit, British Columbia: *Economic Geology*, v. 109, p.  
39  
40 791 939–977.  
41  
42 792 Dilles, J. H., Kent, A. J., Wooden, J. L., Tosdal, R. M., Koleszar, A., Lee, R. G., and  
43  
44 793 Farmer, L. P., 2015, Zircon compositional evidence for sulfur-degassing from ore-  
45  
46 794 forming arc magmas: *Economic Geology*, v. 110, p. 241–251.  
47  
48 795 Dostal, J., Gale, V., and Church, B., 1999, Upper Triassic Takla Group volcanic rocks,  
49  
50 796 Stikine Terrane, north-central British Columbia: geochemistry, petrogenesis, and  
51  
52 797 tectonic implications: *Canadian Journal of Earth Sciences*, v. 36, p. 1483–1494.  
53  
54 798 DURING, P., ROWINS, S. M., MCKINLEY, B. S. M., DICKINSON, J. M., DIAKOW, L. J., KIM,  
55  
56 799 Y.-S., and CREASER, R. A., 2009, Magmatic and structural controls on porphyry-style  
57  
58 800 Cu–Au–Mo mineralization at Kemess South, Toodoggone District of British  
59  
60 801 Columbia, Canada: *Mineralium Deposita*, v. 44, p. 435–462.  
61  
62 802 Ferry, J., and Watson, E., 2007, New thermodynamic models and revised calibrations for  
63  
64 803 the Ti-in-zircon and Zr-in-rutile thermometers: *Contributions to Mineralogy and*  
65  
804 *Petrology*, v. 154, p. 429–437.  
805  
806 Friedman, R.M., and Ash, C.H., 1997, U-Pb age of intrusions related to porphyry Cu-Au  
807  
808 mineralization in the Tatogga Lake area, northwestern British Columbia: B.C.  
809  
810 Ministry of Employment and Investment Paper 1997-1, p. 291–297.  
811  
812 Gabrielse, H., 1991, Late Paleozoic and Mesozoic terrane interactions in north-central  
813  
814 British Columbia: *Canadian Journal of Earth Sciences*, v. 28, p. 947–957.

- 1  
2  
3  
4 810 Gagnon, J.-F., Barresi, T., Waldron, J. W., Nelson, J., Poulton, T., and Cordey, F., 2012,  
5 811 Stratigraphy of the upper Hazelton Group and the Jurassic evolution of the Stikine  
6 812 terrane, British Columbia 1 1 ESS Contribution 20120051: Canadian Journal of Earth  
7 813 Sciences, v. 49, p. 1027–1052.
- 10 814 Gillstrom, G., Anand, R., Robertson, S., and Sterling, P., 2012, 2012 technical report on  
11 815 the Red Chris copper-gold project, for Imperial Metals Corp (Amended and Restated  
12 816 at 2015). <https://www.imperialmetals.com/assets/docs/red-chris-43-101-report-sept-30-2015.pdf>.  
15 817
- 16 818 Ginibre, C., and Wörner, G., 2007, Variable parent magmas and recharge regimes of the  
17 819 Parinacota magma system (N. Chile) revealed by Fe, Mg and Sr zoning in plagioclase:  
18 820 Lithos, v. 98, p. 118–140.
- 21 821 Goldstein, S., O'Nions, R., and Hamilton, P., 1984, A Sm-Nd isotopic study of  
22 822 atmospheric dusts and particulates from major river systems: Earth and planetary  
23 823 Science letters, v. 70, p. 221–236.
- 25 824 Gustafson, L.B., and Hunt, J.P., 1975, The porphyry copper deposit at El Salvador, Chile:  
26 825 Economic Geology, v. 70, p. 857–912.
- 28 826 Halter, W. E., Heinrich, C. A., and Pettke, T., 2005, Magma evolution and the formation  
29 827 of porphyry Cu-Au ore fluids: evidence from silicate and sulfide melt inclusions:  
30 828 Mineralium Deposita, v. 39, p. 845–863.
- 33 829 Harris, A. C., Dunlap, W. J., Reiners, P. W., Allen, C. M., Cooke, D. R., White, N. C.,  
34 830 Campbell, I. H., and Golding, S. D., 2008, Multimillion year thermal history of a  
35 831 porphyry copper deposit: application of U–Pb,  $^{40}\text{Ar}/^{39}\text{Ar}$  and (U–Th)/He chronometers,  
36 832 Bajo de la Alumbrera copper–gold deposit, Argentina: Mineralium Deposita, v. 43, p.  
37 833 295–314.
- 40 834 Hattori, K., 1993, High-sulfur magma, a product of fluid discharge from underlying  
41 835 mafic magma: evidence from Mount Pinatubo, Philippines: Geology, v. 21, p. 1083–  
42 836 1086.
- 45 837 Hattori, K. H., and Keith, J. D., 2001, Contribution of mafic melt to porphyry copper  
46 838 mineralization: evidence from Mount Pinatubo, Philippines, and Bingham Canyon,  
47 839 Utah, USA: Mineralium Deposita, v. 36, p. 799–806.
- 50 840 Hawkesworth, C., Gallagher, K., Hergt, J., and McDermott, F., 1993, Mantle and slab  
51 841 contributions in arc magmas: Annual Review of Earth and Planetary Sciences, v. 21, p.  
52 842 175–204.
- 54 843 Hayba, D. O., and Ingebritsen, S. E., 1997, Multiphase groundwater flow near cooling  
55 844 plutons: Journal of Geophysical Research, v. 102, p. 235–252.
- 57 845 Hoskin, P. W., and Schaltegger, U., 2003, The composition of zircon and igneous and  
58 846 metamorphic petrogenesis: Reviews in mineralogy and geochemistry, v. 53, p. 27–62.

- 1  
2  
3  
4 847 Hou, Z., Yang, Z., Lu, Y., Kemp, A., Zheng, Y., Li, Q., Tang, J., Yang, Z., and Duan, L.,  
5 848 2015, A genetic linkage between subduction-and collision-related porphyry Cu  
6 849 deposits in continental collision zones: *Geology*, v. 43, p. 247–250.
- 7  
8  
9 850 Imai, A., 2002, Metallogenesis of porphyry Cu deposits of the western Luzon arc,  
10 851 Philippines: K-Ar ages, SO<sub>3</sub> Contents of microphenocrystic apatite and significance of  
11 852 intrusive rocks: *Resource Geology*, v. 52, p. 147–161.
- 12  
13 853 Jago, C. P., Tosdal, R. M., Cooke, D. R., and Harris, A. C., 2014, Vertical and lateral  
14 854 variation of mineralogy and chemistry in the Early Jurassic Mt. Milligan alkalic  
15 855 porphyry Au-Cu deposit, British Columbia, Canada: *Economic Geology*, v. 109, p.  
16 856 1005–1033.
- 17  
18 857 Jugo, P. J., Luth, R. W., and Richards, J. P., 2005, Experimental data on the speciation of  
19 858 sulfur as a function of oxygen fugacity in basaltic melts: *Geochimica et*  
20 859 *Cosmochimica Acta*, v. 69, p. 497–503.
- 21  
22 860 Jugo, P. J., 2009, Sulfur content at sulfide saturation in oxidized magmas: *Geology*, v. 37,  
23 861 p. 415–418.
- 24  
25 862 Keith, J., Whitney, J., Hattori, K., Ballantyne, G., Christiansen, E., Barr, D., Cannan, T.,  
26 863 and Hook, C., 1997, The role of magmatic sulfides and mafic alkaline magmas in the  
27 864 Bingham and Tintic mining districts, Utah: *Journal of Petrology*, v. 38, p. 1679–1690.
- 28  
29 865 Konecke, B. A., Fiege, A., Simon, A. C., and Holtz, F., 2017a, Cryptic metasomatism  
30 866 during late-stage lunar magmatism implicated by sulfur in apatite: *Geology*, p. 739–  
31 867 742.
- 32  
33 868 Konecke, B. A., Fiege, A., Simon, A. C., Parat, F., and Stechern, A., 2017b, Co-  
34 869 variability of S<sup>6+</sup>, S<sup>4+</sup>, and S<sup>2-</sup> in apatite as a function of oxidation state: Implications  
35 870 for a new oxybarometer: *American Mineralogist*, v. 102, p. 548–557.
- 36  
37 871 Lang, J. R., Lueck, B., Mortensen, J. K., Russell, J. K., Stanley, C. R., and Thompson, J.  
38 872 F., 1995, Triassic-Jurassic silica-undersaturated and silica-saturated alkalic intrusions  
39 873 in the Cordillera of British Columbia: Implications for arc magmatism: *Geology*, v. 23,  
40 874 p. 451–454.
- 41  
42 875 Lange, R. A., Frey, H. M., and Hector, J., 2009, A thermodynamic model for the  
43 876 plagioclase-liquid hygrometer/thermometer: *American Mineralogist*, v. 94, p. 494–506.
- 44  
45 877 Large, S.J.E., von Quadt, A., Wotzlaw, J.-F., Guillong, M., and Heinrich, C.A., 2018,  
46 878 Magma evolution leading to porphyry Au-Cu mineralization at the Ok Tedi Deposit,  
47 879 Papua New Guinea: trace element geochemistry and high-precision geochronology of  
48 880 igneous zircon: *Economic Geology*, v. 113, p. 39–61.
- 49  
50 881 Larocque, A. C., Stimac, J. A., Keith, J. D., and Huminicki, M. A., 2000, Evidence for  
51 882 open-system behavior in immiscible Fe–S–O liquids in silicate magmas: implications

1  
2  
3  
4 883 for contributions of metals and sulfur to ore-forming fluids: The Canadian  
5 884 Mineralogist, v. 38, p. 1233–1249.  
6  
7 885 Li, J., Li, G., Qin, K., Xiao, B., Chen, L., and Zhao, J., 2012, Mineralogy and mineral  
8 886 chemistry of the Cretaceous Duolong gold-rich porphyry copper deposit in the  
9 887 Bangongco arc, northern Tibet: Resource Geology, v. 62, p. 19–41.  
10 888 Li, Y., Selby, D., Feely, M., Costanzo, A., and Li, X.-H., 2017, Fluid inclusion  
11 889 characteristics and molybdenite Re-Os geochronology of the Qulong porphyry copper-  
12 890 molybdenum deposit, Tibet: Mineralium Deposita, v.52, p. 137–158.  
13 891 Liang, H.-Y., Campbell, I. H., Allen, C., Sun, W.-D., Liu, C.-Q., Yu, H.-X., Xie, Y.-W.,  
14 892 and Zhang, Y.-Q., 2006, Zircon  $Ce^{4+}/Ce^{3+}$  ratios and ages for Yulong ore-bearing  
15 893 porphyries in eastern Tibet: Mineralium Deposita, v. 41, p. 152–159.  
16 894 Loader, M. A., Wilkinson, J. J., and Armstrong, R. N., 2017, The effect of titanite  
17 895 crystallisation on Eu and Ce anomalies in zircon and its implications for the  
18 896 assessment of porphyry Cu deposit fertility: Earth and Planetary Science Letters, v.  
19 897 472, p. 107–119.  
20 898 Loucks, R.R., 2013, Distinctive composition and genesis of copper ore-forming arc  
21 899 magmas: Goldschmidt Conference 2013 Abstracts: Mineralogical Magazine, v. 77, p.  
22 900 1642.  
23 901 Locock, A. J., 2014, An Excel spreadsheet to classify chemical analyses of amphiboles  
24 902 following the IMA 2012 recommendations: Computers & Geosciences, v. 62, p. 1–11.  
25 903 Logan, J. M., and Mihalynuk, M. G., 2014, Tectonic controls on Early Mesozoic paired  
26 904 alkaline porphyry deposit belts (Cu-Au ± Ag-Pt-Pd-Mo) within the Canadian  
27 905 Cordillera: Economic Geology, v. 109, p. 827–858.  
28 906 Loucks, R., 2014, Distinctive composition of copper-ore-forming arc magmas: Australian  
29 907 Journal of Earth Sciences, v. 61, p. 5–16.  
30 908 Lowell, J. D., and Guilbert, J. M., 1970, Lateral and vertical alteration-mineralization  
31 909 zoning in porphyry ore deposits: Economic Geology, v. 65, p. 373–408.  
32 910 Lu, Y.-J., Loucks, R. R., Fiorentini, M. L., Yang, Z.-M., and Hou, Z.-Q., 2015, Fluid flux  
33 911 melting generated postcollisional high Sr/Y copper ore-forming water-rich magmas in  
34 912 Tibet: Geology, v.43, p. 583–586.  
35 913 Lu, Y.-J., Loucks, R. R., Fiorentini, M., McCuaig, T. C., Evans, N. J., Yang, Z.-M., Hou,  
36 914 Z.-Q., Kirkland, C. L., Parra-Avila, L. A., and Kobussen, A., 2016, Zircon  
37 915 compositions as a pathfinder for Cu±Mo±Au deposits: Society of Economic  
38 916 Geologists Special Publication, v. 19, p. 329–347.  
39 917 Mao, M., Rukhlov, A. S., Rowins, S. M., Spence, J., and Coogan, L. A., 2016, Apatite  
40 918 trace element compositions: A robust new tool for mineral exploration: Economic  
41 919 Geology, v. 111, p. 1187–1222.  
42  
43  
44  
45  
46  
47  
48  
49  
50  
51  
52  
53  
54  
55  
56  
57  
58  
59  
60  
61  
62  
63  
64  
65



- 1  
2  
3  
4 920 Marsden, H., and Thorkelson, D. J., 1992, Geology of the Hazelton volcanic belt in  
5  
6 921 British Columbia: implications for the Early to Middle Jurassic evolution of Stikinia:  
7  
8 922 Tectonics, v. 11, p. 1266–1287.
- 9 923 Masterman, G. J., Cooke, D. R., Berry, R. F., Clark, A. H., Archibald, D. A., Mathur, R.,  
10  
11 924 Walshe, J. L., and Durán, M., 2004,  $^{40}\text{Ar}/^{39}\text{Ar}$  and Re-Os geochronology of porphyry  
12  
13 925 copper-molybdenum deposits and related copper-silver veins in the Collahuasi district,  
14  
15 926 northern Chile: Economic Geology, v. 99, p. 673–690.
- 16 927 Mathez, E. A., 1973, Refinement of the Kudo-Weill plagioclase thermometer and its  
17  
18 928 application to basaltic rocks: Contributions to Mineralogy and Petrology, v. 41, p. 61–  
19  
20 929 72.
- 21 930 Mathez, E.A., 1984, Influence of degassing on oxidation-states of basaltic magmas:  
22  
23 931 Nature, v. 310, p. 371–375.
- 24 932 Mathez, E. A., and Webster, J. D., 2005, Partitioning behavior of chlorine and fluorine in  
25  
26 933 the system apatite-silicate melt-fluid: Geochimica et Cosmochimica Acta, v. 69, p.  
27  
28 934 1275–1286.
- 29 935 Matzel, J. E., Bowring, S. A., and Miller, R. B., 2006, Time scales of pluton construction  
30  
31 936 at differing crustal levels: Examples from the Mount Stuart and Tenpeak intrusions,  
32  
33 937 North Cascades, Washington: Geological Society of America Bulletin, v. 118, p.  
34  
35 938 1412–1430.
- 36 939 McMillan, W.J., Thompson, J.F.H., Hart, C.J.R., and Johnston, S.T., 1995, Regional  
37  
38 940 geological and tectonic setting of porphyry deposits in British Columbia and Yukon  
39  
40 941 Territory: Canadian Institute of Mining, Metallurgy and Petroleum Special Volume 46,  
41  
42 942 p. 40–57.
- 43 943 Merzbacher, C., and Eggler, D.H., 1984, A magmatic geohygrometer: Application to  
44  
45 944 Mount St. Helens and other dacitic magmas: Geology, v. 12, p. 587–590.
- 46 945 Micko, J., Tosdal, R. M., Bissig, T., Chamberlain, C. M., and Simpson, K. A., 2014,  
47  
48 946 Hydrothermal alteration and mineralization of the Galore Creek alkalic Cu-Au  
49  
50 947 porphyry deposit, northwestern British Columbia, Canada: Economic Geology, v. 109,  
51  
52 948 p. 891–914.
- 53 949 Mihalyuk, M., Erdmer, P., Ghent, E., Cordey, F., Archibald, D., Friedman, R., and  
54  
55 950 Johannson, G., 2004, Coherent French Range blueschist: Subduction to exhumation  
56  
57 951 in < 2.5 my?: Geological Society of America Bulletin, v. 116, p. 910–922.
- 58 952 Monger, J. W. H., and Irving, E., 1980, Northward displacement of north-central British  
59  
60 953 Columbia: Nature, v. 285, p. 289–294.
- 61 954 Moore, G., and Carmichael, I., 1998, The hydrous phase equilibria (to 3 kbar) of an  
62  
63 955 andesite and basaltic andesite from western Mexico: constraints on water content and  
64  
65

1  
2  
3  
4  
5  
6  
7  
8  
9  
10  
11  
12  
13  
14  
15  
16  
17  
18  
19  
20  
21  
22  
23  
24  
25  
26  
27  
28  
29  
30  
31  
32  
33  
34  
35  
36  
37  
38  
39  
40  
41  
42  
43  
44  
45  
46  
47  
48  
49  
50  
51  
52  
53  
54  
55  
56  
57  
58  
59  
60  
61  
62  
63  
64  
65

956 conditions of phenocryst growth: *Contributions to Mineralogy and Petrology*, v. 130, p.  
957 304–319.

958 Mortensen, J.K., Ghosh, D.K., and Ferri, F., 1995, U-Pb geochronology of intrusive rocks  
959 associated with copper-gold porphyry deposits in the Canadian Cordillera: *Canadian  
960 Institute of Mining, Metallurgy and Petroleum, Special Volume 46*, p. 142–158.

961 Mutch, E., Blundy, J., Tattitch, B., Cooper, F., and Brooker, R., 2016, An experimental  
962 study of amphibole stability in low-pressure granitic magmas and a revised Al-in-  
963 hornblende geobarometer: *Contributions to Mineralogy and Petrology*, v. 171, 85, doi:  
964 10.1007/s00410-016-1298-9

965 Myers, J. t., and Eugster, H., 1983, The system Fe-Si-O: Oxygen buffer calibrations to  
966 1,500 K: *Contributions to Mineralogy and Petrology*, v. 82, p. 75–90.

967 Nadeau, O., Williams-Jones, A. E., and Stix, J., 2010, Sulphide magma as a source of  
968 metals in arc-related magmatic hydrothermal ore fluids: *Nature Geoscience*, v. 3, p.  
969 501–505.

970 Nadeau, O., Stix, J., and Williams-Jones, A. E., 2016, Links between arc volcanoes and  
971 porphyry-epithermal ore deposits: *Geology*, v. 44, p. 11–14.

972 Naney, M. T., 1983, Phase equilibria of rock-forming ferromagnesian silicates in granitic  
973 systems: *American Journal of Science*, v. 283, p. 993–1033.

974 Nelson, J., and Colpron, M., 2007, Tectonics and metallogeny of the British Columbia,  
975 Yukon and Alaskan Cordillera, 1.8 Ga to the present: *Mineral deposits of Canada: a  
976 synthesis of major deposit-types, district metallogeny, the evolution of geological  
977 provinces, and exploration methods: Geological Association of Canada, Mineral  
978 Deposits Division, Special Publication*, v. 5, p. 755–791.

979 Nelson, J., Colpron, M., and Israel, S., 2013, The Cordillera of British Columbia, Yukon,  
980 and Alaska: Tectonics and metallogeny: *Society of Economic Geologists Special  
981 Publication*, v. 17, p. 53–109.

982 Newell, J.M., and Peatfield, G.R., 1995, The Red Chris porphyry copper-gold deposit:  
983 *Canadian Institute of Mining and Metallurgy Special Volume 46*,  
984 p. 674–688.

985 Norris, J.R., 2012, Evolution of alteration and mineralization at the Red Chris Cu-Au  
986 porphyry deposit East zone, northwestern British Columbia, Canada: M.Sc. thesis,  
987 Vancouver, Canada, University of British Columbia, 194 p.

988 Pan, L.-C., Hu, R.-Z., Wang, X.-S., Bi, X.-W., Zhu, J.-J., and Li, C., 2016, Apatite trace  
989 element and halogen compositions as petrogenetic-metallogenic indicators: Examples  
990 from four granite plutons in the Sanjiang region, SW China: *Lithos*, v. 254–255, p.  
991 118–130.

1  
2  
3  
4  
5  
6  
7  
8  
9  
10  
11  
12  
13  
14  
15  
16  
17  
18  
19  
20  
21  
22  
23  
24  
25  
26  
27  
28  
29  
30  
31  
32  
33  
34  
35  
36  
37  
38  
39  
40  
41  
42  
43  
44  
45  
46  
47  
48  
49  
50  
51  
52  
53  
54  
55  
56  
57  
58  
59  
60  
61  
62  
63  
64  
65

992 Parat, F., and Holtz, F., 2005, Sulfur partition coefficient between apatite and rhyolite:  
993 the role of bulk S content: *Contributions to Mineralogy and Petrology*, v. 150, p. 643–  
994 651.

995 Parat, F., Holtz, F., and Klügel, A., 2011, S-rich apatite-hosted glass inclusions in  
996 xenoliths from La Palma: constraints on the volatile partitioning in evolved alkaline  
997 magmas: *Contributions to Mineralogy and Petrology*, v. 162, p. 463–478.

998 Pass, H. E., Cooke, D. R., Davidson, G., Maas, R., Dipple, G., Rees, C., Ferreira, L.,  
999 Taylor, C., and Deyell, C. L., 2014, Isotope geochemistry of the northeast zone,  
1000 Mount Polley alkalic Cu-Au-Ag porphyry deposit, British Columbia: A case for  
1001 carbonate assimilation: *Economic Geology*, v. 109, p. 859–890.

1002 Patchett, P., Gehrels, G. E., and Isachsen, C., 1998, Nd isotopic characteristics of  
1003 metamorphic and plutonic rocks of the Coast Mountains near Prince Rupert, British  
1004 Columbia: *Canadian Journal of Earth Sciences*, v. 35, p. 556–561.

1005 Paterson, S. R., Okaya, D., Memeti, V., Economos, R., and Miller, R. B., 2011, Magma  
1006 addition and flux calculations of incrementally constructed magma chambers in  
1007 continental margin arcs: Combined field, geochronologic, and thermal modeling  
1008 studies: *Geosphere*, v. 7, p. 1439–1468.

1009 Pearce, T. H., and Kolisnik, A. M., 1990, Observations of plagioclase zoning using  
1010 interference imaging: *Earth-Science Reviews*, v. 29, p. 9–26.

1011 Pearce, J., 1996, Sources and settings of granitic rocks: *Episodes*, v. 19, p. 120–125.

1012 Peng, G., Luhr, J. F., and McGee, J. J., 1997, Factors controlling sulfur concentrations in  
1013 volcanic apatite: *American Mineralogist*, v. 82, p. 1210–1224.

1014 Piccoli, P., and Candela, P., 1994, Apatite in felsic rocks; a model for the estimation of  
1015 initial halogen concentrations in the Bishop Tuff (Long Valley) and Tuolumne  
1016 Intrusive Suite (Sierra Nevada Batholith) magmas: *American Journal of Science*, v.  
1017 294, p. 92–135.

1018 Piccoli, P. M., and Candela, P. A., 2002, Apatite in igneous systems: *Reviews in*  
1019 *Mineralogy and Geochemistry*, v. 48, p. 255–292.

1020 Pilet, S., Baker, M. B., Müntener, O., and Stolper, E. M., 2011, Monte Carlo simulations  
1021 of metasomatic enrichment in the lithosphere and implications for the source of  
1022 alkaline basalts: *Journal of Petrology*, v. 52, p. 1415–1442.

1023 Qiu, J.-T., Li, P.-J., Santosh, M., and Yu, X.-Q., 2014, Magma oxygen fugacities of  
1024 granitoids in the Xiaolinling area, central China: implications for regional tectonic  
1025 setting: *Neues Jahrbuch für Mineralogie-Abhandlungen (Journal of Mineralogy and*  
1026 *Geochemistry)*, v. 191, p. 317–329.

1027 Rees, C., Riedell, K. B., Proffett, J. M., Macpherson, J., and Robertson, S., 2015, The  
1028 Red Chris porphyry copper-gold deposit, Northern British Columbia, Canada: *Igneous*

- 1  
2  
3  
4 1029 phases, alteration, and controls of mineralization: *Economic Geology*, v. 110, p. 857–  
5 888.  
6 1030  
7 1031 Rezeau, H., Moritz, R., Wotzlaw, J.-F., Tayan, R., Melkonyan, R., Ulianov, A., Selby, D.,  
8 d’Abzac, F.-X., and Stern, R. A., 2016, Temporal and genetic link between  
9 1032 incremental pluton assembly and pulsed porphyry Cu-Mo formation in accretionary  
10 1033 orogens: *Geology*, v. 44, p. 627–630.  
11 1034  
12 1035 Richards, J. P., 2003, Tectono-magmatic precursors for porphyry Cu-(Mo-Au) deposit  
13 1036 formation: *Economic Geology*, v. 98, p. 1515–1533.  
14 1037  
15 1038 Richards, J. P., 2009, Postsubduction porphyry Cu-Au and epithermal Au deposits:  
16 1039 Products of remelting of subduction-modified lithosphere: *Geology*, v. 37, p. 247–250.  
17 1040  
18 1041 Richards, J.P., 2011, Magmatic to hydrothermal metal fluxes in convergent and collided  
19 1042 margins: *Ore Geology Reviews*, v. 40, p. 1–26.  
20 1043  
21 1044 Richards, J. P., 2015, The oxidation state, and sulfur and Cu contents of arc magmas:  
22 1045 implications for metallogeny: *Lithos*, v. 233, p. 27–45.  
23 1046  
24 1047 Richards, J. P., and Kerrich, R., 2007, Special Paper: Adakite-like rocks: their diverse  
25 1048 origins and questionable role in metallogenesis: *Economic Geology*, v. 102, p. 537–  
26 1049 576.  
27 1050  
28 1051 Richards, J. P., López, G. P., Zhu, J.-J., Creaser, R. A., Locock, A. J., and Mumin, A. H.,  
29 1052 2017, Contrasting tectonic settings and sulfur contents of magmas associated with  
30 1053 Cretaceous porphyry Cu ± Mo ± Au and intrusion-related iron oxide Cu-Au deposits  
31 1054 in northern Chile: *Economic Geology*, v. 112, p. 295–318.  
32 1055  
33 1056 Ricketts, B. D., Evenchick, C. A., Anderson, R. G., and Murphy, D. C., 1992, Bowser  
34 1057 basin, northern British Columbia: Constraints on the timing of initial subsidence and  
35 1058 Stikinia-North America terrane interactions: *Geology*, v. 20, p. 1119–1122.  
36 1059  
37 1060 Ridolfi, F., Renzulli, A., and Puerini, M., 2010, Stability and chemical equilibrium of  
38 1061 amphibole in calc-alkaline magmas: an overview, new thermobarometric formulations  
39 1062 and application to subduction-related volcanoes: *Contributions to Mineralogy and  
40 1063 Petrology*, v. 160, p. 45–66.  
41 1064  
42 1065 Rohrlach, B.D., and Loucks, R.R., 2005, Multi-million-year cyclic ramp-up of volatiles  
43 1066 in a lower crustal magma reservoir trapped below the Tampakan copper-gold deposit  
44 1067 by Mio-Pliocene crustal compression in the southern Philippines, *in* Porter, T.M., ed.,  
45 1068 Super porphyry copper and gold deposits: A global perspective: PGC Publishing,  
46 1069 Adelaide, South Australia, v. 2, p. 369–407.  
47 1070  
48 1071 Rutherford, M.J., and Devine, J.D., 1988, The May 18, 1980, eruption of Mount St.  
49 1072 Helens. 3. Stability and chemistry of amphibole in the magma chamber: *Journal of  
50 1073 Geophysical Research*, v. 93, p. 11,949–11,959.  
51 1074  
52  
53  
54  
55  
56  
57  
58  
59  
60  
61  
62  
63  
64  
65

1  
2  
3  
4 1065 Rutherford, M. J., and Devine, J. D., 2003, Magmatic conditions and magma ascent as  
5 indicated by hornblende phase equilibria and reactions in the 1995–2002 Soufriere  
6 1066 Hills magma: *Journal of Petrology*, v. 44, p. 1433–1453.  
7 1067  
8 1068 Samson, S. D., McClelland, W. C., Patchett, P. J., Gehrels, G. E., and Anderson, R. G.,  
9 1069 1989, Evidence from neodymium isotopes for mantle contributions to Phanerozoic  
10 1070 crustal genesis in the Canadian Cordillera: *Nature*, v. 337, p. 705–709.  
11 1071 Samson, S. D., Patchett, P. J., McClelland, W. C., and Gehrels, G. E., 1991, Nd and Sr  
12 1072 isotopic constraints on the petrogenesis of the west side of the northern Coast  
13 1073 Mountains batholith, Alaskan and Canadian Cordillera: *Canadian Journal of Earth  
14 1074 Sciences*, v. 28, p. 939–946.  
15 1075 Schaltegger, U., Brack, P., Ovtcharova, M., Peytcheva, I., Schoene, B., Stracke, A.,  
16 1076 Marocchi, M., and Bargossi, G. M., 2009, Zircon and titanite recording 1.5 million  
17 1077 years of magma accretion, crystallization and initial cooling in a composite pluton  
18 1078 (southern Adamello batholith, northern Italy): *Earth and Planetary Science Letters*, v.  
19 1079 286, p. 208–218.  
20 1080 Scott, J.E., Richards, J.P., Heaman, L.M., Creaser, R.A., and Salazar, G.S., 2008, The  
21 1081 Schaft Creek porphyry Cu-Mo-(Au) deposit, Northwestern British Columbia:  
22 1082 *Exploration and Mining Geology*, v. 17, p. 163–196.  
23 1083 Sedorff, E., Dilles, J., Proffett, J., Einaudi, M., Zurcher, L., Stavast, W., Johnson, D.,  
24 1084 and Barton, M., 2005, Porphyry deposits: Characteristics and origin of hypogene  
25 1085 features: *Economic Geology 100th anniversary volume*, v. 29, p. 251–298.  
26 1086 Selby, D., and Creaser, R. A., 2004, Macroscale NTIMS and microscale LA-MC-ICP-  
27 1087 MS Re-Os isotopic analysis of molybdenite: Testing spatial restrictions for reliable  
28 1088 Re-Os age determinations, and implications for the decoupling of Re and Os within  
29 1089 molybdenite: *Geochimica et Cosmochimica Acta*, v. 68, p. 3897–3908.  
30 1090 Shen, P., Hattori, K., Pan, H., Jackson, S., and Seitmuratova, E., 2015, Oxidation  
31 1091 condition and metal fertility of granitic magmas: zircon trace-element data from  
32 1092 porphyry Cu deposits in the Central Asian Orogenic Belt: *Economic Geology*, v. 110,  
33 1093 p. 1861–1878.  
34 1094 Sillitoe, R., 2010, Porphyry copper systems: *Economic Geology*, v. 105, p. 3–41.  
35 1095 Simon, A. C., and Ripley, E. M., 2011, The role of magmatic sulfur in the formation of  
36 1096 ore deposits: *Reviews in Mineralogy and Geochemistry*, v. 73, p. 513–578.  
37 1097 Steinberger, I., Hinks, D., Driesner, T., and Heinrich, C.A., 2013, Source plutons driving  
38 1098 porphyry copper ore formation: combining geomagnetic data, thermal constraints, and  
39 1099 chemical mass balance to quantify the magma chamber beneath the Bingham Canyon  
40 1100 deposit: *Economic Geology*, v. 108, p. 605–624.  
41  
42  
43  
44  
45  
46  
47  
48  
49  
50  
51  
52  
53  
54  
55  
56  
57  
58  
59  
60  
61  
62  
63  
64  
65

1  
2  
3  
4  
5  
6  
7  
8  
9  
10  
11  
12  
13  
14  
15  
16  
17  
18  
19  
20  
21  
22  
23  
24  
25  
26  
27  
28  
29  
30  
31  
32  
33  
34  
35  
36  
37  
38  
39  
40  
41  
42  
43  
44  
45  
46  
47  
48  
49  
50  
51  
52  
53  
54  
55  
56  
57  
58  
59  
60  
61  
62  
63  
64  
65

1101 Stern, C. R., Funk, J. A., Skewes, M. A., and Arévalo, A., 2007, Magmatic anhydrite in  
1102 plutonic rocks at the El Teniente Cu-Mo deposit, Chile, and the role of sulfur-and  
1103 copper-rich magmas in its formation: *Economic geology*, v. 102, p. 1335–1344.

1104 Stock, M. J., Humphreys, M. C. S., Smith, V. C., Isaia, R., and Pyle, D. M., 2016, Late-  
1105 stage volatile saturation as a potential trigger for explosive volcanic eruptions: *Nature*  
1106 *Geosciences*, v. 9, p. 249–254.

1107 Streck, M. J., and Dilles, J. H., 1998, Sulfur evolution of oxidized arc magmas as  
1108 recorded in apatite from a porphyry copper batholith: *Geology*, v. 26, p. 523–526.

1109 Sun, S.-S., and McDonough, W., 1989, Chemical and isotopic systematics of oceanic  
1110 basalts: implications for mantle composition and processes: Geological Society,  
1111 London, Special Publications, v. 42, p. 313–345.

1112 Tapster, S., Condon, D., Naden, J., Noble, S., Petterson, M., Roberts, N., Saunders, A.,  
1113 and Smith, D. J., 2016, Rapid thermal rejuvenation of high-crystallinity magma linked  
1114 to porphyry copper deposit formation; evidence from the Koloula Porphyry Prospect,  
1115 Solomon Islands: *Earth and Planetary Science Letters*, v. 442, p. 206–217.

1116 Taseko Mines Limited, 2013, Gibraltar reserves and resources at December 31, 2012:  
1117 Taseko Mines Limited Report, [www.tasekomines.com/gibraltar/ID540174](http://www.tasekomines.com/gibraltar/ID540174).

1118 Titley, S.R., and Beane, R.E., 1981, Porphyry copper deposits, Part 1. Geologic settings,  
1119 petrology, and tectogenesis: *Economic Geology 75<sup>TH</sup> Anniversary Volume*, p. 214–  
1120 235.

1121 Trail, D., Watson, E. B., and Tailby, N. D., 2011, The oxidation state of Hadean magmas  
1122 and implications for early Earth's atmosphere: *Nature*, v. 480, p. 79–82.

1123 Ustunisik, G., Kilinc, A., and Nielsen, R. L., 2014, New insights into the processes  
1124 controlling compositional zoning in plagioclase: *Lithos*, v. 200, p. 80–93.

1125 Von Quadt, A., Erni, M., Martinek, K., Moll, M., Peytcheva, I., and Heinrich, C. A., 2011,  
1126 Zircon crystallization and the lifetimes of ore-forming magmatic-hydrothermal  
1127 systems: *Geology*, v. 39, p. 731–734.

1128 Walker Jr, B. A., Miller, C. F., Lowery Claiborne, L., Wooden, J. L., and Miller, J. S.,  
1129 2007, Geology and geochronology of the Spirit Mountain batholith, southern Nevada:  
1130 Implications for timescales and physical processes of batholith construction: *Journal*  
1131 *of Volcanology and Geothermal Research*, v. 167, p. 239–262.

1132 Wallace, P. J., 2005, Volatiles in subduction zone magmas: concentrations and fluxes  
1133 based on melt inclusion and volcanic gas data: *Journal of Volcanology and*  
1134 *Geothermal Research*, v. 140, p. 217–240.

1135 Wang, R., Richards, J. P., Hou, Z., Yang, Z., and DuFrane, S. A., 2014a, Increased  
1136 magmatic water content—the key to Oligo-Miocene porphyry Cu-Mo ± Au formation  
1137 in the Eastern Gangdese Belt, Tibet: *Economic Geology*, v. 109, p. 1315–1339.

1  
2  
3  
4  
5  
6  
7  
8  
9  
10  
11  
12  
13  
14  
15  
16  
17  
18  
19  
20  
21  
22  
23  
24  
25  
26  
27  
28  
29  
30  
31  
32  
33  
34  
35  
36  
37  
38  
39  
40  
41  
42  
43  
44  
45  
46  
47  
48  
49  
50  
51  
52  
53  
54  
55  
56  
57  
58  
59  
60  
61  
62  
63  
64  
65

1138 Wang, R., Richards, J. P., Hou, Z.-q., Yang, Z.-m., Gou, Z.-b., and DuFrane, S. A., 2014b,  
1139 Increasing magmatic oxidation state from Paleocene to Miocene in the Eastern  
1140 Gangdese Belt, Tibet: Implication for collision-related porphyry Cu-Mo ± Au  
1141 mineralization: *Economic Geology*, v. 109, p. 1943–1965.

1142 Waters, L. E., and Lange, R. A., 2015, An updated calibration of the plagioclase-liquid  
1143 hygrometer-thermometer applicable to basalts through rhyolites: *American*  
1144 *Mineralogist*, v. 100, p. 2172–2184.

1145 Webster, J. D., 1997, Chloride solubility in felsic melts and the role of chloride in  
1146 magmatic degassing: *Journal of Petrology*, v. 38, p. 1793–1807.

1147 Webster, J. D., Kinzler, R. J., and Mathez, E. A., 1999, Chloride and water solubility in  
1148 basalt and andesite melts and implications for magmatic degassing: *Geochimica et*  
1149 *Cosmochimica Acta*, v. 63, p. 729–738.

1150 Webster, J. D., Tappen, C. M., and Mandeville, C. W., 2009, Partitioning behavior of  
1151 chlorine and fluorine in the system apatite–melt–fluid. II: Felsic silicate systems at 200  
1152 MPa: *Geochimica et Cosmochimica Acta*, v. 73, p. 559–581.

1153 Webster, J., Goldoff, B., Sintoni, M., Shimizu, N., and De Vivo, B., 2014, C–O–H–Cl–  
1154 S–F volatile solubilities, partitioning, and mixing in phonolitic–trachytic melts and  
1155 aqueous–carbonic vapor ± saline liquid at 200 MPa: *Journal of Petrology*, v. 55, p.  
1156 2217–2248.

1157 Webster, J. D., and Piccoli, P. M., 2015, Magmatic apatite: A powerful, yet deceptive,  
1158 mineral: *Elements*, v. 11, p. 177–182.

1159 Weis, P., Driesner, T., and Heinrich, C., 2012, Porphyry-copper ore shells form at stable  
1160 pressure-temperature fronts within dynamic fluid plumes: *Science*, v. 338, p. 1613–  
1161 1616.

1162 Wilkinson, J. J., 2013, Triggers for the formation of porphyry ore deposits in magmatic  
1163 arcs: *Nature Geoscience*, v. 6, p. 917–925.

1164 Winchester, J.A., and Floyd, P.A., 1977, Geochemical discrimination of different magma  
1165 series and their differentiation products using immobile elements: *Chemical Geology*,  
1166 v. 20, p. 325–343.

1167 Xu, L., Bi, X., Hu, R., Qi, Y., Tang, Y., Wang, X., and Zhu, J., 2016, Redox states and  
1168 genesis of magmas associated with intra-continental porphyry Cu–Au mineralization  
1169 within the Jinshajiang–Red River alkaline igneous belt, SW China: *Ore Geology*  
1170 *Reviews*, v. 73, Part 2, p. 330–345.

1171 Yang, Z., Hou, Z., White, N. C., Chang, Z., Li, Z., and Song, Y., 2009, Geology of the  
1172 post-collisional porphyry copper–molybdenum deposit at Qulong, Tibet: *Ore Geology*  
1173 *Reviews*, v. 36, p. 133–159.

1  
2  
3  
4  
5  
6  
7  
8  
9  
10  
11  
12  
13  
14  
15  
16  
17  
18  
19  
20  
21  
22  
23  
24  
25  
26  
27  
28  
29  
30  
31  
32  
33  
34  
35  
36  
37  
38  
39  
40  
41  
42  
43  
44  
45  
46  
47  
48  
49  
50  
51  
52  
53  
54  
55  
56  
57  
58  
59  
60  
61  
62  
63  
64  
65

1174 Zajacz, Z., Seo, J.H., Candela, P.A., Piccoli, P.M., and Tossell, J.A., 2011, The solubility  
1175 of copper in high-temperature magmatic vapors: A quest for the significance of  
1176 various chloride and sulfide complexes: *Geochimica et Cosmochimica Acta*, v. 75, p.  
1177 2811–2827.

1178 Zajacz, Z., Candela, P.A., Piccoli, P.M., Wälle, M., and Sanchez-Valle, C., 2012, Gold  
1179 and copper in volatile saturated mafic to intermediate magmas: Solubilities,  
1180 partitioning, and implications for ore deposit formation: *Geochimica et Cosmochimica*  
1181 *Acta*, v. 91, p. 140–159.

1182 Zhang, C., Holtz, F., Ma, C., Wolff, P. E., and Li, X., 2012, Tracing the evolution and  
1183 distribution of F and Cl in plutonic systems from volatile-bearing minerals: a case  
1184 study from the Liujiawa pluton (Dabie orogen, China): *Contributions to Mineralogy*  
1185 *and Petrology*, v. 164, p. 859–879.

1186 Zhang, D., and Audétat, A., 2017, What caused the formation of the giant Bingham  
1187 Canyon porphyry Cu-Mo-Au deposit? Insights from melt Inclusions and magmatic  
1188 sulfides: *Economic Geology*, v. 112, p. 221–244.

1189 Zimmer, M.M., Plank, T., Hauri, E.H., Yogodzinski, G.M., Stelling, P., Larsen, J., Singer,  
1190 B., Jicha, B., Mandeville, C., and Nye, C.J., 2010, The role of water in generating the  
1191 calc-alkaline trend: New volatile data for Aleutian magmas and a new Tholeiitic Index:  
1192 *Journal of Petrology*, v. 51, p. 2411–2444.

1193 Zhu, C., and Sverjensky, D. A., 1991, Partitioning of F-Cl-OH between minerals and  
1194 hydrothermal fluids: *Geochimica et Cosmochimica Acta*, v. 55, p. 1837–1858.



1  
2  
3  
4 **1195 Figure Captions**

5  
6 **1196** Fig. 1. Major terranes in the south of the Canadian Cordillera, showing Triassic to  
7  
8  
9 **1197** Jurassic magmatic belts and major associated porphyry deposits in the Stikine and  
10  
11 **1198** Quesnel terranes (modified from Nelson and Colpron, 2007; Nelson et al., 2013; original  
12  
13 **1199** graphics file provided by Joanne Nelson, British Columbia Geological Survey of Canada).  
14  
15 **1200** The age of the Red Chris deposit is from this study (Table 1), and the ages for the other  
16  
17 **1201** porphyry deposits are from Brown and Kahlert (1986; Red Mountain), Mortensen et al.  
18  
19 **1202** (1995; Mt. Polley), Scott et al. (2008; Schaft Creek), Duuring et al. (2009; Kemess  
20  
21 **1203** South), Taseko Mines Limited (2013; Gibraltar), Bath et al. (2014; Lorraine), Byrne and  
22  
23 **1204** Tosdal (2014; Galore Creek), Devine et al. (2014; Lorraine), Logan and Mihalynuk (2014;  
24  
25 **1205** Highland Valley, Copper Mountaine, Afton/Ajax, and Brenda), and Jago et al. (2014; Mt.  
26  
27 **1206** Milligan).  
28  
29  
30  
31  
32

33 **1207**

34  
35 **1208** Fig. 2. Simplified geological map of the Red Stock and Red Chris Cu-Au deposit,  
36  
37 **1209** showing the main mineralized zoned (named) and the locations of sampled drill holes  
38  
39 **1210** (modified from Rees et al., 2015). Universal Transverse Mercator coordinates are based  
40  
41 **1211** on the WGS84 datum.  
42  
43  
44  
45

46 **1212**

47  
48 **1213** Fig. 3. Hand specimen photographs of samples of the P1, P2E, P2L, and P3 porphyry  
49  
50 **1214** intrusions, and two late basaltic to andesitic dikes. (A) P1 porphyry with anhedral to  
51  
52 **1215** subhedral altered amphibole and plagioclase phenocrysts, crosscut by pyrite-quartz veins  
53  
54 **1216** (sample RC13-35). (B) P2E porphyry showing crowded texture with chloritized  
55  
56 **1217** amphibole and plagioclase phenocrysts; plagioclase grains are rimmed or replaced by  
57  
58  
59  
60  
61  
62  
63  
64  
65

1  
2  
3  
4  
5  
6  
7  
8  
9  
10  
11  
12  
13  
14  
15  
16  
17  
18  
19  
20  
21  
22  
23  
24  
25  
26  
27  
28  
29  
30  
31  
32  
33  
34  
35  
36  
37  
38  
39  
40  
41  
42  
43  
44  
45  
46  
47  
48  
49  
50  
51  
52  
53  
54  
55  
56  
57  
58  
59  
60  
61  
62  
63  
64  
65

1218 secondary K-feldspar. The brick-red color is due to fine-grained hematite (sample RC13-  
1219 107). (C) P2L porphyry composed of abundant fresh amphibole and plagioclase  
1220 phenocrysts, with quartz in the groundmass (sample RC13-32). (D) The P3 porphyry is  
1221 similar to P2L, but is distinguished by the absence of quartz in the groundmass (sample  
1222 RC13-78). (E) Andesitic dike with anhedral to subhedral amphibole phenocrysts, crosscut  
1223 by a small calcite vein (sample RC13-62). (F) Basaltic dike with chloritized amphibole  
1224 phenocrysts (sample RC13-106). See Digital Appendix Table A1 for sample locations.

1225  
1226 Fig. 4. West-southwest–east-northeast cross section A–A’, and north-northwest–south-  
1227 southwest cross section B–B’ (location of sections shown in Fig. 2), modified from  
1228 Gillstrom et al. (2012) and Rees et al. (2015). Copper equivalent-grade zones, drill holes,  
1229 and the boundary between potassic and post-potassic zones are shown: Cu equivalent (%)  
1230 =  $\text{Cu (\%)} + 0.486 \times \text{Au (g/t)}$ .

1231  
1232 Fig. 5. Hand specimen photographs and photomicrographs of alteration and vein minerals.  
1233 (A, B) P2E porphyry (samples RC13-81 and RC13-75) with potassic alteration and A-  
1234 type quartz veins comprising magnetite, secondary K-feldspar, and disseminated bornite  
1235 and pyrite. Potassic alteration is characterized by secondary K-feldspar veins and  
1236 selvages around A-veins. Late unmineralized carbonate veins cut the A veins. (C)  
1237 Amphibole phenocryst altered to secondary biotite, which has then been altered to  
1238 chlorite, reflecting potassic alteration overprinted by chlorite–sericite alteration (plane-  
1239 polarized transmitted light; P2E: sample RC13-30). (D) Plagioclase phenocryst partially  
1240 overprinted by sericite (cross-polarized transmitted light; P2E porphyry: sample RC13-

1  
2  
3  
4 1241 11). (E) B-type quartz veins with centerline pyrite in P2L porphyry (sample RC13-44). (F)  
5  
6 1242 Pyritic D vein in P1 porphyry (sample RC13-40). (G) High-grade ore in sheeted A-type  
7  
8  
9 1243 quartz-chalcopyrite-K-feldspar veins (sample RC13-31 in P2E porphyry). (H) Quartz-  
10  
11 1244 carbonate-pyrite-molybdenite-chalcopyrite vein in P2E porphyry (reflected light; sample  
12  
13 1245 RC13-88). Abbreviations: Amp = amphibole; Bi = biotite; Bn = bornite; Cbn = carbonate;  
14  
15 1246 Chl = chlorite; Cpy = chalcopyrite; Kfs = K-feldspar; Mo = molybdenite; Mt = magnetite;  
16  
17 1247 Pl = plagioclase; Py = pyrite; Qtz = quartz. See Digital Appendix Table A1 for sample  
18  
19 1248 locations.  
20  
21  
22  
23 1249  
24  
25  
26 1250 Fig. 6. Zircon U–Pb Tera-Wasserburg concordia diagrams for (A) P1, (B) P2E, (C) P2L,  
27  
28 1251 and (D) P3 porphyry samples dated by LA-MC-ICP-MS. Uncertainty ellipses and  
29  
30 1252 calculated ages are shown at  $2\sigma$ .  
31  
32  
33 1253  
34  
35  
36 1254 Fig. 7. Weighted mean Re-Os model age of three molybdenite vein samples from the Red  
37  
38 1255 Chris Cu-Au deposit.  
39  
40  
41 1256  
42  
43 1257 Fig. 8. Zr/Ti vs. Nb/Y discrimination diagram (Winchester and Floyd, 1977) for porphyry  
44  
45 1258 and basaltic–andesitic dike samples from Red Chris.  
46  
47  
48 1259  
49  
50  
51 1260 Fig. 9. Selected whole-rock major element variation diagrams for porphyry and basaltic–  
52  
53 1261 andesitic dike samples from Red Chris: (A) K<sub>2</sub>O, (B) Na<sub>2</sub>O, (C) TiO<sub>2</sub>, (D) Al<sub>2</sub>O<sub>3</sub>, (E)  
54  
55 1262 total Fe<sub>2</sub>O<sub>3</sub>, and (F) MgO vs. SiO<sub>2</sub>.  
56  
57  
58 1263  
59  
60  
61  
62  
63  
64  
65

1  
2  
3  
4  
5  
6  
7  
8  
9  
10  
11  
12  
13  
14  
15  
16  
17  
18  
19  
20  
21  
22  
23  
24  
25  
26  
27  
28  
29  
30  
31  
32  
33  
34  
35  
36  
37  
38  
39  
40  
41  
42  
43  
44  
45  
46  
47  
48  
49  
50  
51  
52  
53  
54  
55  
56  
57  
58  
59  
60  
61  
62  
63  
64  
65

1264 Fig. 10. (A) Primitive mantle-normalized trace element, and (B) chondrite-normalized  
1265 rare earth element diagrams for porphyry and basaltic–andesitic dike samples from Red  
1266 Chris. The normalization values for primitive mantle chondrite are from Sun and  
1267 McDonough (1989).

1268  
1269 Fig. 11.  $\epsilon_{Nd}(t)$  vs. initial  $^{87}Sr/^{86}Sr$  ratios for porphyry and basaltic–andesitic dike samples  
1270 from Red Chris, calculated at  $t = 200$  Ma. All the samples fall in the field of Mesozoic  
1271 igneous rocks in the Stikine island arc terrane, clearly different from the Late Cretaceous  
1272 to Eocene plutons in the Northern Coast Plutonic Complex, which were derived from  
1273 evolved crust. The depleted MORB mantle field is from Pilet et al. (2011); the Stikinia  
1274 Mesozoic igneous rock field is from Samson et al. (1989); the Northern Coast Plutonic  
1275 Complex field is from Samson et al. (1991) and Patchett et al. (1998); all data are re-  
1276 calculated at 200 Ma.

1277  
1278 Fig. 12. Histogram and relative probability curve for zircon  $\epsilon_{Hf}(t)$  values from (A) P1, (B)  
1279 P2E, (C) P2L, and (D) P3 porphyry samples.

1280  
1281 Fig. 13. Classification diagram and plots of oxidation state, temperature, pressure, and  
1282 magmatic water content estimated from amphibole compositions from P2E and P2L  
1283 porphyry samples at Red Chris. A.  $C(Al^{VI} + Fe^{3+} + 2Ti^{4+})$  (apfu) vs.  $A(Na^{+} + K^{+})$  (apfu). B.  
1284  $\Delta FMQ$  vs. temperature. C.  $\Delta FMQ$  vs. pressure. D.  $\Delta FMQ$  vs. magmatic water content.  
1285 The classification diagram for calcic amphibole is given by the Excel spreadsheet of

1  
2  
3  
4  
5  
6  
7  
8  
9  
10  
11  
12  
13  
14  
15  
16  
17  
18  
19  
20  
21  
22  
23  
24  
25  
26  
27  
28  
29  
30  
31  
32  
33  
34  
35  
36  
37  
38  
39  
40  
41  
42  
43  
44  
45  
46  
47  
48  
49  
50  
51  
52  
53  
54  
55  
56  
57  
58  
59  
60  
61  
62  
63  
64  
65

1286 Locock (2014), and the superscript C and A represent C and A cations following the  
1287 general amphibole formula ( $AB_2C_5T_8O_{22}W_2$ ), respectively. Note that potassic-magnesian-  
1288 hastingsite is included in the field of magnesio-hastingsite.  $\Delta FMQ$  values, temperatures,  
1289 and magmatic water content were calculated from the spreadsheet of Ridolfi et al. (2010).  
1290 Amphibole crystallization pressures were calculated using the equation of Mutch et al.  
1291 (2016). The  $\Delta FMQ$  values were calculated following the equation of Myers and Eugster  
1292 (1983):  $\log fO_2 = -24,441.9/T (K) + 8.290 (\pm 0.167)$ . Abbreviation: apfu = atoms per  
1293 formula unit.

1294

1295 Fig. 14. Photomicrographs (cross-polarized transmitted light), Backscattered electron  
1296 (BSE) images, and electron microprobe analysis profiles for FeO and anorthite proportion  
1297 ( $X_{An}$ ) for representative plagioclase crystals from the P2E, P2L, and P3 porphyries at Red  
1298 Chris. Red circles on photomicrographs and white circles on BSE images denote the  
1299 analyzed spots. The error bars for  $X_{An}$  and FeO analyses are smaller than the size of the  
1300 symbols. Abbreviations: Amp = amphibole; Ap = apatite; Pl = plagioclase; Ser = sericite.

1301

1302 Fig. 15. Chondrite-normalized REE patterns for zircons from (A) P1, (B), P2E, (C) P2L,  
1303 and (D) P3 porphyry samples from Red Chris. Normalization values are from Sun and  
1304 McDonough (1989).

1305

1306 Fig. 16. Zircon  $Eu_N/Eu_N^*$  vs. temperature diagram.  $Eu_N/Eu_N^*$  is the europium anomaly,  
1307 calculated as  $Eu_N/Eu_N^* = Eu_N/(Sm_N \times Gd_N)^{0.5}$ , using the chondrite normalization values

1  
2  
3  
4  
5  
6  
7  
8  
9  
10  
11  
12  
13  
14  
15  
16  
17  
18  
19  
20  
21  
22  
23  
24  
25  
26  
27  
28  
29  
30  
31  
32  
33  
34  
35  
36  
37  
38  
39  
40  
41  
42  
43  
44  
45  
46  
47  
48  
49  
50  
51  
52  
53  
54  
55  
56  
57  
58  
59  
60  
61  
62  
63  
64  
65

1308 of Sun and McDonough (1989). Oxidized suites have zircon  $Eu_N/Eu_N^*$  values  $>0.4$   
1309 (Dilles et al., 2015).

1310

1311 Fig. 17. Backscattered electron images of apatite crystals in samples from (A) P1 (RC13-  
1312 39), (B) P2E (RC13-107), (C) P2L (RC13-33), and (D) P3 (RC13-78). Concentrations of  
1313  $SO_3$  and Cl in apatite crystals are shown in wt. % ( $SO_3/Cl$ ); red circles represent the  
1314 analyzed spots. Higher concentrations are observed in apatites from P2E and P2L; some  
1315 apatite microphenocrysts from P2 porphyries show zoning from  $SO_3$ -Cl-rich cores to  
1316  $SO_3$ -Cl-poorer rims (C).

1317

1318 Fig. 18. Plots of (A) S, and (B) F vs. Cl contents for apatite microphenocrysts from P1 to  
1319 P3 porphyry samples at Red Chris. Abbreviation: apfu = atoms per formula unit. Data  
1320 from Digital Appendix Table A8.

1  
2  
3  
4 **1 Elevated magmatic sulfur and chlorine contents in ore-forming magmas at the Red**  
5  
6 **2 Chris porphyry Cu-Au deposit, Northern British Columbia, Canada**

7  
8  
9 3 Jing-Jing Zhu<sup>1, 2, 3\*</sup>, Jeremy P. Richards<sup>1, 2</sup>, Chris Rees<sup>4</sup>, Robert Creaser<sup>2</sup>, S. Andrew  
10  
11 DuFrane<sup>2</sup>, Andrew Locock<sup>2</sup>, Joseph A. Petrus<sup>1</sup>, and Jürgen Lang<sup>2</sup>

12  
13  
14 5 <sup>1</sup> *Harquail School of Earth Sciences, Laurentian University, 935 Ramsey Lake Road,*  
15  
16 6 *Sudbury, ON, Canada P3E 2C6*

17  
18  
19 7 <sup>2</sup> *Department of Earth and Atmospheric Sciences, University of Alberta, Edmonton,*  
20  
21 8 *Alberta, Canada T6G 2E3*

22  
23  
24 9 <sup>3</sup> *State Key Laboratory of Ore Deposit Geochemistry, Institute of Geochemistry, Chinese*  
25  
26 10 *Academy of Sciences, Guiyang 550081, PR China*

27  
28  
29 11 <sup>4</sup> *Imperial Metals Corporation, 200-580 Hornby Street, Vancouver, B.C., Canada V6C*  
30  
31 12 *3B6*

32  
33  
34  
35  
36 13 *\*Corresponding author e-mail: [jzhu4@laurentian.ca](mailto:jzhu4@laurentian.ca); [zhujingjing-1103@163.com](mailto:zhujingjing-1103@163.com)*

37  
38  
39  
40 **14 Abstract**

41  
42 15 The Red Chris porphyry Cu-Au deposit is located in the Stikinia island-arc terrane in  
43  
44 16 northwest British Columbia, ~~it~~ It is hosted by the Red Stock, which has four phases of  
45  
46 17 porphyry intrusions: P1, P2E, P2L, and P3. New U-Pb dating of zircon shows that these  
47  
48 18 intrusions were emplaced at  $211.6 \pm 1.3$  Ma (MSWD = 0.85),  $206.0 \pm 1.2$  Ma (MSWD =  
49  
50 19  $1.5$ ),  $203.6 \pm 1.8$  Ma (MSWD = 1.5), and  $201.7 \pm 1.2$  Ma (MSWD = 1.05), respectively.  
51  
52 20 The ore-forming event at Red Chris was a short-lived event at  $206.1 \pm 0.5$  Ma (MSWD =  
53  
54 21  $0.96$ ; weighted average age of three Re-Os analyses), implying a duration of <1 m.y., as  
55  
56 22 defined by the uncertainty range. This mineralization age coincides with the emplacement  
57  
58  
59  
60  
61  
62  
63  
64  
65

1  
2  
3  
4 23 age of the P2E porphyry, and is consistent with cross-cutting relationships that suggest  
5  
6  
7 24 P2E was the main syn-mineralization intrusion.

8  
9 25 Zircons from P1 to P3 porphyry rocks have consistently high  $\text{Eu}_N/\text{Eu}_N^*$  ratios (mostly >  
10  
11 26 0.4), indicating that their associated magmas were moderately oxidized. The magmatic  
12  
13  
14 27 water contents estimated from plagioclase and amphibole compositions suggest  $\text{H}_2\text{O}$   
15  
16 28 contents of ~5 wt. %. Taken together, the P1 to P3 porphyries are interpreted to be  
17  
18  
19 29 moderately oxidized and hydrous.

20  
21 30 The four phases of porphyries are differentiated by sulfur and chlorine contents. The  
22  
23  
24 31  $\text{SO}_3$  contents of igneous apatite microphenocrysts from the mineralization-related P2  
25  
26 32 porphyries are higher (P2E:  $0.30 \pm 0.13$  wt. %,  $n = 34$ ; P2L:  $0.29 \pm 0.18$  wt. %,  $n = 100$ )  
27  
28  
29 33 than those from the pre-mineralization P1 ( $0.11 \pm 0.03$  wt. %,  $n = 34$ ) and post-  
30  
31 34 mineralization P3 porphyries ( $0.03 \pm 0.01$  wt. %,  $n = 13$ ). The chlorine contents in apatite  
32  
33 35 grains from the P2E and P2L porphyries are  $1.18 \pm 0.37$  ( $n = 34$ ) and  $1.47 \pm 0.28$  wt. %  
34  
35 36 ( $n = 100$ ), also higher than those from P1 ( $0.51 \pm 0.3$  wt. % Cl,  $n = 34$ ) and P3 ( $0.02 \pm$   
36  
37 37  $0.02$  wt. % Cl,  $n = 17$ ). These results imply that the sulfur and chlorine contents of the  
38  
39  
40 38 P2E and P2L magmas were higher than in the P1 and P3 magmas, suggesting that  
41  
42  
43 39 elevated magmatic S-Cl contents in the P2 porphyries may have been important for ore-  
44  
45 40 formation. Although the process that caused the increase in sulfur and chlorine is not  
46  
47  
48 41 clear, reverse zoning seen in plagioclase phenocrysts from the P2 porphyry, and the  
49  
50  
51 42 occurrence of more mafic compositions in P2L suggest that recharge of the deeper  
52  
53 43 magma chamber by a relatively S-Cl-rich mafic magma may have triggered the ore-  
54  
55 44 forming hydrothermal event.

56  
57  
58 45



1  
2  
3  
4  
5  
6  
7  
8  
9  
10  
11  
12  
13  
14  
15  
16  
17  
18  
19  
20  
21  
22  
23  
24  
25  
26  
27  
28  
29  
30  
31  
32  
33  
34  
35  
36  
37  
38  
39  
40  
41  
42  
43  
44  
45  
46  
47  
48  
49  
50  
51  
52  
53  
54  
55  
56  
57  
58  
59  
60  
61  
62  
63  
64  
65

## Introduction

46  
47 Compared to the relatively long-lived magmatic systems represented by a composite  
48 batholith (up to 10 m.y.; Matzel et al., 2006; Walker et al., 2007; Harris et al., 2008;  
49 Schaltegger et al., 2009; Paterson et al., 2011; Rezeau et al., 2016), the life spans of  
50 porphyry magmatic-hydrothermal ore-forming events are much shorter, probably on the  
51 order of several ~~10<sup>5</sup>~~-hundred thousand years (up to 1 m.y.; Cathles et al., 1997; Hayba  
52 and Ingebritsen, 1997; Masterman et al., 2004; von Quadt et al., 2011; Weis et al., 2012;  
53 Chiaradia et al., 2013; Correa et al., 2016; Li et al., 2017). In many large magmatic  
54 systems, porphyry formation occurs at a relatively late stage in the system's evolution  
55 (Creasey, 1977; Titley and Beane, 1981; Candela, 1992; Richards, 2003; Rohrlach and  
56 Loucks, 2005; Yang et al., 2009; Correa et al., 2016).

57 Although the multiple phases of porphyry stocks are commonly broadly cogenetic,  
58 they may be derived from packets of magma that evolved at different crustal levels over  
59 the history of the larger magmatic system (Annen et al., 2006). Understanding why ore-  
60 formation is only associated with a specific intrusive suite within these broader systems,  
61 and at discrete, commonly singular times, is a focus of this study.

62 It is recognized that magmas with high sulfur (>1000 ppm), chlorine (>3000 ppm),  
63 and water (>4 wt. %) contents as well as relatively high oxidation states (higher than the  
64 fayalite-magnetite-quartz buffer,  $\Delta\text{FMQ}$ , by 1–2 log  $f\text{O}_2$  units) are fertile for the  
65 generation of magmatic-hydrothermal porphyry Cu deposits (Burnham, 1979; Candela,  
66 1992; Richards, 2003, 2009, 2011, 2015; Wallace, 2005; Chambefort et al., 2008; Simon  
67 and Ripley, 2011; Chiaradia et al., 2012; Loucks, 2014; Hou et al., 2015; Lu et al., 2015,  
68 2016; Chelle-Michou and Chiaradia, 2017). These ingredients are essential for the

1  
2  
3  
4 69 transport of Cu (and Au) both in the magma (Zajacz et al., 2012) and in exsolved high  
5  
6 70 temperature, SO<sub>2</sub>-rich, saline magmatic fluids (Candela and Holland, 1984; Zajacz et al.,  
7  
8  
9 71 2011). However, whereas many magmas achieve such compositions, ore formation is a  
10  
11 72 relatively rare and discrete event in such systems.

13  
14 73 Various mechanisms have been proposed that might trigger an ore forming event  
15  
16 74 from a fertile magma source, including recharge of the magma chamber by hot, sulfur-  
17  
18 75 rich melts (Hattori, 1993; Keith et al., 1997; Larocque et al., 2000; Hattori and Keith,  
19  
20 76 2001; Halter et al., 2005; Stern et al., 2007; Nadeau et al., 2010, 2016; Wilkinson, 2013;  
21  
22 77 Tapster et al., 2016; Zhang and Audétat, 2017), fluxing by sulfur gases (Blundy et al.,  
23  
24 78 2015), or increasing the water and oxidation state of magmas during long-term  
25  
26 79 fractionation in deep magma chambers (Ballard et al., 2002; Wang et al., 2014a, 2014b;  
27  
28 80 Dilles et al., 2015; Lu et al., 2015, 2016). The Red Chris porphyry Cu-Au deposit  
29  
30 81 provides an opportunity to test these hypotheses, because ore-formation occurred at a  
31  
32 82 discrete and relatively late stage in the ~10 m.y. history of the associated magmatic  
33  
34 83 system.

35  
36 84 The Red Chris deposit is located in northwest British Columbia, and contains  
37  
38 85 measured and indicated resources of 1,035 million metric tonnes of ore grading 0.35%  
39  
40 86 Cu and 0.35 g/t Au (Gillstrom et al., 2012). Pre-, syn-, and post-mineralization porphyry  
41  
42 87 intrusions have been recognized based on detailed core logging and petrographic work  
43  
44 88 (Rees et al., 2015), with mineralization occurring in a singular episode during this  
45  
46 89 magmatic history. In this paper, we present detailed geochronological and geochemical  
47  
48 90 data for the porphyry phases at Red Chris, and show that they have similar bulk  
49  
50 91 compositions, including all being relatively hydrous and oxidized. However, the syn-  
51  
52  
53  
54  
55  
56  
57  
58  
59  
60  
61  
62  
63  
64  
65

1  
2  
3  
4 92 mineralization porphyry is characterized by plagioclase with reverse zoning and apatite  
5  
6 93 with relatively high sulfur and chlorine contents. We interpret these data to indicate that  
7  
8  
9 94 high magmatic S and Cl contents, in addition to high H<sub>2</sub>O contents and oxidation state,  
10  
11 95 were critical for Cu-Au ore-formation at Red Chris. We speculate that there was an  
12  
13  
14 96 injection of relatively mafic (hotter, and more S- and Cl-rich) but cogenetic magma into  
15  
16 97 the mid–upper crustal source magma chamber approximately coincident with  
17  
18  
19 98 emplacement of the syn-mineralization porphyry.  
20  
21 99

## 23 100 **Geological Setting**

24  
25  
26  
27 101 Red Chris is situated within the island-arc terrane of Stikinia in the Intermontane Belt  
28  
29 102 of the Canadian Cordillera of British Columbia (Fig. 1; Monger and Irving, 1980; Nelson  
30  
31 and Colpron, 2007; Nelson et al., 2013). Stikinia consists primarily of Mesozoic arc-  
32  
33 103 related igneous and sedimentary rocks, formed in response to subduction processes prior  
34  
35 104 to accretion to the ancestral North American margin in the Middle Jurassic (Gabrielse,  
36  
37 105 1991; Ricketts et al., 1992; Lang et al., 1995; Mihalynuk et al., 2004; Nelson and Colpron,  
38  
39 106 2007; Logan and Mihalynuk, 2014). In northwestern Stikinia, arc assemblages comprise  
40  
41 107 the Middle to Late Triassic Stuhini Group, unconformably overlain by Late Triassic and  
42  
43 108 Early to Middle Jurassic volcanic and sedimentary rocks of the Hazelton Group (Fig. 2;  
44  
45 109 Brown et al., 1991; Gabrielse, 1991; Marsden and Thorkelson, 1992; Dostal et al., 1999;  
46  
47 110 Gagnon et al., 2012; Nelson et al., 2013; Logan and Mihalynuk, 2014). The Hazelton  
48  
49 111 Group is overlain by sedimentary rocks of the syn- to post-accretion Middle Jurassic to  
50  
51 112 Early Cretaceous Bowser Lake Group.  
52  
53  
54  
55  
56  
57  
58  
59  
60  
61  
62  
63  
64  
65

1  
2  
3  
4 114 Several porphyry Cu±Au±Mo deposits occur in the region, hosted by Late Triassic to  
5  
6  
7 115 Early Jurassic arc-related plutons (Fig. 1), including Red Chris which formed in the Late  
8  
9 116 Triassic Red Stock. Collectively, these regional intrusions have ages ranging from ~222  
10  
11 117 Ma to ~180 Ma, recording much of the pre-accretionary history of Stikinia (Lang et al.,  
12  
13 118 1995; McMillan et al., 1995; Scott et al., 2008; Nelson et al., 2013; Logan and Mihalynuk,  
14  
15 119 2014). A significant percentage of the known porphyry Cu deposits, including Red Chris,  
16  
17 120 formed during a 6-m.y. pulse of magmatism between 206 and 200 Ma, with compositions  
18  
19 121 ranging from calc-alkaline to strongly alkaline (Lang et al., 1995; McMillan et al., 1995;  
20  
21 122 Nelson et al., 2013; Bissig and Cooke, 2014; Logan and Mihalynuk, 2014; Micko et al.,  
22  
23 123 2014; Pass et al., 2014).  
24  
25  
26  
27  
28  
29  
30 124  
31  
32

### 125 **Geology of the Red Chris Cu-Au deposit**

33  
34  
35  
36 126 The Red Chris Cu-Au deposit was discovered in the 1950s and explored  
37  
38 127 intermittently in subsequent decades, with mining beginning in 2015 (Ash et al., 1995,  
39  
40 128 1996; Newell and Peatfield, 1995; Baker et al., 1997; Gillstrom et al., 2012; Rees et al.,  
41  
42 129 2015). The deposit is hosted by the Red Stock, which is the largest of a suite of Late  
43  
44 130 Triassic to Early Jurassic stocks and dikes that intrude the Stuhini Group in the district  
45  
46 131 (Fig. 2; Friedman and Ash, 1997; Rees et al., 2015). The stock is tabular, elongate in an  
47  
48 132 east to northeast direction, and approximately 6.5 km long by 300 to 1500 m wide (Fig. 2;  
49  
50 133 Ash et al., 1995; Baker et al., 1997; Gillstrom et al., 2012). It has a steep northern contact  
51  
52 134 against Stuhini Group country rocks, but its southeastern margin against Hazelton and  
53  
54 135 Bowser Lake Group strata is poorly exposed, and has locally been truncated by the NE-  
55  
56  
57  
58  
59  
60  
61  
62  
63  
64  
65

1  
2  
3  
4 136 trending, steeply SE-dipping South Boundary fault (Fig. 2). This fault, and the East zone  
5  
6 137 fault within the stock, probably reflect a long-lived and deep structure which guided the  
7  
8  
9 138 emplacement of the intrusions, mineralization, and subsequent deformation of the Red  
10  
11 139 Stock.

14  
15 140 The Red Stock is a composite intrusion consisting of several phases of porphyritic  
16  
17 141 diorite to quartz monzonite. Mineralogically, the rocks consist of medium- to coarse-  
18  
19 142 grained amphibole, plagioclase, and minor biotite phenocrysts, with K-feldspar,  
20  
21  
22 143 plagioclase, and quartz in the groundmass. Based on compositional and textural  
23  
24 144 differences and crosscutting relationships, Rees et al. (2015) identified four distinct  
25  
26 145 porphyry phases, P1, P2, P3, and P4. The P1 porphyry is a pre-mineralization  
27  
28 146 leucodiorite which accounts for the main volume of the Red Stock, and is distinguished  
29  
30 147 by sparse anhedral to subhedral amphibole (~10%) and abundant plagioclase (30–40  
31  
32 148 vol. %) phenocrysts with lengths up to 4 mm. The groundmass is composed of fine-  
33  
34  
35 149 grained plagioclase and minor quartz (Fig. 3A).

36  
37  
38  
39  
40 150 The P2 porphyry is a syn-mineralization quartz monzonite intrusion which is largely  
41  
42 151 unexposed at surface but is observed in drill core to have intruded P1 at depth. It has been  
43  
44 152 subdivided by Rees et al. (2015) into early (P2E), intermediate (P2I), and late (P2L)  
45  
46 153 phases based on vein truncations and chilled margins. The P2 porphyries are generally  
47  
48 154 characterized by tabular subhedral to euhedral amphibole (10–15 vol. %) and plagioclase  
49  
50 155 (35–50 vol. %) phenocrysts. The amphibole crystals are mostly euhedral and larger than  
51  
52 156 in P1, with lengths up to 10 mm. The groundmass comprises K-feldspar, plagioclase, and  
53  
54  
55 157 quartz. In this paper, the P2 subphases are simplified to an early stage (P2E; Fig. 3B) and  
56  
57 158 late stage porphyry (P2L, probably corresponding to P2I and P2L of Rees et al., 2015;  
58  
59  
60  
61  
62  
63  
64  
65

1  
2  
3  
4 159 Fig. 3C). The P2E porphyry has a crowded plagioclase texture with slightly smaller  
5  
6 160 amphibole phenocrysts than P2L. In contrast, the P2L porphyry is relatively fresh and  
7  
8  
9 161 occurs only as small dikes (Fig. 4).

10  
11  
12 162 The post-mineralization P3 monzonite porphyry is much less abundant. It is texturally  
13  
14  
15 163 similar to the P2L porphyry with abundant amphibole phenocrysts (15–20 vol. %), but is  
16  
17 164 distinguished by the absence of quartz in the groundmass, which is mainly composed of  
18  
19  
20 165 K-feldspar and plagioclase (Fig. 3D). Although no crosscutting relationships between the  
21  
22 166 P3 and P2L porphyries have been found, the zircon U-Pb dating results (see below)  
23  
24 167 confirm that P3 is younger. The P4 porphyry occurs as rare dikes and is typified by  
25  
26  
27 168 sparse fine-grained amphibole phenocrysts (Rees et al., 2015). No P4 samples were  
28  
29  
30 169 included in this study.

31  
32  
33 170 Several younger basaltic to andesitic dikes with sparse amphibole phenocrysts cut the  
34  
35 171 Red Stock and the Stuhini Group host rocks (Figs. 3E and F). They postdate the  
36  
37 172 porphyry-stage Cu-Au mineralization (Baker et al., 1997; Rees et al., 2015), but are  
38  
39  
40 173 mildly to strongly altered (Figs. 3E and F) and are crosscut by late quartz-calcite-pyrite  
41  
42  
43 174 veins.

#### 44 45 175 *Hydrothermal alteration*

46  
47  
48  
49 176 Alteration at Red Chris has been described previously by Baker et al. (1997),  
50  
51 177 Gillstrom et al. (2012), Norris (2012) and Rees et al. (2015). The alteration assemblages  
52  
53 178 are typical of calc-alkaline porphyry Cu systems (Lowell and Guilbert, 1970; Seedorff et  
54  
55  
56 179 al., 2005; Sillitoe, 2010), and consists of early stage potassic alteration, overprinted by  
57  
58  
59 180 chlorite-sericite, sericitic (phyllic), intermediate argillic, and minor late stage propylitic

1  
2  
3  
4 181 ~~alteration (see paragenetic diagram in Rees et al., 2015)~~Alteration at Red Chris is typical  
5  
6 182 ~~of calc-alkaline porphyry Cu systems (Lowell and Guilbert, 1970; Seedorff et al., 2005;~~  
7  
8 183 ~~Sillitoe, 2010), and consists of early stage potassic alteration, overprinted by chlorite–~~  
9  
10 184 ~~sericite, sericitic (phyllic), intermediate argillic, and minor late stage propylitic alteration~~  
11  
12 185 ~~(see paragenetic diagram in figure 13 of Rees et al., 2015; Baker et al., 1997; Gillstrom et~~  
13  
14 186 ~~al., 2012; Norris, 2012).~~ Potassic alteration is expressed by replacement of amphibole  
15  
16 187 phenocrysts by secondary biotite, plagioclase replaced or rimmed by secondary K-  
17  
18 188 feldspar, and by K-feldspar veins (Figs. 3B and 5A–C). It is best preserved in the deeper  
19  
20 189 levels of the deposit where it is spatially associated with the syn-mineralization P2E  
21  
22 190 porphyry; however it locally extends into pre-mineralization P1 porphyry wall rocks (Fig.  
23  
24 191 4). The P2L and P3 porphyries ~~are~~were only weakly affected by potassic alteration (Rees  
25  
26 192 et al., 2015).

27  
28  
29  
30  
31  
32  
33  
34 193 Chlorite–sericite alteration is characterized by chlorite replacing secondary biotite  
35  
36 194 (Fig. 5C) and sericite replacing feldspar (Fig. 5D). At shallower levels in the system,  
37  
38 195 potassic alteration is completely overprinted by phyllic and intermediate argillic  
39  
40 196 alteration (Gillstrom et al., 2012), characterized by sericite after plagioclase (phyllic; Fig.  
41  
42 197 5D), and illite and kaolinite (intermediate argillic; Norris, 2012). This lower temperature  
43  
44 198 alteration overprint affects all the porphyry phases, but is less pervasive at depth.

45  
46  
47  
48  
49 199 Propylitic alteration at Red Chris is mainly observed as minor chlorite and epidote in  
50  
51 200 the outer part of the Red Stock, and extends for 100 to 200 m into the Stuhini volcanic  
52  
53 201 country rocks (Gillstrom et al., 2012; Norris, 2012; Rees et al., 2015).

54  
55  
56  
57  
58 202 *Vein styles and mineralization*

1  
2  
3  
4 203 Detailed descriptions of vein styles at Red Chris have been given by Norris (2012)  
5  
6 204 and Rees et al. (2015). A-type quartz veins (Gustafson and Hunt, 1975) and stockworks  
7  
8  
9 205 are associated with potassic alteration and host the bulk of the copper-gold mineralization.  
10  
11 206 These veins are most intensely developed around the apex of the principal P2 porphyry  
12  
13  
14 207 body, but extend for hundreds of metres into the P1 wall rocks (~~see figure 13 in Rees et~~  
15  
16 208 ~~al., 2015~~). Typical A veins contain K-feldspar, biotite, chalcopyrite, bornite, and  
17  
18  
19 209 magnetite, with K-feldspar alteration halos (Figs. 5A–B and G). Copper sulfides also  
20  
21 210 occur as disseminations in the host porphyry. Bornite is more abundant in the apex of  
22  
23 211 P2E, and progressively decreases outwards where chalcopyrite is the dominant Cu-  
24  
25 212 sulfide (Norris, 2012; Rees et al., 2015). At shallower depths in the preserved system,  
26  
27 213 early bornite was sulfidized to chalcopyrite, and pyrite becomes increasingly dominant.  
28  
29 214 Rees et al. (2015) delineated a high-sulfur contour (>4% S) in section above which total  
30  
31 215 sulfide (dominantly pyrite) ranges from 4 to 10%. Microscopic native gold and electrum  
32  
33 216 occur as inclusions in bornite (Rees et al., 2015). The grades of Cu and Au are positively  
34  
35 217 correlated with quartz vein density (Gillstrom et al., 2012). In high-grade zones at depth  
36  
37 218 (e.g., 4.12 % Cu and 8.83 g/t Au in hole 09-350 from 540 to 692.5 m down-hole depth),  
38  
39 219 vein abundance exceeds 80 vol. % in sheeted arrays (Fig. 5G; Rees et al., 2015).  
40  
41  
42  
43  
44  
45

46 220 B- and D-type veins (Gustafson and Hunt, 1975) are relatively minor at Red Chris,  
47  
48 221 and host only minor amounts of Cu sulfides. B quartz veins are characterized by  
49  
50 222 relatively straight margins with sulfide centerlines (pyrite and minor chalcopyrite, and  
51  
52 223 locally molybdenite; Fig. 5E). Pyritic D veins have variable widths (1 to 10 mm; Fig. 5F).  
53  
54 224 Carbonate and minor chlorite veins cut all the earlier veins and are generally barren  
55  
56 225 (Norris, 2012).  
57  
58  
59  
60  
61  
62  
63  
64  
65



1  
2  
3  
4 **226** **Sampling and Analytical Methods**

5  
6 **227** Samples of the P1, P2E, P2L, and P3 porphyries were collected from drill core, and  
7  
8  
9 **228** descriptions and locations are listed in Digital Appendix Table A1; sampled drill hole  
10  
11 **229** locations are also shown on Figure 2. Fourteen least-altered samples of the porphyry  
12  
13  
14 **230** intrusions and three samples of late basaltic to andesitic dikes were selected for whole-  
15  
16 **231** rock geochemical analysis. Eight of these samples were selected for determination of Nd-  
17  
18 **232** Sr isotopes. Three samples of quartz-carbonate-pyrite-molybdenite-chalcopyrite veins  
19  
20 **233** (Fig. 5H) were collected for Re-Os dating. Four samples of the P1 (RC13-40), P2E  
21  
22 **234** (RC13-107), P2L (RC13-33), and P3 (RC13-78) intrusions were selected for zircon U-Pb  
23  
24  
25 **235** dating, Hf isotopic, and trace element analyses. Details of analytical methods are  
26  
27  
28 **236** provided in Appendix 1.

29  
30 **237**  
31  
32  
33 **238** *Electron microprobe analyses*

34  
35  
36 **239** Primary igneous minerals such as plagioclase and amphibole in the porphyry rocks  
37  
38 **240** are widely altered to K-feldspar, sericite, and chlorite (Figs. 3A–B and 5C–D). However,  
39  
40 **241** a few least-altered samples of the P2E, P2L, and P3 porphyries contained unaltered  
41  
42 **242** plagioclase and amphibole grains. In addition, igneous apatite grains were typically  
43  
44 **243** preserved as inclusions within plagioclase and amphibole phenocrysts. Compared with  
45  
46 **244** hydrothermal apatite (acicular crystals intergrown with other hydrothermal minerals such  
47  
48 **245** as quartz, sericite, chlorite, and sulfides), igneous apatite grains typically showed stubby  
49  
50 **246** prismatic habits, as described by Richards et al. (2017). Detailed analytical methods are  
51  
52  
53 **247** described in Appendix 1.

54  
55  
56  
57  
58 **248**  
59  
60  
61  
62  
63  
64  
65

1  
2  
3  
4 249 *Re-Os molybdenite dating*

5  
6 250 Three samples of molybdenite from quartz-carbonate-pyrite-molybdenite-chalcopyrite  
7  
8 251 veins were collected from the Gully zone (RC13-88 and RC13-103), and the East zone  
9  
10 252 (RC13-82; Digital Appendix Table A1; Fig. 2). A molybdenite mineral separate was  
11  
12 253 produced for each sample by metal-free crushing followed by gravity and magnetic  
13  
14 254 concentration methods. Dating was conducted at the Canadian Centre for Isotopic  
15  
16 255 Microanalysis at the University of Alberta, Canada, using methods described in  
17  
18 256 Appendix 1.  
19  
20  
21  
22  
23

24 257

25  
26 258 **Geochronological Results**

27  
28 259 *Zircon U-Pb ages of the Red Stock*

29  
30 260 Zircon U-Pb results are presented in Digital Appendix Table A2 and illustrated in  
31  
32 261 Figure 6; all ages are illustrated and reported with  $2\sigma$  errors. All the zircons show  
33  
34 262 oscillatory zoning under BSE imaging. Sample RC13-40 was collected from P1  
35  
36 263 leucodiorite porphyry (Digital Appendix Table A1). Analyzed zircon grains form a  
37  
38 264 tightly clustered age population, mostly with low common lead contents. Except for one  
39  
40 265 inherited or xenocryst zircon (apparent  $^{206}\text{Pb}/^{238}\text{U}$  age =  $261 \pm 12$  Ma), the twenty-seven  
41  
42 266 grains yielded an intercept age of  $211.6 \pm 1.3$  Ma (MSWD = 0.85; Fig. 6A), similar to the  
43  
44 267 weighted mean  $^{206}\text{Pb}/^{238}\text{U}$  age of  $211.8 \pm 1.3$  Ma (MSWD = 0.8).  
45  
46  
47

48  
49 268 Sample RC13-107 was collected from P2E quartz monzonite porphyry (Digital  
50  
51 269 Appendix Table A1). One xenocrystic zircon grain yielded an older age (apparent  
52  
53 270  $^{206}\text{Pb}/^{238}\text{U}$  age =  $316 \pm 10$  Ma), but the other twenty-nine zircons contained low amounts  
54  
55 271 of common lead and intersected the concordia line at  $206.0 \pm 1.2$  Ma (MSWD = 1.5; Fig.  
56  
57  
58  
59  
60  
61  
62  
63  
64  
65

1  
2  
3  
4 272 6B), in good agreement with the weighted mean  $^{206}\text{Pb}/^{238}\text{U}$  age of  $205.9 \pm 1.5$  Ma  
5  
6 273 (MSWD = 1.5).

7  
8  
9 274 Sample RC13-33 was collected from P2L quartz monzonite porphyry (Digital  
10  
11 275 Appendix Table A1). Two xenocryst grains were found among thirty-one analyzed  
12  
13 276 zircons, with  $^{206}\text{Pb}/^{238}\text{U}$  ages of  $298 \pm 16$  Ma and  $441 \pm 13$  Ma. The remaining twenty-  
14  
15 277 nine zircon grains had low common lead contents and yielded an intercept age of  $203.6 \pm$   
16  
17 278  $1.8$  Ma (MSWD = 1.5; Fig. 6C), similar to the weighted mean  $^{206}\text{Pb}/^{238}\text{U}$  age of  $203.3 \pm$   
18  
19 279  $1.5$  Ma (MSWD = 1.04).

20  
21  
22  
23 280 Sample RC13-78 was collected from P3 monzonite porphyry (Digital Appendix Table  
24  
25 281 A1). Thirty-two zircons with low common lead contents yielded an intercept age of  $201.7$   
26  
27 282  $\pm 1.2$  Ma (MSWD = 1.05; Fig. 6D), and a weighted mean  $^{206}\text{Pb}/^{238}\text{U}$  age of  $201.6 \pm 1.2$   
28  
29 283 Ma (MSWD = 1.04).

30  
31  
32  
33 284 All of the zircons have magmatic textures, and the intercept ages above are interpreted  
34  
35 285 to be the crystallization ages of the individual intrusions. The ages are consistent with  
36  
37 286 crosscutting relationships described by Rees et al. (2015), and define a 10 m.y. span of  
38  
39 287 magmatism from  $211.6 \pm 1.3$  Ma (P1) to  $201.7 \pm 1.2$  Ma (P3). The relative ages of the  
40  
41 288 two samples of syn-mineralization P2 porphyry are consistent with crosscutting  
42  
43 289 relationships, but the dates (P2E:  $206.0 \pm 1.2$  Ma; P2L:  $203.6 \pm 1.8$  Ma) overlap within  
44  
45 290 the  $2\sigma$  uncertainty. Hence the apparent 2.4 m.y. age difference is not statistically robust,  
46  
47 291 and their true ages may in fact be closer as suggested by their close relationship with ore  
48  
49 292 mineral paragenesis.

50  
51  
52  
53 293

54  
55  
56  
57 294 *Re-Os molybdenite ages*

1  
2  
3  
4 295 The Re-Os model ages for three samples are shown in Table 1. They have relatively  
5  
6 296 high rhenium contents ranging from 497.8 to 1771 ppm, with common  $^{187}\text{Os}$  of 1078 to  
7  
8  
9 297 3821 ppb. Although the three samples are from two different mineralization zones (i.e.,  
10  
11 298 East and Gully zones; Fig. 2), they yielded indistinguishable model ages within  
12  
13  
14 299 uncertainty:  $206.5 \pm 0.8$  Ma,  $205.7 \pm 0.9$  Ma, and  $205.9 \pm 1.1$  Ma ( $\pm 2$  s.d.). The small  
15  
16 300 grain size of the molybdenite ( $< 1$  mm) minimizes the risk of decoupling between Re and  
17  
18  
19 301  $^{187}\text{Os}$  in these samples (caused by diffusion: Selby and Creaser, 2004). The results  
20  
21 302 yielded a weighted average age for all three samples of  $206.1 \pm 0.5$  Ma (95% confidence  
22  
23  
24 303 level with MSWD = 0.96; Fig. 7). This age is consistent with the age of the syn-  
25  
26 304 mineralization P2E porphyry ( $206.0 \pm 1.2$  Ma).  
27  
28  
29  
30

## 31 306 **Geochemical and Isotopic Results**

### 32 33 307 *Whole-rock major and trace elements*

34  
35  
36 308 Whole-rock major and trace element compositions for fourteen samples of the Red  
37  
38 309 Stock and three basaltic–andesitic dike samples are listed in Table 2. All the P1 to P3  
39  
40  
41 310 porphyry intrusions have relatively homogeneous major element compositions, but have  
42  
43 311 moderate to high loss-on-ignition values (LOI: 2.3 to 10.9%) reflecting varying degrees  
44  
45  
46 312 of potassic and sericitic alteration. On an LOI-free basis, they are mostly intermediate  
47  
48 313 composition ( $\text{SiO}_2 = 56.71\text{--}63.16$  wt. %; Digital Appendix Table A3), and straddle the  
49  
50  
51 314 boundary between granodiorite (diorite) and syenite on a Zr/Ti versus Nb/Y diagram (Fig.  
52  
53 315 8). The late basaltic–andesitic dikes have distinct compositions, and plot in the field of  
54  
55  
56 316 diorite and gabbro on Figure 8. On Harker-type diagrams of  $\text{SiO}_2$  versus selected major  
57  
58 317 elements, the alkali elements ( $\text{K}_2\text{O}$  and  $\text{Na}_2\text{O}$ ; Figs. 9A–B) show significant scatter,  
59  
60  
61  
62  
63  
64  
65

1  
2  
3  
4 318 likely due to hydrothermal alteration, as confirmed by a rough correlation between alkali  
5  
6 319 contents and LOI. However, other elements such as Fe<sub>2</sub>O<sub>3</sub>, MgO, TiO<sub>2</sub>, and Al<sub>2</sub>O<sub>3</sub> show  
7  
8  
9 320 roughly correlated trends with SiO<sub>2</sub> (Figs. 9E–F), suggesting a broadly cogenetic suite,  
10  
11 321 with the exception of the late basaltic to andesitic dikes, which do not plot on the same  
12  
13  
14 322 trends for K<sub>2</sub>O and TiO<sub>2</sub>.

15  
16 323 On primitive mantle-normalized extended trace element and chondrite-normalized  
17  
18 324 rare earth element (REE) diagrams (Figs. 10A–B), the porphyritic rocks show largely  
19  
20  
21 325 indistinguishable patterns consistent with typical subduction-related igneous rocks  
22  
23  
24 326 (Hawkesworth et al., 1993; Pearce, 1996), characterized by large-ion lithophile element  
25  
26 327 (LILEs: Rb, Ba, Th, U, K) and light rare earth element enrichments (LREE), low  
27  
28 328 concentrations of high field strength elements (HFSE: Nb, Ta, Zr, Hf, and Ti), relative  
29  
30  
31 329 depletions in compatible elements and middle to heavy rare earth elements (MREE,  
32  
33 330 HREE; La/Yb =  $8.9 \pm 1.7$ , n = 14), and flat to listric-shaped patterns from MREE to  
34  
35  
36 331 HREE. Such listric patterns likely reflect amphibole fractionation from hydrous magmas,  
37  
38 332 and are an indication of magma fertility for porphyry ore formation (Richards and  
39  
40  
41 333 Kerrich, 2007). Most samples have flat or slightly positive Eu anomalies with  $Eu_N/Eu_N^*$   
42  
43 334 of  $1.1 \pm 0.15$  (n = 14; Fig. 10B), also likely reflecting amphibole fractionation and lack of  
44  
45  
46 335 plagioclase fractionation.

47  
48 336 Three samples of late basaltic to andesitic dikes show distinct trace element patterns,  
49  
50  
51 337 especially for HFSE and REE, which are enriched relative to the porphyries; they are  
52  
53 338 clearly not cogenetic with the earlier porphyries.

54  
55 339 Excluding two samples with high Sr values that may reflect calcite veining, the  
56  
57  
58 340 porphyries have relatively high Sr/Y ( $53 \pm 23$ , n = 12) and V/Sc ratios ( $9.0 \pm 0.9$ , n = 14),  
59  
60  
61  
62  
63  
64  
65

1  
2  
3  
4 341 which overlap the range of fertile rocks for porphyry formation (Richards and Kerrich,  
5  
6 342 2007; Loucks, 2013, 2014).

7  
8  
9 343

10  
11 344 *Whole-rock Nd-Sr isotopes*

12  
13  
14 345 Nd and Sr isotopic compositions of the porphyritic rocks are very homogeneous (Table  
15  
16 346 4 and Fig. 11). They show a narrow range of initial Sr isotopic ratios from 0.7042 to  
17  
18 347 0.7047 ( $(^{87}\text{Sr}/^{86}\text{Sr})_t = 0.7044 \pm 0.0002$ ,  $n = 8$ ), with relatively high  $\epsilon_{\text{Nd}}(t)$  values from 2.4  
19  
20  
21 348 to 3.6 (average =  $+3.1 \pm 0.4$ ,  $n = 8$ ), consistent with a mantle source with minor crustal  
22  
23 349 contamination. The single-stage Nd model ages ( $T_{\text{DM1}}$ ) calculated following the methods  
24  
25 350 of Goldstein et al. (1984) range from 0.74 to 0.88 Ga (average =  $0.80 \pm 0.05$  Ga,  $n = 8$ ),  
26  
27  
28 351 and are indistinguishable for the different porphyry phases. Two basaltic–andesitic dike  
29  
30 352 samples show slightly lower Sr isotopic ratios ( $(^{87}\text{Sr}/^{86}\text{Sr})_t = 0.7042$  and  $0.7043$ ) and  
31  
32  
33 353 higher  $\epsilon_{\text{Nd}}(t)$  ratios ( $+3.5$  and  $+3.9$ ) than the porphyry rocks (Fig. 11).

34  
35  
36  
37 354 *Zircon Hf isotopes*

38  
39 355 Zircon Hf isotopic results are listed in Digital Appendix Table A4, and illustrated in  
40  
41 356 Figure 12. The four zircon samples from porphyritic rocks show indistinguishable Hf  
42  
43 357 isotopic compositions and single-stage Hf model ages of  $375 \pm 52$  Ma (range = 264–527  
44  
45 358 Ma,  $n = 56$ ), with relatively high  $\epsilon_{\text{Hf}}(t)$  values of  $12.0 \pm 0.4$  (weighted mean value, 95%  
46  
47 359 confidence level; range = 8.1–14.8,  $n = 56$ ). These data suggest that the porphyries shared  
48  
49  
50 360 a common primitive mantle source, consistent with their island arc origin.

51  
52  
53  
54 361

55  
56 362 **Amphibole, Plagioclase, Zircon, and Apatite Compositions**

1  
2  
3  
4 363 The compositions of amphibole, plagioclase, zircon, and apatite from samples of least-  
5  
6 364 altered porphyritic rocks are listed in Digital Appendix Tables A5, A6, A7, and A8,  
7  
8  
9 365 respectively. Based on these analyses, water and sulfur contents as well as oxygen  
10  
11 366 fugacity of the magma have been estimated qualitatively and quantitatively.  
12  
13

14 367

15  
16 368 *Amphibole compositions*  
17

18  
19 369 Amphibole compositions can be used to estimate magmatic oxidation state,  
20  
21 370 crystallization temperatures and pressures, as well as water contents (e.g., Ridolfi et al.,  
22  
23 371 2010; Zhang et al., 2012; Wang et al., 2014b). However, fresh amphibole grains were  
24  
25 372 only observed in the P2E and P2L porphyries. All of the analyzed grains are calcic  
26  
27 373 amphiboles, and two generations of amphibole were recognized in both P2E and P2L.  
28  
29 374 Early stage grains occur as phenocrysts and are characterized by higher Al contents  
30  
31 375 (range = 9.35–12.86 and 8.79–13.46 wt. % Al<sub>2</sub>O<sub>3</sub> for P2E and P2L, respectively; Digital  
32  
33 376 Appendix Table A5); they are mostly classified as magnesio-ferri-hornblende and  
34  
35 377 magnesio-hastingsite (including potassic-magnesio-hastingsite; Fig. 13A). The late stage  
36  
37 378 grains were developed in the groundmass or as recrystallized phenocrysts, typified by  
38  
39 379 lower Al concentrations (range = 1.62–4.76 and 4.33–7.53 wt. % Al<sub>2</sub>O<sub>3</sub> for P2E and P2L,  
40  
41 380 respectively; Digital Appendix Table A5). They are classified as magnesio-ferri-  
42  
43 381 hornblende or rare actinolite (Fig. 13A). The early stage amphibole grains are intergrown  
44  
45 382 with plagioclase phenocrysts (Fig. 14), and igneous apatite crystals occur as inclusions  
46  
47 383 within amphibole (Fig. 14B). This indicates that these three minerals are broadly coeval.  
48  
49

50  
51 384 The crystallization temperature, magmatic water contents, and oxygen fugacities were  
52  
53 385 estimated for the two stages of amphiboles using the spreadsheet of Ridolfi et al. (2010),  
54  
55  
56  
57  
58  
59  
60  
61  
62  
63  
64  
65

1  
2  
3  
4 386 and the crystallization pressures were calculated following the equation of Mutch et al.  
5  
6 387 (2016). The Al-in-hornblende geobarometer used is applicable to granitoids that contain  
7  
8 388 amphibole, plagioclase, quartz, and alkali feldspar, broadly consistent with the mineral  
9  
10 389 assemblage within P2 porphyry rocks. The calculated results are listed in Digital  
11  
12  
13  
14 390 Appendix Table A5 and illustrated in Figure 13 (B–C).

15  
16 391 Amphibole phenocrysts from the P2E and P2L porphyry samples have similar  
17  
18 392 compositions, with calculated crystallization pressures from 3.5 to 6.7 kbar (average =  
19  
20  
21 393  $4.6 \pm 0.8$  kbar,  $n = 51$ ), temperatures from 855 to 983 °C (average =  $900 \pm 30$  °C,  $n = 51$ ),  
22  
23 394  $\Delta$ FMQ values from 0.5 to 1.8 (average =  $1.1 \pm 0.3$ ,  $n = 51$ ), and H<sub>2</sub>O contents in melts  
24  
25  
26 395 from 4.0 to 6.1 wt. % (average =  $5.1 \pm 0.4$  wt. %,  $n = 51$ ).

27  
28 396 Late stage (low-Al) amphiboles in P2E porphyry samples yielded crystallization  
29  
30 397 pressures from 0.6 to 1.4 kbar (average =  $1.1 \pm 0.3$  kbar,  $n = 12$ ), temperatures from 637°  
31  
32  
33 398 to 774 °C (average =  $719 \pm 34$  °C,  $n = 12$ ),  $\Delta$ FMQ values from 2.6 to 3.3 (average =  $3 \pm$   
34  
35 399  $0.2$ ,  $n = 12$ ), and magmatic water contents from 3.6 to 5.1 wt. % (average =  $4 \pm 0.4$  wt. %,  $n$   
36  
37 400 = 12). Low-Al amphibole grains from P2L samples yielded slightly higher crystallization  
38  
39 401 pressures ( $2.0 \pm 0.4$  MPa; range = 1.3–2.6 kbar,  $n = 8$ ) and temperatures ( $800 \pm 24$  °C;  
40  
41 402 range = 751–800 °C,  $n = 8$ ), slightly lower  $\Delta$ FMQ values ( $2.4 \pm 0.3$ ; range = 1.1–2.9,  $n =$   
42  
43 403 8), but similar H<sub>2</sub>O contents ( $4.0 \pm 0.2$ ; range = 3.7–4.4,  $n = 8$ ) to those calculated for  
44  
45  
46 404 P2E.

47  
48  
49  
50 405 There are clear trends of increasing oxidation state and decreasing crystallization  
51  
52 406 pressures, temperatures, and magmatic water contents from early to late stage amphiboles  
53  
54  
55 407 in both P2E and P2L porphyries (Figs. 13B–D). These trends are consistent with the  
56  
57  
58 408 high-Al amphibole phenocrysts having crystallized at depth before final crystallization of  
59  
60  
61  
62  
63  
64  
65



1  
2  
3  
4 409 the magma (and low-Al amphibole) after emplacement at shallow levels (e.g., Rutherford  
5  
6 410 and Devine, 2003). The decreasing magmatic water contents might be attributed to  
7  
8  
9 411 degassing during ascent and crystallization, which can also result in a small increase in  
10  
11 412 oxygen fugacity (Mathez, 1984; Candela, 1986; Burgisser and Scaillet, 2007; Zimmer et  
12  
13 413 al., 2010; Bell and Simon, 2011; Dilles et al., 2015).

14  
15  
16 414

17  
18  
19 415 *Plagioclase compositions*

20  
21 416 Plagioclase phenocrysts from all P1 porphyry samples studied have been altered, but  
22  
23 417 partially unaltered phenocrysts were found in some P2 and P3 porphyry samples.

24  
25 418 Analyses with  $K_2O > 1$  wt. % are interpreted to reflect potassic alteration and have been  
26  
27 419 excluded. Plagioclase grains from the P2E porphyry (sample RC13-13) are classified as  
28  
29 420 oligoclase ( $\geq An_{17}$ ) to labradorite ( $\leq An_{70}$ ), with an average anorthite (An) content of  $44 \pm$   
30  
31 421  $12$  mol % ( $n = 28$ ). Nearly all these crystals exhibited reverse zoning in An content, with  
32  
33 422 compositional ranges up to  $\sim 16$  mol %, and FeO contents that correlate positively with  
34  
35 423  $X_{An}$  values (Digital Appendix Table A6; Fig. 14A). Plagioclase grains from the P2L  
36  
37 424 porphyry (samples RC13-26 and RC13-33) have compositions similar to P2E (An mol %  
38  
39 425 =  $48 \pm 5$ ,  $n = 38$ ), and also show reverse zoning with amplitudes up to  $\sim 19$  mol % An that  
40  
41 426 correlate with FeO contents (Fig. 14B). Such reverse zoning with positive An-FeO  
42  
43 427 correlations were observed both in partially altered (i.e., sericite alteration; Fig. 14A) and  
44  
45 428 relatively fresh plagioclase crystals (Fig. 14B), indicating that it was not likely to have  
46  
47 429 been generated by hydrothermal alterations. In contrast, plagioclase grains from the P3  
48  
49 430 porphyry (RC13-78) display relatively uniform An compositions (An mol % =  $51 \pm 5$ ,  $n$   
50  
51 431 = 37), with no clear zoning in  $X_{An}$  and FeO (Fig. 14C).

1  
2  
3  
4 432 Plagioclase compositions (An proportions) are very sensitive to dissolved water  
5  
6 433 content and temperature of the melt, and thus can be used as a hygrometer if corrected for  
7  
8  
9 434 temperature (Mathez, 1973; Lange, 2009; Waters and Lange, 2015). We used apatite  
10  
11 435 saturation temperatures (AST) following the formula of Piccoli and Candela (1994) to  
12  
13 436 calculate magma temperatures for P2 and P3 samples (Table 4; Digital Appendix Table  
14  
15  
16 437 A3). The whole-rock  $\text{SiO}_2$  and  $\text{P}_2\text{O}_5$  values were assumed to approximate the melt  
17  
18 438 contents at the time of crystallization, although this assumption can be challenged  
19  
20  
21 439 (Piccoli and Candela, 1994, 2002). Nevertheless, the calculated temperatures are  
22  
23 440 reasonable for magmas of intermediate, hydrous composition, and are also in agreement  
24  
25 441 with the estimated crystallization temperatures of early stage amphibole (Digital  
26  
27  
28 442 Appendix Table A5): 932 °C for P2E (RC13-13), 892 °C (RC13-26) and 905 °C (RC13-  
29  
30 443 33) for P2L, and 928 °C for P3 (RC13-78; Table 4).

31  
32  
33 444 The updated spreadsheet of Waters and Lange (2015) has been used to calculate  
34  
35 445 magmatic water contents (Digital Appendix Table A9). The calculated values are  
36  
37 446 relatively uniform and indistinguishable between the different porphyry phases:  $5.2 \pm 0.2$   
38  
39 447 ( $n = 28$ ) for P2E,  $5.5 \pm 0.2$  ( $n = 38$ ) for P2L, and  $5.1 \pm 0.1$  wt. % ( $n = 37$ ) for P3. For the  
40  
41 448 P2E and P2L porphyries, the magmatic water contents calculated from plagioclase and  
42  
43 449 early stage amphibole compositions agree well with each other (Digital Appendix Tables  
44  
45  
46 450 A5 and A8).

47  
48  
49  
50  
51 451

#### 52 452 *Zircon trace element compositions*

53  
54  
55 453 Twenty trace element spot analyses were obtained for zircons from samples of P1 to  
56  
57  
58 454 P3 porphyries (Digital Appendix Table A7; Fig. 15). It is common to encounter small

1  
2  
3  
4 455 mineral inclusions, especially of apatite, titanite, in zircon during LA-ICP-MS analyses  
5  
6 456 (e.g., Lu et al., 2016). We have taken Ca > 200 ppm or La > 0.3 ppm as an indication of  
7  
8  
9 457 apatite contamination, and Ti > 20 ppm to reflect titanite contamination, and such data  
10  
11 458 were excluded (Digital Appendix Table A7). The remaining analyses have low LREE  
12  
13  
14 459 and elevated HREE contents, with small negative Eu and strongly positive Ce anomalies  
15  
16 460 (Fig. 15). These REE patterns and total contents ( $\Sigma\text{REE} = 351\text{--}1125$  ppm), as well as  
17  
18  
19 461 Th/U ratios above 0.1 (0.26–0.63) (Digital Appendix Table A7) are typical of igneous  
20  
21 462 zircons from relatively oxidized magmas (Hoskin and Schaltegger, 2003).

22  
23  
24 463 Zircon crystals from the P1 to P3 porphyries show slightly different calculated Ti-in-  
25  
26 464 zircon temperatures and Eu anomalies ( $\text{Eu}_\text{N}/\text{Eu}_\text{N}^* = \text{Eu}_\text{N}/(\text{Sm}_\text{N} \times \text{Gd}_\text{N})^{0.5}$ ; Fig. 16; Digital  
27  
28  
29 465 Appendix Table A7). Titanium-in-zircon temperatures were calculated using the equation  
30  
31 466 of Ferry and Watson (2007), where it is assumed that  $\log a_{\text{SiO}_2} = 1$  because of the  
32  
33 467 existence of quartz in the host porphyries, and  $\log a_{\text{TiO}_2} = 0.7$  due to the presence of  
34  
35  
36 468 titanite (a common accessory mineral in these rocks). Zircon crystals from the P2E  
37  
38  
39 469 porphyry (sample RC13-107) have the highest calculated temperatures (average of  $760 \pm$   
40  
41 470  $29$  °C; range =  $723^\circ\text{--}819^\circ\text{C}$ ,  $n = 14$ ) with relatively uniform  $\text{Eu}_\text{N}/\text{Eu}_\text{N}^*$  values from 0.5 to  
42  
43  
44 471 0.7 (average =  $0.6 \pm 0.1$ ;  $n = 14$ ). Zircon crystals from the P3 porphyry (sample RC13-78)  
45  
46 472 show the lowest calculated temperatures (average =  $726 \pm 24$  °C; range =  $693^\circ\text{--}758^\circ\text{C}$ ,  $n$   
47  
48 473 = 18) and lowest  $\text{Eu}_\text{N}/\text{Eu}_\text{N}^*$  ratios ( $0.5 \pm 0.1$ ; range = 0.3–0.6,  $n = 18$ ). Zircon crystals  
49  
50  
51 474 from the P1 and P2L porphyries have intermediate calculated temperatures (P1:  $736 \pm$   
52  
53 475  $26$  °C, range =  $699^\circ\text{--}810^\circ\text{C}$ ,  $n = 16$ ; P2L:  $730 \pm 24$  °C, range =  $705^\circ\text{--}795^\circ\text{C}$ ,  $n = 17$ ),  
54  
55  
56 476 and a similar wide range of  $\text{Eu}_\text{N}/\text{Eu}_\text{N}^*$  values (P1: 0.3–1.0, average =  $0.6 \pm 0.2$ ; P2L: 0.3–  
57  
58 477 0.9, average =  $0.6 \pm 0.1$ ).

1  
2  
3  
4 478 Trace element compositions in zircon are sensitive to magmatic water content and  
5  
6  
7 479 oxygen fugacity, and have been used to distinguish between fertile and infertile suites in  
8  
9  
10 480 porphyry Cu ± Au ± Mo systems (Ballard et al., 2002; Liang et al., 2006; Qiu et al., 2014;  
11  
12 481 Wang et al., 2014b; Dilles et al., 2015; Shen et al., 2015; Lu et al., 2016; Xu et al., 2016;  
13  
14 482 Loader et al., 2017). In hydrous magmas, early plagioclase crystallization is suppressed  
15  
16 483 (Moore and Carmichael, 1998), leading to no pronounced depletion of Eu in melts (Eu<sup>2+</sup>  
17  
18 484 substitutes for Ca<sup>2+</sup> in plagioclase). On the other hand, in oxidized magmas, Eu is  
19  
20  
21 485 predominantly present as Eu<sup>3+</sup> and is partitioned into zircon along with other REE  
22  
23  
24 486 (Ballard et al., 2002; Hoskin and Schaltegger, 2003; Trail et al., 2011; Dilles et al., 2015).  
25  
26 487 Therefore, the small negative Eu anomalies in zircon samples (as indicated by Eu<sub>N</sub>/Eu<sub>N</sub><sup>\*</sup>  
27  
28 488 ratios >0.3 and mostly > 0.4; Fig. 16A), and slightly positive anomalies in whole rocks  
29  
30  
31 489 (Fig. 10) indicate relatively high magmatic water contents and/or oxidation states  
32  
33  
34 490 (Ballard et al., 2002; Dilles et al., 2015; Lu et al., 2016).

35  
36 491 Ballard et al. (2002) defined the zircon Ce<sup>4+</sup>/Ce<sup>3+</sup> ratio as an indicator of magmatic  
37  
38 492 oxidation state. However, Dilles et al. (2015) and Lu et al. (2016) argue that these values  
39  
40  
41 493 are difficult to estimate accurately because the abundances of the adjacent elements, La  
42  
43 494 and Pr, which are used as a baseline to calculate the magnitude of the Ce anomaly, are  
44  
45 495 low and close to the analytical detection limit. Confirming this reservation, Ce<sup>4+</sup>/Ce<sup>3+</sup>  
46  
47  
48 496 ratios and *f*O<sub>2</sub> values calculated for our samples using the equation of Trail et al. (2011)  
49  
50  
51 497 yielded unrealistic and widely variable ΔFMQ values (-9 to +5).

52  
53 498

54  
55 499 *Apatite compositions*  
56  
57  
58  
59  
60  
61  
62  
63  
64  
65

1  
2  
3  
4 500 The SO<sub>3</sub>, Cl, and F analyses of igneous apatites are listed in Digital Appendix Table  
5  
6 501 A8 and illustrated in Figures 17 and 18. The results show that igneous apatites from the  
7  
8 502 P2 porphyries have higher sulfur and chlorine concentrations than those from P1 and P3  
9  
10 503 rocks. The high SO<sub>3</sub> contents in apatites from the P2 porphyries (P2E: 0.11 to 0.8 wt. %  
11  
12 504 SO<sub>3</sub>, average = 0.30 ± 0.13 wt. %, n = 34; P2L: 0.07 to 1.2 wt. % SO<sub>3</sub>, average = 0.29 ±  
13  
14 505 0.18 wt. %, n = 100) are similar to values from global porphyry Cu deposits (Streck and  
15  
16 506 Dilles, 1998; Imai, 2002; Li et al., 2012; Pan et al., 2016; Richards et al., 2017). In  
17  
18 507 comparison, apatite crystals from the P1 porphyry (RC13-39) have lower sulfur contents  
19  
20 508 (0.05 to 0.19 wt. % SO<sub>3</sub>; average = 0.11 ± 0.03 wt. %, n = 34), whereas those from the P3  
21  
22 509 porphyry (RC13-78) have the lowest sulfur concentrations (from 0.05 wt. % to below the  
23  
24 510 analytical detection limit of SO<sub>3</sub>; average of analyses above limit of detection = 0.03 ±  
25  
26 511 0.01, n = 13). Although the ranges for P1 and P2L porphyries overlap at their outer limits,  
27  
28 512 a t-test shows that the two populations are significantly different (t = 5.87, p = 0).

29  
30  
31 513 Similarly, the Cl contents in apatite crystals from P1 and P3 porphyries are  
32  
33 514 significantly lower (0.51 ± 0.3 wt. %, n = 34, and 0.1 ± 0.06 wt. %, n = 17, respectively)  
34  
35 515 compared to values from the P2 porphyries (P2E: 1.18 ± 0.37 wt. %, n = 34; P2L: 1.47 ±  
36  
37 516 0.28 wt. %, n = 100). There is a rough positive correlation between sulfur and chlorine  
38  
39 517 contents of apatites from the four porphyries (Fig. 18A), with relatively constant molar  
40  
41 518 S/Cl ratios (P1: 0.13 ± 0.08, n = 34; P2E: 0.13 ± 0.08, n = 34; P2L: 0.10 ± 0.14, n = 100;  
42  
43 519 P3: 0.16 ± 0.09, n = 13; Table 4). Detailed analyses also show that single apatite crystals  
44  
45 520 are commonly zoned in sulfur, with decreasing core-to-rim SO<sub>3</sub> contents (and small  
46  
47 521 decreases in Cl; Fig. 17C), possibly reflecting progressive degassing of SO<sub>2</sub> (and Cl)  
48  
49 522 from the melt during crystallization (Richards et al., 2017).  
50  
51  
52  
53  
54  
55  
56  
57  
58  
59  
60  
61  
62  
63  
64  
65

1  
2  
3  
4 523 Fluorine contents in apatites from the P1 and P3 porphyries are similar (P1:  $3.64 \pm$   
5  
6 524  $0.48$  wt. %,  $n = 34$ ; P3:  $3.6 \pm 0.4$ ,  $n = 17$ ) and distinctly higher than in the P2E ( $2.33 \pm$   
7  
8  
9 525  $0.29$  wt. %,  $n = 34$ ) and P2L ( $2.32 \pm 0.23$  wt. %,  $n = 100$ ) porphyries.

10  
11 526 Some hydrothermal apatite grains were also analyzed for comparison with igneous  
12  
13 527 grains, and they show wide variations in sulfur and chlorine content (Digital Appendix  
14  
15 528 Table A8), as observed by other researchers (e.g., Li et al., 2012; Richards et al., 2017).

16  
17  
18 529 The sulfur partition coefficient between apatite and melt is jointly controlled by  
19  
20 530 temperature, oxygen fugacity, and the S content in the silicate melt (Peng et al., 1997;  
21  
22 531 Parat and Holtz, 2005; Parat et al., 2011; Webster and Piccoli, 2015; Konecke et al.,  
23  
24 532 2017a, b), and no formula currently exists to accurately calculate magmatic sulfur  
25  
26 533 concentrations from apatite  $SO_3$  contents. However, two semi-quantitative formulae can  
27  
28 534 be used to estimate relative magmatic S content (Peng et al., 1997; Parat et al., 2011).  
29  
30 535 Using the equation of Peng et al. (1997), the magmas related to the P2E and P2L  
31  
32 536 porphyry intrusions are calculated to have sulfur concentrations of  $0.03 \pm 0.01$  wt. % ( $n =$   
33  
34 537  $34$ ) and  $0.02 \pm 0.01$  wt. % ( $n = 100$ ), significantly higher than the corresponding S  
35  
36 538 contents for P1 ( $0.010 \pm 0.003$  wt. % S,  $n = 34$ ) and P3 magmas ( $0.003 \pm 0.001$  wt. % S,  
37  
38 539  $n = 13$ ; Table 4). The results calculated by the method of Parat et al. (2011) are more  
39  
40 540 variable, and yielded lower absolute values than those from Peng et al. (1997). However,  
41  
42 541 they also support the conclusion that the P2E and P2L magmas had significantly higher  
43  
44 542 sulfur contents than the P1 and P3 magmas (Table 4).

45  
46 543 The chlorine partition coefficient between apatite and melt is a complex function of  
47  
48 544 magma composition and Cl concentration in the melt (Zhu and Sverjensky, 1991; Piccoli  
49  
50 545 and Candela, 1994; Mathez and Webster, 2005; Webster et al., 2009; Chelle-Michou and  
51  
52  
53  
54  
55  
56  
57  
58  
59  
60  
61  
62  
63  
64  
65

1  
2  
3  
4 546 Chiaradia, 2017). Mathez and Webster (2005) proposed a value of 0.8 as the partition  
5  
6 547 coefficient (mass ratio) between apatite and basaltic melt (51.1 wt. % SiO<sub>2</sub>). Based on  
7  
8 548 this semi-quantitative equation (and recognizing that these magmas were not basaltic), we  
9  
10 549 estimate Cl concentrations in the P2E and P2L magmas of  $1.48 \pm 0.46$  wt.% (n = 34) and  
11  
12 550  $1.83 \pm 0.34$  wt.% (n = 100), respectively, significantly higher than for P1 ( $0.63 \pm 0.38$   
13  
14 551 wt.%, n = 34) and P3 ( $0.12 \pm 0.07$  wt.%; Table 4).  
15  
16  
17  
18  
19  
20

## 21 553 **Discussion**

### 22 554 *Magmatic duration and timing of ore formation at Red Chris*

23  
24  
25 555 Four phases of the Red Stock, P1, P2E, P2L, and P3, have been dated at  $211.6 \pm 1.3$   
26  
27 556 Ma,  $206.0 \pm 1.2$  Ma,  $203.6 \pm 1.8$  Ma, and  $201.7 \pm 1.2$  Ma, respectively, spanning a period  
28  
29 557 of ~10 m.y. (Fig. 6; Digital Appendix Table A2). These ages are consistent with  
30  
31 558 crosscutting relationships described by Rees et al. (2015). Re-Os dating of molybdenite  
32  
33 559 intergrown with chalcopyrite in quartz veins yielded a weighted mean age of  $206.1 \pm 0.5$   
34  
35 560 Ma (Fig. 7), reflecting the timing of mineralization and in good agreement with the  
36  
37 561 emplacement age of the mineralized P2E quartz monzonite porphyry. Ore formation  
38  
39 562 occurred at a relatively late stage in the ~10 m.y. evolution of the Red Stock, and over a  
40  
41 563 relatively brief period time (<1 m.y., as defined by the uncertainty on the average of three  
42  
43 564 Re-Os analyses). This relatively late and short duration of mineralization is similar to the  
44  
45 565 timing observed in many other porphyry deposits (e.g., Cathles et al., 1997; Masterman et  
46  
47 566 al., 2004; von Quadt et al., 2011; Chiaradia et al., 2013; Correa et al., 2016; Li et al.,  
48  
49 567 2017).  
50  
51  
52  
53  
54  
55  
56  
57  
58  
59  
60  
61  
62  
63  
64  
65

1  
2  
3  
4 568 The age of mineralization at ~206 Ma is contemporaneous with the major pulse of  
5  
6 569 mineralization in the Stikine and Quesnel terranes, representing a particularly fertile pre-  
7  
8  
9 570 accretionary magmatic event (Nelson and Colpron, 2007; Nelson et al., 2013; Logan and  
10  
11 571 Mihalynuk, 2014).

12  
13  
14 572

15  
16 573 *Igneous geochemistry and petrogenesis*

17  
18  
19 574 Whole-rock major and trace element compositions of P1 to P3 porphyry rocks are  
20  
21 575 almost identical to each other, and show characteristics of subduction-related magmatic  
22  
23 576 rocks with high LILE and low HFSE concentrations (Figs. 9 and 10; Hawkesworth et al.,  
24  
25 577 1993; Pearce, 1996). The high Sr/Y ratios ( $53 \pm 23$ ,  $n = 12$ ) and slightly positive Eu  
26  
27 578 anomalies ( $Eu_n/Eu_n^* = 1.1 \pm 0.15$ ;  $n = 14$ ) indicate the suppression of plagioclase  
28  
29 579 crystallization and early crystallization of amphibole from hydrous and oxidized magmas  
30  
31 580 (Richards and Kerrich, 2007; Loucks, 2014). Rees et al. (2015) concluded from their  
32  
33 581 analysis of petrochemistry that the Red Stock evolved from subalkaline (P1, P2) to  
34  
35 582 marginally alkaline (P3), and classified the overall system as high-K calc-alkalic.

36  
37  
38 583 All the porphyritic rocks from P1 to P3 show mantle-like, relatively low  $(^{87}\text{Sr}/^{86}\text{Sr})_t$   
39  
40 584 ( $0.7044 \pm 0.0002$ ) and high  $\epsilon_{\text{Nd}}(t)$  ( $+3.1 \pm 0.4$ ) values, and similar single-stage Nd model  
41  
42 585 ages ( $0.80 \pm 0.05$  Ga). Zircon crystals from these rocks yield positive zircon  $\epsilon_{\text{Hf}}(t)$  values  
43  
44 586 ( $+8.1$  to  $+14.8$ ) and single-stage Hf model ages of  $375 \pm 52$  Ma (Figs. 11 and 12). These  
45  
46 587 data indicate minimal involvement of ancient crustal components in the petrogenesis of  
47  
48 588 these magmas, as observed for other Mesozoic igneous rocks in the Stikine terrane, and  
49  
50 589 are consistent with an oceanic island arc setting (Samson et al., 1989; Logan and  
51  
52 590 Mihalynuk, 2014).



1  
2  
3  
4 591 Late basaltic to andesitic dikes have similar Nd–Sr isotopic compositions to the  
5  
6 592 porphyritic rocks, but show distinct trace element and REE patterns, and lower Sr/Y and  
7  
8  
9 593 La/Yb ratios, suggesting that they are not cogenetic.  
10

11 594

12  
13  
14 595 *Oxygen fugacity and sulfur-chlorine-water contents of the porphyry magmas*

15  
16 596 Magmatic oxidation state, and sulfur, chlorine, and water contents are fundamental  
17  
18 597 factors for the formation of porphyry Cu deposits (e.g., Burnham, 1979; Candela, 1992;  
19  
20  
21 598 Richards, 2003; Loucks, 2014). It is difficult to measure the original magmatic oxidation  
22  
23 599 state in altered plutonic rocks, but normalized Ce and Eu anomalies in zircons can be  
24  
25  
26 600 used to provide qualitative estimates (Ballard et al., 2002; Dilles et al., 2015; Lu et al.,  
27  
28  
29 601 2016). Zircon grains from the P1 to P3 porphyries display large positive Ce and small  
30  
31 602 negative Eu anomalies ( $Eu_N/Eu_N^*$  mostly  $> 0.4$ ; Figs. 15 and 16), similar to zircons from  
32  
33 603 other mineralized porphyry systems worldwide (Wang et al., 2014b; Dilles et al., 2015;  
34  
35  
36 604 Lu et al., 2016). These data are also consistent with estimates of magmatic oxidation state  
37  
38 605 from early stage amphibole phenocrysts from the P2E and P2L porphyries, which yielded  
39  
40  
41 606  $\Delta FMQ$  values of  $1.5 \pm 0.2$  ( $n = 7$ ) and  $1.1 \pm 0.3$  ( $n = 44$ ). Consequently, we conclude that  
42  
43 607 the four phases of magma in the Red Stock were all at least moderately oxidized.  
44

45  
46 608 It is similarly difficult to estimate original magmatic water contents from altered  
47  
48 609 plutonic rocks. However, the presence of amphibole phenocrysts in the P1 to P3  
49  
50  
51 610 porphyries suggest that the magmas contained at least 4 wt. %  $H_2O$  (Burnham, 1979,  
52  
53 611 Naney, 1983; Merzbacher and Egger, 1984; Rutherford and Devine, 1988; Ridolfi et al.,  
54  
55  
56 612 2010). This observation is supported by: (1) high whole-rock Sr/Y ratios ( $53 \pm 23$ ,  $n =$   
57  
58 613 12), which reflect the suppression of plagioclase relative to amphibole crystallization  
59  
60  
61  
62  
63  
64  
65

1  
2  
3  
4 614 under hydrous conditions (Moore and Carmichael, 1998; Richards and Kerrich, 2007); (2)  
5  
6 615 high  $10000 \times (\text{Eu}_N/\text{Eu}_N^*)/Y$  ( $>1$ ) and low Dy/Yb ( $<0.3$ ) ratios in zircons (Digital Appendix  
7  
8  
9 616 Table A7; Lu et al., 2016); (3) high whole-rock V/Sc ratios ( $9.0 \pm 0.9$ ,  $n = 14$ ) (Loucks,  
10  
11 617 2014); and (4) estimates of magmatic water content from plagioclase phenocryst  
12  
13  
14 618 compositions, which indicate values of  $\sim 5$  wt.%  $\text{H}_2\text{O}$ .

15  
16 619 The compositions of igneous apatite inclusions in plagioclase and amphibole  
17  
18 620 phenocrysts have been used to estimate magmatic sulfur and chlorine contents. The  
19  
20  
21 621 results suggest that apatite microphenocrysts from the P2E and P2L porphyries had  
22  
23  
24 622 higher S and Cl contents than for P1 and P3 (Fig. 18). The  $\text{SO}_3$  contents in apatite are  
25  
26 623 controlled by both magmatic sulfur concentration and oxidation state (Peng et al., 1997;  
27  
28 624 Parat and Holtz, 2005; Webster and Piccoli, 2015). Sulfur occurs in the apatite structure  
29  
30  
31 625 mainly as  $\text{S}^{6+}$  and its content will increase in relatively oxidized environments (Boyce et  
32  
33  
34 626 al., 2010; Parat et al., 2011; Konecke et al., 2017b). The magmas associated with the four  
35  
36 627 porphyry phases at Red Chris were all moderately oxidized, and therefore the differences  
37  
38 628 in apatite sulfur content likely mainly reflect variations in the sulfur fugacity in the  
39  
40  
41 629 associated melts. The data indicate that the P2E and P2L porphyry magmas contained  
42  
43  
44 630 significantly higher S contents than the P1 and P3 magmas (Fig. 18). Models used to  
45  
46 631 estimate magmatic sulfur content in equilibrium with apatite (Peng et al., 1997) are not  
47  
48 632 strictly accurate because of uncertainties in the details of exchange reactions (Streck and  
49  
50  
51 633 Dilles, 1998; Mao et al., 2016) but are expected to be correct in relative terms. Our data  
52  
53 634 yield higher values for the P2E and P2L porphyries (0.02–0.03 wt. % S) compared to  
54  
55 635 estimates for P1 (0.01 wt. % S) and P3 (0.003 wt. % S). Consequently, we conclude that

1  
2  
3  
4 636 the syn-mineral porphyry (P2E and P2L) magmas were more S-rich than the pre-  
5  
6 637 mineralization P1 and especially the post-mineralization P3 porphyry magmas.

7  
8  
9 638 Similarly, the magmatic Cl contents calculated from apatite compositions in the P2E  
10  
11 639 and P2L porphyries are also higher than in the P1 and P3 porphyries, whereas F contents  
12  
13 640 are lower (Table 4). Volatile species such as S, Cl, and F are differentially affected by  
14  
15 641 degassing during ascent and crystallization of magmas: S and Cl will be preferentially  
16  
17 642 lost to the vapor phase relative to F (Webster et al., 2014; Stock et al., 2016), leading to  
18  
19 643 high F/Cl and F/S ratios in degassed magmas. The data shown in Figure 18 suggest that  
20  
21 644 the P2E and P2L were S-Cl-rich, whereas the P1 and P3 were S-Cl-poor but enriched in F.

22  
23  
24  
25  
26 645 These differences could reflect either loss of volatiles from the source magma  
27  
28 646 chamber (presumed to be an underlying batholith) prior to emplacement of the P1 and P3  
29  
30 647 magmas but not in the case of P2, or conversely addition of a volatile phase or a volatile-  
31  
32 648 rich magma to the magma chamber immediately prior to emplacement of P2. Volatile  
33  
34 649 loss is expected to be a general condition of upper crustal magma emplacement, and this  
35  
36 650 may well be a factor contributing to the low Cl/F ratios in the late P3 magmas, as well as  
37  
38 651 the negatively correlated trend for F and Cl in P1. The P2 magma was emplaced after P1,  
39  
40 652 and so might be expected to be similarly degassed if this represents a comagmatic  
41  
42 653 sequence. However, the 6–8 m.y. age difference between P1 ( $211.6 \pm 1.3$  Ma) and P2  
43  
44 654 (P2E:  $206.0 \pm 1.2$  Ma; P2L:  $203.6 \pm 1.8$  Ma) indicates that P1 and P2 are not directly  
45  
46 655 comagmatic. One explanation is that the P2 event represents a pulse of S-Cl-rich magma  
47  
48 656 injected at a relatively late stage into the mid-crustal magma reservoir, leading to a pulse  
49  
50 657 of fluid exsolution and injection of P2 magma into the shallower level Red Stock, where  
51  
52 658 syn-P2, quartz-vein hosted mineralization formed the Red Chris Cu-Au deposit. The  
53  
54  
55  
56  
57  
58  
59  
60  
61  
62  
63  
64  
65

1  
2  
3  
4 659 post-mineralization P3 ( $201.7 \pm 1.2$  Ma) and P4 porphyries may represent the final stages  
5  
6 660 of intrusive activity emanating from the now degassed underlying magma chamber.  
7  
8

9 661 Although both P2E and P2L porphyries are S-Cl-rich, apatites from P2L are  
10  
11 662 marginally the most enriched. Samples of P2L are also the most mafic ( $\text{SiO}_2$ -poor) in the  
12  
13  
14 663 suite, and it is therefore tempting to speculate that the source magma chamber was  
15  
16 664 recharged with more mafic, S-Cl- $\text{H}_2\text{O}$ -rich magma during the P2 stage. The solubility of  
17  
18  
19 665 S and Cl is higher in oxidized mafic magmas compared to felsic melts ( $> 1000$  ppm S  
20  
21 666 and  $> 3000$  ppm Cl; Carmichael and Ghiorso, 1986; Webster, 1997; Webster et al., 1999;  
22  
23  
24 667 Hattori and Keith, 2001; Jugo et al., 2005; Jugo, 2009; Chelle-Michou and Chiaradia,  
25  
26 668 2017). Therefore, a key step in porphyry ore formation at Red Chris may have been  
27  
28  
29 669 recharge of the batholithic system by a less evolved, although broadly cogenetic, magma  
30  
31 670 (cf. Hattori and Keith, 2001; Steinberger et al., 2013; Large et al., 2018).  
32

33 671 Support for this recharge model is provided by high magmatic temperatures  
34  
35  
36 672 calculated from zircon grains from some P2 samples (Fig. 16), and reverse zoning  
37  
38 673 observed in plagioclase phenocrysts from the P2E and P2L porphyries, but which is not  
39  
40  
41 674 observed in P3 (Fig. 14C). In detail, zircons from the P2E porphyry show the highest Ti-  
42  
43 675 in-zircon temperatures and  $\text{Eu}_N/\text{Eu}_N^*$  values, and P3 the lowest values. This might reflect  
44  
45  
46 676 an influx of higher temperature melt during the evolution of the P2E magma, and greater  
47  
48 677 degrees of plagioclase fractionation from the late P3 magma. The compositional ranges  
49  
50  
51 678 of up to  $\sim 19$  mol % An for plagioclase are higher than the upper limit caused by chemical  
52  
53 679 diffusion ( $\sim 10$  mol % An; Pearce and Kolisnik, 1990). Furthermore, these reverse zoning  
54  
55  
56 680 patterns are matched by FeO contents in the phenocrysts (Figs. 14A and 14B), which  
57  
58 681 suggests that the zonation reflects changes in magma composition (as opposed to simply  
59  
60  
61  
62  
63  
64  
65

1  
2  
3  
4 682 changes in pressure, temperature, or water content; Ginibre and Wörner, 2007; Lange,  
5  
6 683 2009; Ustunisik et al., 2014; Waters and Lange, 2015). We therefore interpret these  
7  
8  
9 684 changes to reflect late-stage (rim) growth from a more mafic magma that mixed into a  
10  
11 685 more evolved resident magma.  
12  
13  
14 686

## 687 **Conclusions**

688 Zircon U-Pb ages indicate that the Red Stock was emplaced over a period of ~10 m.y.  
689 (211.6 ± 1.3 Ma, 206.0 ± 1.2 Ma, 203.6 ± 1.8 Ma, and 201.7 ± 1.2 Ma for the P1, P2E,  
690 P2L, and P3 porphyries, respectively). The ore-forming event at Red Chris occurred  
691 relatively late in this magmatic history, synchronous with P2E at 206.1 ± 0.5 Ma, and  
692 over a short period of <1 m.y. (as constrained by the error on the average of three Re-Os  
693 analyses). The four phases of porphyry and their related magmas were chemically fairly  
694 homogeneous and isotopically primitive, consistent with an island arc origin. The  
695 magmas were all moderately oxidized and hydrous (~5 wt. H<sub>2</sub>O), but the P2 magmas had  
696 distinctly higher S and Cl contents. Combined with evidence for reverse zonation in  
697 plagioclase phenocrysts from P2 porphyries, and more mafic compositions in P2L, we  
698 suggest that the deeper source magma chamber was recharged at the time of  
699 emplacement of the P2 porphyries by injection of a more mafic S-Cl-rich magma. This  
700 recharge process may have triggered ore formation by causing voluminous exsolution of  
701 metalliferous hydrothermal fluids.

702

703

## **Acknowledgements**

1  
2  
3  
4 704 This research was funded by a Collaborative Research and Development Grant from  
5  
6 705 Natural Sciences and Engineering Research Council of Canada and the Red Chris  
7  
8  
9 706 Development Company Ltd. (RCDC) to JPR, and a post-doctoral fellowship from China  
10  
11 707 Scholarship Council, University of Alberta, and Institute of Geochemistry, Chinese  
12  
13  
14 708 Academy of Sciences to JJZ. RCDC provided access to the Red Chris mine by Jürgen  
15  
16 709 Lang to collect samples from drill core in 2014. Prof. Zhaochu Hu from China University  
17  
18  
19 710 of Geosciences at Wuhan, China is thanked for help with in-situ zircon LA-ICP-MS Hf  
20  
21 711 isotope analyses, which was funded by the National Natural Science Foundation Project  
22  
23  
24 712 of China (41673049 and 41303040), and the National Key Research and Development  
25  
26 713 Program of China (2016YFC0600503) to JJZ. We particularly thank Steve Robertson and  
27  
28  
29 714 ‘Lyn Anglin from RCDC for support of this project. We thank David Cooke and Adam  
30  
31 715 Bath for constructive reviews of the manuscript.  
32  
33  
34 716

## 35 36 717 **References**

- 37  
38 718 Annen, C., Blundy, J., and Sparks, R., 2006, The genesis of intermediate and silicic  
39  
40 719 magmas in deep crustal hot zones: *Journal of Petrology*, v. 47, p. 505–539.  
41  
42 720 Ash, C.H., Fraser, T.M., Blanchflower, J.D. and Thurston, B.G., 1995, Tatogga Lake  
43  
44 721 project, north western British Columbia (104H/11, 12); in *Geological Field work 1994*,  
45  
46 722 BC Ministry of Energy, Mines and Petroleum Resources, Paper 1995-1, p. 343–358.  
47  
48 723 Ash, C.H., Stinson, P.K., and Macdonald, R.W.J., 1996, Geology of the Todagin plateau  
49  
50 724 and Kinaskan Lake area, northwestern British Columbia (104H/12, 104G/9): B.C.  
51  
52 725 Ministry of Energy, Mines and Petroleum Resources Paper 1996-1, p. 155–174.  
53  
54 726 Baker, T., Ash, C., and Thompson, J., 1997, Geological setting and characteristics of the  
55  
56 727 Red Chris porphyry copper-gold deposit, northwestern British Columbia: *Exploration*  
57  
58 728 *Mining Geology*, v. 6, p. 297–316.  
59  
60 729 Ballard, J. R., Palin, M. J., and Campbell, I. H., 2002, Relative oxidation states of  
61  
62 730 magmas inferred from  $Ce^{(IV)}/Ce^{(III)}$  in zircon: application to porphyry copper deposits  
63  
64 731 of northern Chile: *Contributions to Mineralogy and Petrology*, v. 144, p. 347–364.  
65

1  
2  
3  
4  
5  
6  
7  
8  
9  
10  
11  
12  
13  
14  
15  
16  
17  
18  
19  
20  
21  
22  
23  
24  
25  
26  
27  
28  
29  
30  
31  
32  
33  
34  
35  
36  
37  
38  
39  
40  
41  
42  
43  
44  
45  
46  
47  
48  
49  
50  
51  
52  
53  
54  
55  
56  
57  
58  
59  
60  
61  
62  
63  
64  
65

732 Bath, A. B., Cooke, D. R., Friedman, R. M., Faure, K., Kamenetsky, V. S., Tosdal, R. M.,  
733 and Berry, R. F., 2014, Mineralization, U-Pb geochronology, and stable isotope  
734 geochemistry of the lower main zone of the Lorraine deposit, north-central British  
735 Columbia: a replacement-style alkalic Cu-Au porphyry: *Economic Geology*, v. 109, p.  
736 979–1004.

737 Bell, A. S., and Simon, A., 2011, Experimental evidence for the alteration of the  $Fe^{3+}/\Sigma Fe$   
738 of silicate melt caused by the degassing of chlorine-bearing aqueous volatiles:  
739 *Geology*, v. 39, p. 499–502.

740 Bissig, T., and Cooke, D. R., 2014, Introduction to the special issue devoted to alkalic  
741 porphyry Cu-Au and epithermal Au Deposits: *Economic Geology*, v. 109, p. 819–825.

742 Blundy, J., Mavrogenes, J., Tattitch, B., Sparks, S., and Gilmer, A., 2015, Generation of  
743 porphyry copper deposits by gas-brine reaction in volcanic arcs: *Nature Geoscience*, v.  
744 8, p. 235–240.

745 Boyce, J. W., Liu, Y., Rossman, G. R., Guan, Y., Eiler, J. M., Stolper, E. M., and Taylor,  
746 L. A., 2010, Lunar apatite with terrestrial volatile abundances: *Nature*, v. 466, p. 466.

747 Brown, D. A., Logan, J. M., Gunning, M. H., Orchard, M. J., and Bamber, W. E., 1991,  
748 Stratigraphic evolution of the Paleozoic Stikine assemblage in the Stikine and Iskut  
749 rivers area, northwestern British Columbia: *Canadian Journal of Earth Sciences*, v. 28,  
750 p. 958–972.

751 Brown, P., and Kahlert, B., 1986, Geology and mineralization of the Red Mountain  
752 porphyry molybdenum deposit, south-central Yukon: *Canadian Institute of Mining  
753 and Metallurgy, Special Volume 37*, p. 288–297.

754 Burgisser, A., and Scaillet, B., 2007, Redox evolution of a degassing magma rising to the  
755 surface: *Nature*, v. 445, p. 194–197.

756 Burnham, C.W., 1979, Magmas and hydrothermal fluids, in Barnes, H.L., ed.,  
757 *Geochemistry of hydrothermal ore deposits*, 2nd ed.: New York, John Wiley and Sons,  
758 p. 71–136.

759 Byrne, K., and Tosdal, R. M., 2014, Genesis of the Late Triassic southwest zone breccia-  
760 hosted alkalic porphyry Cu-Au deposit, Galore Creek, British Columbia, Canada:  
761 *Economic Geology*, v. 109, p. 915–938.

762 Candela, P. A., 1986, The evolution of aqueous vapor from silicate melts: effect on  
763 oxygen fugacity: *Geochimica et Cosmochimica Acta*, v. 50, p. 1205–1211.

764 Candela, P. A., 1992, Controls on ore metal ratios in granite-related ore systems: an  
765 experimental and computational approach: *Transactions of the Royal Society of  
766 Edinburgh, Earth Sciences*, v. 83, p. 317–326.

- 1  
2  
3  
4 767 Candela, P.A., and Holland, H.D., 1984, The partitioning of copper and molybdenum  
5 768 between silicate melts and aqueous fluids: *Geochimica et Cosmochimica Acta*, v. 48, p.  
6 769 373–380.
- 7  
8  
9 770 Carmichael, I. S., and Ghiorso, M. S., 1986, Oxidation-reduction relations in basic  
10 771 magma: a case for homogeneous equilibria: *Earth and Planetary Science Letters*, v. 78,  
11 772 p. 200–210.
- 12  
13 773 Cathles, L. M., Erendi, A., and Barrie, T., 1997, How long can a hydrothermal system be  
14 774 sustained by a single intrusive event?: *Economic Geology*, v. 92, p. 766–771
- 15  
16 775 Chambefort, I., Dilles, J. H., and Kent, A. J. R., 2008, Anhydrite-bearing andesite and  
17 776 dacite as a source for sulfur in magmatic-hydrothermal mineral deposits: *Geology*, v.  
18 777 36, p. 719–722.
- 19  
20  
21 778 Chelle-Michou, C., and Chiaradia, M., 2017, Amphibole and apatite insights into the  
22 779 evolution and mass balance of Cl and S in magmas associated with porphyry copper  
23 780 deposits: *Contributions to Mineralogy and Petrology*, v. 172, 105, doi:  
24 781 <https://doi.org/10.1007/s00410-017-1417-2>
- 25  
26  
27 782 Chiaradia, M., Ulianov, A., Kouzmanov, K., and Beate, B., 2012, Why large porphyry Cu  
28 783 deposits like high Sr/Y magmas?: *Scientific reports*, v. 2, 685.
- 29  
30 784 Chiaradia, M., Schaltegger, U., Spikings, R., Wotzlaw, J.-F., and Ovtcharova, M., 2013,  
31 785 How accurately can we date the duration of magmatic-hydrothermal events in  
32 786 porphyry systems?—An invited paper: *Economic Geology*, v. 108, p. 565–584.
- 33  
34 787 Correa, K. J., Rabbia, O. M., Hernández, L. B., Selby, D., and Astengo, M., 2016, The  
35 788 timing of magmatism and ore formation in the El Abra porphyry copper deposit,  
36 789 northern Chile: implications for long-lived multiple-event magmatic-hydrothermal  
37 790 porphyry Systems: *Economic Geology*, v. 111, p. 1–28.
- 38  
39  
40 791 Creasey, S., 1977, Intrusives associated with porphyry copper deposits: *Bulletin of the*  
41 792 *Geological Society of Malaysia*, v. 9, p. 51–66.
- 42  
43  
44 793 Devine, F. A. M., Chamberlain, C. M., Davies, A. G. S., Friedman, R., and Baxter, P.,  
45 794 2014, Geology and district-scale setting of tilted alkalic porphyry Cu-Au  
46 795 mineralization at the Lorraine deposit, British Columbia: *Economic Geology*, v. 109, p.  
47 796 939–977.
- 48  
49  
50 797 Dilles, J. H., Kent, A. J., Wooden, J. L., Tosdal, R. M., Koleszar, A., Lee, R. G., and  
51 798 Farmer, L. P., 2015, Zircon compositional evidence for sulfur-degassing from ore-  
52 799 forming arc magmas: *Economic Geology*, v. 110, p. 241–251.
- 53  
54 800 Dostal, J., Gale, V., and Church, B., 1999, Upper Triassic Takla Group volcanic rocks,  
55 801 Stikine Terrane, north-central British Columbia: geochemistry, petrogenesis, and  
56 802 tectonic implications: *Canadian Journal of Earth Sciences*, v. 36, p. 1483–1494.
- 57  
58  
59  
60  
61  
62  
63  
64  
65



1  
2  
3  
4  
5  
6  
7  
8  
9  
10  
11  
12  
13  
14  
15  
16  
17  
18  
19  
20  
21  
22  
23  
24  
25  
26  
27  
28  
29  
30  
31  
32  
33  
34  
35  
36  
37  
38  
39  
40  
41  
42  
43  
44  
45  
46  
47  
48  
49  
50  
51  
52  
53  
54  
55  
56  
57  
58  
59  
60  
61  
62  
63  
64  
65

803 Duuring, P., Rowins, S. M., McKinley, B. S. M., Dickinson, J. M., Diakow, L. J., Kim,  
804 Y.-S., and Creaser, R. A., 2009, Magmatic and structural controls on porphyry-style  
805 Cu–Au–Mo mineralization at Kemess South, Toodoggone District of British  
806 Columbia, Canada: *Mineralium Deposita*, v. 44, p. 435–462.

807 Ferry, J., and Watson, E., 2007, New thermodynamic models and revised calibrations for  
808 the Ti-in-zircon and Zr-in-rutile thermometers: *Contributions to Mineralogy and*  
809 *Petrology*, v. 154, p. 429–437.

810 Friedman, R.M., and Ash, C.H., 1997, U-Pb age of intrusions related to porphyry Cu-Au  
811 mineralization in the Tatogga Lake area, northwestern British Columbia: B.C.  
812 Ministry of Employment and Investment Paper 1997-1, p. 291–297.

813 Gabrielse, H., 1991, Late Paleozoic and Mesozoic terrane interactions in north-central  
814 British Columbia: *Canadian Journal of Earth Sciences*, v. 28, p. 947–957.

815 Gagnon, J.-F., Barresi, T., Waldron, J. W., Nelson, J., Poulton, T., and Cordey, F., 2012,  
816 Stratigraphy of the upper Hazelton Group and the Jurassic evolution of the Stikine  
817 terrane, British Columbia 1 1 ESS Contribution 20120051: *Canadian Journal of Earth*  
818 *Sciences*, v. 49, p. 1027–1052.

819 Gillstrom, G., Anand, R., Robertson, S., and Sterling, P., 2012, 2012 technical report on  
820 the Red Chris copper-gold project, for Imperial Metals Corp (Amended and Restated  
821 at 2015). [https://www.imperialmetals.com/assets/docs/red-chris-43-101-report-sept-](https://www.imperialmetals.com/assets/docs/red-chris-43-101-report-sept-30-2015.pdf)  
822 [30-2015.pdf](https://www.imperialmetals.com/assets/docs/red-chris-43-101-report-sept-30-2015.pdf).

823 Ginibre, C., and Wörner, G., 2007, Variable parent magmas and recharge regimes of the  
824 Parinacota magma system (N. Chile) revealed by Fe, Mg and Sr zoning in plagioclase:  
825 *Lithos*, v. 98, p. 118–140.

826 Goldstein, S., O’Nions, R., and Hamilton, P., 1984, A Sm-Nd isotopic study of  
827 atmospheric dusts and particulates from major river systems: *Earth and planetary*  
828 *Science letters*, v. 70, p. 221–236.

829 Gustafson, L.B., and Hunt, J.P., 1975, The porphyry copper deposit at El Salvador, Chile:  
830 *Economic Geology*, v. 70, p. 857–912.

831 Halter, W. E., Heinrich, C. A., and Pettke, T., 2005, Magma evolution and the formation  
832 of porphyry Cu-Au ore fluids: evidence from silicate and sulfide melt inclusions:  
833 *Mineralium Deposita*, v. 39, p. 845–863.

834 Harris, A. C., Dunlap, W. J., Reiners, P. W., Allen, C. M., Cooke, D. R., White, N. C.,  
835 Campbell, I. H., and Golding, S. D., 2008, Multimillion year thermal history of a  
836 porphyry copper deposit: application of U–Pb, <sup>40</sup>Ar/<sup>39</sup>Ar and (U–Th)/He chronometers,  
837 Bajo de la Alumbrera copper–gold deposit, Argentina: *Mineralium Deposita*, v. 43, p.  
838 295–314.

- 1  
2  
3  
4 839 Hattori, K., 1993, High-sulfur magma, a product of fluid discharge from underlying  
5 mafic magma: evidence from Mount Pinatubo, Philippines: *Geology*, v. 21, p. 1083–  
6 840  
7 841 1086.
- 8  
9 842 Hattori, K. H., and Keith, J. D., 2001, Contribution of mafic melt to porphyry copper  
10 843 mineralization: evidence from Mount Pinatubo, Philippines, and Bingham Canyon,  
11 844 Utah, USA: *Mineralium Deposita*, v. 36, p. 799–806.
- 12  
13 845 Hawkesworth, C., Gallagher, K., Hergt, J., and McDermott, F., 1993, Mantle and slab  
14 846 contributions in arc magmas: *Annual Review of Earth and Planetary Sciences*, v. 21, p.  
15 847 175–204.
- 16  
17 848 Hayba, D. O., and Ingebritsen, S. E., 1997, Multiphase groundwater flow near cooling  
18 849 plutons: *Journal of Geophysical Research*, v. 102, p. 235–252.
- 19  
20 850 Hoskin, P. W., and Schaltegger, U., 2003, The composition of zircon and igneous and  
21 851 metamorphic petrogenesis: *Reviews in mineralogy and geochemistry*, v. 53, p. 27–62.
- 22  
23 852 Hou, Z., Yang, Z., Lu, Y., Kemp, A., Zheng, Y., Li, Q., Tang, J., Yang, Z., and Duan, L.,  
24 853 2015, A genetic linkage between subduction-and collision-related porphyry Cu  
25 854 deposits in continental collision zones: *Geology*, v. 43, p. 247–250.
- 26  
27 855 Imai, A., 2002, Metallogenesis of porphyry Cu deposits of the western Luzon arc,  
28 856 Philippines: K-Ar ages, SO<sub>3</sub> Contents of microphenocrystic apatite and significance of  
29 857 intrusive rocks: *Resource Geology*, v. 52, p. 147–161.
- 30  
31 858 Jago, C. P., Tosdal, R. M., Cooke, D. R., and Harris, A. C., 2014, Vertical and lateral  
32 859 variation of mineralogy and chemistry in the Early Jurassic Mt. Milligan alkalic  
33 860 porphyry Au-Cu deposit, British Columbia, Canada: *Economic Geology*, v. 109, p.  
34 861 1005–1033.
- 35  
36 862 Jugo, P. J., Luth, R. W., and Richards, J. P., 2005, Experimental data on the speciation of  
37 863 sulfur as a function of oxygen fugacity in basaltic melts: *Geochimica et*  
38 864 *Cosmochimica Acta*, v. 69, p. 497–503.
- 39  
40 865 Jugo, P. J., 2009, Sulfur content at sulfide saturation in oxidized magmas: *Geology*, v. 37,  
41 866 p. 415–418.
- 42  
43 867 Keith, J., Whitney, J., Hattori, K., Ballantyne, G., Christiansen, E., Barr, D., Cannan, T.,  
44 868 and Hook, C., 1997, The role of magmatic sulfides and mafic alkaline magmas in the  
45 869 Bingham and Tintic mining districts, Utah: *Journal of Petrology*, v. 38, p. 1679–1690.
- 46  
47 870 Konecke, B. A., Fiege, A., Simon, A. C., and Holtz, F., 2017a, Cryptic metasomatism  
48 871 during late-stage lunar magmatism implicated by sulfur in apatite: *Geology*, p. 739–  
49 872 742.
- 50  
51 873 Konecke, B. A., Fiege, A., Simon, A. C., Parat, F., and Stechern, A., 2017b, Co-  
52 874 variability of S<sup>6+</sup>, S<sup>4+</sup>, and S<sup>2-</sup> in apatite as a function of oxidation state: Implications  
53 875 for a new oxybarometer: *American Mineralogist*, v. 102, p. 548–557.
- 54  
55  
56  
57  
58  
59  
60  
61  
62  
63  
64  
65

- 1  
2  
3  
4 876 Lang, J. R., Lueck, B., Mortensen, J. K., Russell, J. K., Stanley, C. R., and Thompson, J.  
5 877 F., 1995, Triassic-Jurassic silica-undersaturated and silica-saturated alkalic intrusions  
6 878 in the Cordillera of British Columbia: Implications for arc magmatism: *Geology*, v. 23,  
7 879 p. 451–454.
- 10 880 Lange, R. A., Frey, H. M., and Hector, J., 2009, A thermodynamic model for the  
11 881 plagioclase-liquid hygrometer/thermometer: *American Mineralogist*, v. 94, p. 494–506.
- 13 882 Large, S.J.E., von Quadt, A., Wotzlaw, J.-F., Guillong, M., and Heinrich, C.A., 2018,  
14 883 Magma evolution leading to porphyry Au-Cu mineralization at the Ok Tedi Deposit,  
15 884 Papua New Guinea: trace element geochemistry and high-precision geochronology of  
16 885 igneous zircon: *Economic Geology*, v. 113, p. 39–61.
- 18 886 Larocque, A. C., Stimac, J. A., Keith, J. D., and Huminicki, M. A., 2000, Evidence for  
19 887 open-system behavior in immiscible Fe–S–O liquids in silicate magmas: implications  
20 888 for contributions of metals and sulfur to ore-forming fluids: *The Canadian*  
21 889 *Mineralogist*, v. 38, p. 1233–1249.
- 23 890 Li, J., Li, G., Qin, K., Xiao, B., Chen, L., and Zhao, J., 2012, Mineralogy and mineral  
24 891 chemistry of the Cretaceous Duolong gold-rich porphyry copper deposit in the  
25 892 Bangongco arc, northern Tibet: *Resource Geology*, v. 62, p. 19–41.
- 27 893 Li, Y., Selby, D., Feely, M., Costanzo, A., and Li, X.-H., 2017, Fluid inclusion  
28 894 characteristics and molybdenite Re-Os geochronology of the Qulong porphyry copper-  
29 895 molybdenum deposit, Tibet: *Mineralium Deposita*, v.52, p. 137–158.
- 31 896 Liang, H.-Y., Campbell, I. H., Allen, C., Sun, W.-D., Liu, C.-Q., Yu, H.-X., Xie, Y.-W.,  
32 897 and Zhang, Y.-Q., 2006, Zircon  $Ce^{4+}/Ce^{3+}$  ratios and ages for Yulong ore-bearing  
33 898 porphyries in eastern Tibet: *Mineralium Deposita*, v. 41, p. 152–159.
- 35 899 Loader, M. A., Wilkinson, J. J., and Armstrong, R. N., 2017, The effect of titanite  
36 900 crystallisation on Eu and Ce anomalies in zircon and its implications for the  
37 901 assessment of porphyry Cu deposit fertility: *Earth and Planetary Science Letters*, v.  
38 902 472, p. 107–119.
- 40 903 Loucks, R.R., 2013, Distinctive composition and genesis of copper ore-forming arc  
41 904 magmas: *Goldschmidt Conference 2013 Abstracts: Mineralogical Magazine*, v. 77, p.  
42 905 1642.
- 44 906 Locock, A. J., 2014, An Excel spreadsheet to classify chemical analyses of amphiboles  
45 907 following the IMA 2012 recommendations: *Computers & Geosciences*, v. 62, p. 1–11.
- 47 908 Logan, J. M., and Mihalynuk, M. G., 2014, Tectonic controls on Early Mesozoic paired  
48 909 alkaline porphyry deposit belts (Cu-Au ± Ag-Pt-Pd-Mo) within the Canadian  
49 910 Cordillera: *Economic Geology*, v. 109, p. 827–858.
- 51 911 Loucks, R., 2014, Distinctive composition of copper-ore-forming arc magmas: *Australian*  
52 912 *Journal of Earth Sciences*, v. 61, p. 5–16.

1  
2  
3  
4  
5  
6  
7  
8  
9  
10  
11  
12  
13  
14  
15  
16  
17  
18  
19  
20  
21  
22  
23  
24  
25  
26  
27  
28  
29  
30  
31  
32  
33  
34  
35  
36  
37  
38  
39  
40  
41  
42  
43  
44  
45  
46  
47  
48  
49  
50  
51  
52  
53  
54  
55  
56  
57  
58  
59  
60  
61  
62  
63  
64  
65

913 Lowell, J. D., and Guilbert, J. M., 1970, Lateral and vertical alteration-mineralization  
914 zoning in porphyry ore deposits: *Economic Geology*, v. 65, p. 373–408.

915 Lu, Y.-J., Loucks, R. R., Fiorentini, M. L., Yang, Z.-M., and Hou, Z.-Q., 2015, Fluid flux  
916 melting generated postcollisional high Sr/Y copper ore-forming water-rich magmas in  
917 Tibet: *Geology*, v.43, p. 583–586.

918 Lu, Y.-J., Loucks, R. R., Fiorentini, M., McCuaig, T. C., Evans, N. J., Yang, Z.-M., Hou,  
919 Z.-Q., Kirkland, C. L., Parra-Avila, L. A., and Kobussen, A., 2016, Zircon  
920 compositions as a pathfinder for Cu±Mo±Au deposits: *Society of Economic  
921 Geologists Special Publication*, v. 19, p. 329–347.

922 Mao, M., Rukhlov, A. S., Rowins, S. M., Spence, J., and Coogan, L. A., 2016, Apatite  
923 trace element compositions: A robust new tool for mineral exploration: *Economic  
924 Geology*, v. 111, p. 1187–1222.

925 Marsden, H., and Thorkelson, D. J., 1992, Geology of the Hazelton volcanic belt in  
926 British Columbia: implications for the Early to Middle Jurassic evolution of Stikinia:  
927 *Tectonics*, v. 11, p. 1266–1287.

928 Masterman, G. J., Cooke, D. R., Berry, R. F., Clark, A. H., Archibald, D. A., Mathur, R.,  
929 Walshe, J. L., and Durán, M., 2004, <sup>40</sup>Ar/<sup>39</sup>Ar and Re-Os geochronology of porphyry  
930 copper-molybdenum deposits and related copper-silver veins in the Collahuasi district,  
931 northern Chile: *Economic Geology*, v. 99, p. 673–690.

932 Mathez, E. A., 1973, Refinement of the Kudo-Weill plagioclase thermometer and its  
933 application to basaltic rocks: *Contributions to Mineralogy and Petrology*, v. 41, p. 61–  
934 72.

935 Mathez, E.A., 1984, Influence of degassing on oxidation-states of basaltic magmas:  
936 *Nature*, v. 310, p. 371–375.

937 Mathez, E. A., and Webster, J. D., 2005, Partitioning behavior of chlorine and fluorine in  
938 the system apatite-silicate melt-fluid: *Geochimica et Cosmochimica Acta*, v. 69, p.  
939 1275–1286.

940 Matzel, J. E., Bowring, S. A., and Miller, R. B., 2006, Time scales of pluton construction  
941 at differing crustal levels: Examples from the Mount Stuart and Tenpeak intrusions,  
942 North Cascades, Washington: *Geological Society of America Bulletin*, v. 118, p.  
943 1412–1430.

944 McMillan, W.J., Thompson, J.F.H., Hart, C.J.R., and Johnston, S.T., 1995, Regional  
945 geological and tectonic setting of porphyry deposits in British Columbia and Yukon  
946 Territory: *Canadian Institute of Mining, Metallurgy and Petroleum Special Volume 46*,  
947 p. 40–57.

948 Merzbacher, C., and Eggler, D.H., 1984, A magmatic geohygrometer: Application to  
949 Mount St. Helens and other dacitic magmas: *Geology*, v. 12, p. 587–590.

1  
2  
3  
4  
5  
6  
7  
8  
9  
10  
11  
12  
13  
14  
15  
16  
17  
18  
19  
20  
21  
22  
23  
24  
25  
26  
27  
28  
29  
30  
31  
32  
33  
34  
35  
36  
37  
38  
39  
40  
41  
42  
43  
44  
45  
46  
47  
48  
49  
50  
51  
52  
53  
54  
55  
56  
57  
58  
59  
60  
61  
62  
63  
64  
65

950 Micko, J., Tosdal, R. M., Bissig, T., Chamberlain, C. M., and Simpson, K. A., 2014,  
951 Hydrothermal alteration and mineralization of the Galore Creek alkalic Cu-Au  
952 porphyry deposit, northwestern British Columbia, Canada: *Economic Geology*, v. 109,  
953 p. 891–914.

954 Mihalyuk, M., Erdmer, P., Ghent, E., Cordey, F., Archibald, D., Friedman, R., and  
955 Johannson, G., 2004, Coherent French Range blueschist: Subduction to exhumation  
956 in < 2.5 my?: *Geological Society of America Bulletin*, v. 116, p. 910–922.

957 Monger, J. W. H., and Irving, E., 1980, Northward displacement of north-central British  
958 Columbia: *Nature*, v. 285, p. 289–294.

959 Moore, G., and Carmichael, I., 1998, The hydrous phase equilibria (to 3 kbar) of an  
960 andesite and basaltic andesite from western Mexico: constraints on water content and  
961 conditions of phenocryst growth: *Contributions to Mineralogy and Petrology*, v. 130, p.  
962 304–319.

963 Mortensen, J.K., Ghosh, D.K., and Ferri, F., 1995, U-Pb geochronology of intrusive rocks  
964 associated with copper-gold porphyry deposits in the Canadian Cordillera: *Canadian  
965 Institute of Mining, Metallurgy and Petroleum, Special Volume 46*, p. 142–158.

966 Mutch, E., Blundy, J., Tattitch, B., Cooper, F., and Brooker, R., 2016, An experimental  
967 study of amphibole stability in low-pressure granitic magmas and a revised Al-in-  
968 hornblende geobarometer: *Contributions to Mineralogy and Petrology*, v. 171, 85, doi:  
969 10.1007/s00410-016-1298-9

970 Myers, J. t., and Eugster, H., 1983, The system Fe-Si-O: Oxygen buffer calibrations to  
971 1,500 K: *Contributions to Mineralogy and Petrology*, v. 82, p. 75–90.

972 Nadeau, O., Williams-Jones, A. E., and Stix, J., 2010, Sulphide magma as a source of  
973 metals in arc-related magmatic hydrothermal ore fluids: *Nature Geoscience*, v. 3, p.  
974 501–505.

975 Nadeau, O., Stix, J., and Williams-Jones, A. E., 2016, Links between arc volcanoes and  
976 porphyry-epithermal ore deposits: *Geology*, v. 44, p. 11–14.

977 Naney, M. T., 1983, Phase equilibria of rock-forming ferromagnesian silicates in granitic  
978 systems: *American Journal of Science*, v. 283, p. 993–1033.

979 Nelson, J., and Colpron, M., 2007, Tectonics and metallogeny of the British Columbia,  
980 Yukon and Alaskan Cordillera, 1.8 Ga to the present: *Mineral deposits of Canada: a  
981 synthesis of major deposit-types, district metallogeny, the evolution of geological  
982 provinces, and exploration methods: Geological Association of Canada, Mineral  
983 Deposits Division, Special Publication*, v. 5, p. 755–791.

984 Nelson, J., Colpron, M., and Israel, S., 2013, The Cordillera of British Columbia, Yukon,  
985 and Alaska: Tectonics and metallogeny: *Society of Economic Geologists Special  
986 Publication*, v. 17, p. 53–109.

1  
2  
3  
4  
5  
6  
7  
8  
9  
10  
11  
12  
13  
14  
15  
16  
17  
18  
19  
20  
21  
22  
23  
24  
25  
26  
27  
28  
29  
30  
31  
32  
33  
34  
35  
36  
37  
38  
39  
40  
41  
42  
43  
44  
45  
46  
47  
48  
49  
50  
51  
52  
53  
54  
55  
56  
57  
58  
59  
60  
61  
62  
63  
64  
65

987 Newell, J.M., and Peatfield, G.R., 1995, The Red Chris porphyry copper-gold deposit:  
988 Canadian Institute of Mining and Metallurgy Special Volume 46,  
989 p. 674–688.

990 Norris, J.R., 2012, Evolution of alteration and mineralization at the Red Chris Cu-Au  
991 porphyry deposit East zone, northwestern British Columbia, Canada: M.Sc. thesis,  
992 Vancouver, Canada, University of British Columbia, 194 p.

993 Pan, L.-C., Hu, R.-Z., Wang, X.-S., Bi, X.-W., Zhu, J.-J., and Li, C., 2016, Apatite trace  
994 element and halogen compositions as petrogenetic-metallogenic indicators: Examples  
995 from four granite plutons in the Sanjiang region, SW China: *Lithos*, v. 254–255, p.  
996 118–130.

997 Parat, F., and Holtz, F., 2005, Sulfur partition coefficient between apatite and rhyolite:  
998 the role of bulk S content: *Contributions to Mineralogy and Petrology*, v. 150, p. 643–  
999 651.

1000 Parat, F., Holtz, F., and Klügel, A., 2011, S-rich apatite-hosted glass inclusions in  
1001 xenoliths from La Palma: constraints on the volatile partitioning in evolved alkaline  
1002 magmas: *Contributions to Mineralogy and Petrology*, v. 162, p. 463–478.

1003 Pass, H. E., Cooke, D. R., Davidson, G., Maas, R., Dipple, G., Rees, C., Ferreira, L.,  
1004 Taylor, C., and Deyell, C. L., 2014, Isotope geochemistry of the northeast zone,  
1005 Mount Polley alkalic Cu-Au-Ag porphyry deposit, British Columbia: A case for  
1006 carbonate assimilation: *Economic Geology*, v. 109, p. 859–890.

1007 Patchett, P., Gehrels, G. E., and Isachsen, C., 1998, Nd isotopic characteristics of  
1008 metamorphic and plutonic rocks of the Coast Mountains near Prince Rupert, British  
1009 Columbia: *Canadian Journal of Earth Sciences*, v. 35, p. 556–561.

1010 Paterson, S. R., Okaya, D., Memeti, V., Economos, R., and Miller, R. B., 2011, Magma  
1011 addition and flux calculations of incrementally constructed magma chambers in  
1012 continental margin arcs: Combined field, geochronologic, and thermal modeling  
1013 studies: *Geosphere*, v. 7, p. 1439–1468.

1014 Pearce, T. H., and Kolisnik, A. M., 1990, Observations of plagioclase zoning using  
1015 interference imaging: *Earth-Science Reviews*, v. 29, p. 9–26.

1016 Pearce, J., 1996, Sources and settings of granitic rocks: *Episodes*, v. 19, p. 120–125.

1017 Peng, G., Luhr, J. F., and McGee, J. J., 1997, Factors controlling sulfur concentrations in  
1018 volcanic apatite: *American Mineralogist*, v. 82, p. 1210–1224.

1019 Piccoli, P., and Candela, P., 1994, Apatite in felsic rocks; a model for the estimation of  
1020 initial halogen concentrations in the Bishop Tuff (Long Valley) and Tuolumne  
1021 Intrusive Suite (Sierra Nevada Batholith) magmas: *American Journal of Science*, v.  
1022 294, p. 92–135.

- 1  
2  
3  
4 1023 Piccoli, P. M., and Candela, P. A., 2002, Apatite in igneous systems: Reviews in  
5  
6 1024 Mineralogy and Geochemistry, v. 48, p. 255–292.  
7  
8 1025 Pilet, S., Baker, M. B., Müntener, O., and Stolper, E. M., 2011, Monte Carlo simulations  
9  
10 1026 of metasomatic enrichment in the lithosphere and implications for the source of  
11  
12 1027 alkaline basalts: *Journal of Petrology*, v. 52, p. 1415–1442.  
13  
14 1028 Qiu, J.-T., Li, P.-J., Santosh, M., and Yu, X.-Q., 2014, Magma oxygen fugacities of  
15  
16 1029 granitoids in the Xiaoqinling area, central China: implications for regional tectonic  
17  
18 1030 setting: *Neues Jahrbuch für Mineralogie-Abhandlungen (Journal of Mineralogy and  
19  
20 1031 Geochemistry)*, v. 191, p. 317–329.  
21  
22 1032 Rees, C., Riedell, K. B., Proffett, J. M., Macpherson, J., and Robertson, S., 2015, The  
23  
24 1033 Red Chris porphyry copper-gold deposit, Northern British Columbia, Canada: Igneous  
25  
26 1034 phases, alteration, and controls of mineralization: *Economic Geology*, v. 110, p. 857–  
27  
28 1035 888.  
29  
30 1036 Rezeau, H., Moritz, R., Wotzlaw, J.-F., Tayan, R., Melkonyan, R., Ulianov, A., Selby, D.,  
31  
32 1037 d’Abzac, F.-X., and Stern, R. A., 2016, Temporal and genetic link between  
33  
34 1038 incremental pluton assembly and pulsed porphyry Cu-Mo formation in accretionary  
35  
36 1039 orogens: *Geology*, v. 44, p. 627–630.  
37  
38 1040 Richards, J. P., 2003, Tectono-magmatic precursors for porphyry Cu-(Mo-Au) deposit  
39  
40 1041 formation: *Economic Geology*, v. 98, p. 1515–1533.  
41  
42 1042 Richards, J. P., 2009, Postsubduction porphyry Cu-Au and epithermal Au deposits:  
43  
44 1043 Products of remelting of subduction-modified lithosphere: *Geology*, v. 37, p. 247–250.  
45  
46 1044 Richards, J.P., 2011, Magmatic to hydrothermal metal fluxes in convergent and collided  
47  
48 1045 margins: *Ore Geology Reviews*, v. 40, p. 1–26.  
49  
50 1046 Richards, J. P., 2015, The oxidation state, and sulfur and Cu contents of arc magmas:  
51  
52 1047 implications for metallogeny: *Lithos*, v. 233, p. 27–45.  
53  
54 1048 Richards, J. P., and Kerrich, R., 2007, Special Paper: Adakite-like rocks: their diverse  
55  
56 1049 origins and questionable role in metallogenesis: *Economic Geology*, v. 102, p. 537–  
57  
58 1050 576.  
59  
60 1051 Richards, J. P., López, G. P., Zhu, J.-J., Creaser, R. A., Locock, A. J., and Mumin, A. H.,  
61  
62 1052 2017, Contrasting tectonic settings and sulfur contents of magmas associated with  
63  
64 1053 Cretaceous porphyry Cu ± Mo ± Au and intrusion-related iron oxide Cu-Au deposits  
65  
1054 in northern Chile: *Economic Geology*, v. 112, p. 295–318.  
1055  
1056 Ricketts, B. D., Evenchick, C. A., Anderson, R. G., and Murphy, D. C., 1992, Bowser  
1057 basin, northern British Columbia: Constraints on the timing of initial subsidence and  
1058 Stikinia-North America terrane interactions: *Geology*, v. 20, p. 1119–1122.  
1059  
1060  
1061  
1062  
1063  
1064  
1065

- 1  
2  
3  
4 1060 and application to subduction-related volcanoes: *Contributions to Mineralogy and*  
5  
6 1061 *Petrology*, v. 160, p. 45–66.
- 7 1062 Rohrlach, B.D., and Loucks, R.R., 2005, Multi-million-year cyclic ramp-up of volatiles  
8  
9 1063 in a lower crustal magma reservoir trapped below the Tampakan copper-gold deposit  
10 1064 by Mio-Pliocene crustal compression in the southern Philippines, *in* Porter, T.M., ed.,  
11 1065 *Super porphyry copper and gold deposits: A global perspective*: PGC Publishing,  
12 1066 Adelaide, South Australia, v. 2, p. 369–407.
- 13  
14  
15 1067 Rutherford, M.J., and Devine, J.D., 1988, The May 18, 1980, eruption of Mount St.  
16 1068 Helens. 3. Stability and chemistry of amphibole in the magma chamber: *Journal of*  
17 1069 *Geophysical Research*, v. 93, p. 11,949–11,959.
- 18  
19 1070 Rutherford, M. J., and Devine, J. D., 2003, Magmatic conditions and magma ascent as  
20 1071 indicated by hornblende phase equilibria and reactions in the 1995–2002 Soufriere  
21 1072 Hills magma: *Journal of Petrology*, v. 44, p. 1433–1453.
- 22  
23 1073 Samson, S. D., McClelland, W. C., Patchett, P. J., Gehrels, G. E., and Anderson, R. G.,  
24 1074 1989, Evidence from neodymium isotopes for mantle contributions to Phanerozoic  
25 1075 crustal genesis in the Canadian Cordillera: *Nature*, v. 337, p. 705–709.
- 26  
27 1076 Samson, S. D., Patchett, P. J., McClelland, W. C., and Gehrels, G. E., 1991, Nd and Sr  
28 1077 isotopic constraints on the petrogenesis of the west side of the northern Coast  
29 1078 Mountains batholith, Alaskan and Canadian Cordillera: *Canadian Journal of Earth*  
30 1079 *Sciences*, v. 28, p. 939–946.
- 31  
32 1080 Schaltegger, U., Brack, P., Ovtcharova, M., Peytcheva, I., Schoene, B., Stracke, A.,  
33 1081 Marocchi, M., and Bargossi, G. M., 2009, Zircon and titanite recording 1.5 million  
34 1082 years of magma accretion, crystallization and initial cooling in a composite pluton  
35 1083 (southern Adamello batholith, northern Italy): *Earth and Planetary Science Letters*, v.  
36 1084 286, p. 208–218.
- 37  
38 1085 Scott, J.E., Richards, J.P., Heaman, L.M., Creaser, R.A., and Salazar, G.S., 2008, The  
39 1086 Schaft Creek porphyry Cu-Mo-(Au) deposit, Northwestern British Columbia:  
40 1087 *Exploration and Mining Geology*, v. 17, p. 163–196.
- 41  
42 1088 Seedorff, E., Dilles, J., Proffett, J., Einaudi, M., Zurcher, L., Stavast, W., Johnson, D.,  
43 1089 and Barton, M., 2005, Porphyry deposits: Characteristics and origin of hypogene  
44 1090 features: *Economic Geology 100th anniversary volume*, v. 29, p. 251–298.
- 45  
46 1091 Selby, D., and Creaser, R. A., 2004, Macroscale NTIMS and microscale LA-MC-ICP-  
47 1092 MS Re-Os isotopic analysis of molybdenite: Testing spatial restrictions for reliable  
48 1093 Re-Os age determinations, and implications for the decoupling of Re and Os within  
49 1094 molybdenite: *Geochimica et Cosmochimica Acta*, v. 68, p. 3897–3908.
- 50  
51 1095 Shen, P., Hattori, K., Pan, H., Jackson, S., and Seitmuratova, E., 2015, Oxidation  
52 1096 condition and metal fertility of granitic magmas: zircon trace-element data from  
53  
54  
55  
56  
57  
58  
59  
60  
61  
62  
63  
64  
65



1  
2  
3  
4  
5  
6  
7  
8  
9  
10  
11  
12  
13  
14  
15  
16  
17  
18  
19  
20  
21  
22  
23  
24  
25  
26  
27  
28  
29  
30  
31  
32  
33  
34  
35  
36  
37  
38  
39  
40  
41  
42  
43  
44  
45  
46  
47  
48  
49  
50  
51  
52  
53  
54  
55  
56  
57  
58  
59  
60  
61  
62  
63  
64  
65

1097 porphyry Cu deposits in the Central Asian Orogenic Belt: *Economic Geology*, v. 110,  
1098 p. 1861–1878.

1099 Sillitoe, R., 2010, Porphyry copper systems: *Economic Geology*, v. 105, p. 3–41.

1100 Simon, A. C., and Ripley, E. M., 2011, The role of magmatic sulfur in the formation of  
1101 ore deposits: *Reviews in Mineralogy and Geochemistry*, v. 73, p. 513–578.

1102 Steinberger, I., Hinks, D., Driesner, T., and Heinrich, C.A., 2013, Source plutons driving  
1103 porphyry copper ore formation: combining geomagnetic data, thermal constraints, and  
1104 chemical mass balance to quantify the magma chamber beneath the Bingham Canyon  
1105 deposit: *Economic Geology*, v. 108, p. 605–624.

1106 Stern, C. R., Funk, J. A., Skewes, M. A., and Arévalo, A., 2007, Magmatic anhydrite in  
1107 plutonic rocks at the El Teniente Cu-Mo deposit, Chile, and the role of sulfur-and  
1108 copper-rich magmas in its formation: *Economic geology*, v. 102, p. 1335–1344.

1109 Stock, M. J., Humphreys, M. C. S., Smith, V. C., Isaia, R., and Pyle, D. M., 2016, Late-  
1110 stage volatile saturation as a potential trigger for explosive volcanic eruptions: *Nature*  
1111 *Geosciences*, v. 9, p. 249–254.

1112 Streck, M. J., and Dilles, J. H., 1998, Sulfur evolution of oxidized arc magmas as  
1113 recorded in apatite from a porphyry copper batholith: *Geology*, v. 26, p. 523–526.

1114 Sun, S.-S., and McDonough, W., 1989, Chemical and isotopic systematics of oceanic  
1115 basalts: implications for mantle composition and processes: *Geological Society*,  
1116 London, Special Publications, v. 42, p. 313–345.

1117 Tapster, S., Condon, D., Naden, J., Noble, S., Petterson, M., Roberts, N., Saunders, A.,  
1118 and Smith, D. J., 2016, Rapid thermal rejuvenation of high-crystallinity magma linked  
1119 to porphyry copper deposit formation; evidence from the Koloula Porphyry Prospect,  
1120 Solomon Islands: *Earth and Planetary Science Letters*, v. 442, p. 206–217.

1121 Taseko Mines Limited, 2013, Gibraltar reserves and resources at December 31, 2012:  
1122 Taseko Mines Limited Report, [www.tasekomines.com/gibraltar/ID540174](http://www.tasekomines.com/gibraltar/ID540174).

1123 Titley, S.R., and Beane, R.E., 1981, Porphyry copper deposits, Part 1. Geologic settings,  
1124 petrology, and tectogenesis: *Economic Geology 75<sup>TH</sup> Anniversary Volume*, p. 214–  
1125 235.

1126 Trail, D., Watson, E. B., and Tailby, N. D., 2011, The oxidation state of Hadean magmas  
1127 and implications for early Earth/s atmosphere: *Nature*, v. 480, p. 79–82.

1128 Ustunisik, G., Kilinc, A., and Nielsen, R. L., 2014, New insights into the processes  
1129 controlling compositional zoning in plagioclase: *Lithos*, v. 200, p. 80–93.

1130 Von Quadt, A., Erni, M., Martinek, K., Moll, M., Peytcheva, I., and Heinrich, C. A., 2011,  
1131 Zircon crystallization and the lifetimes of ore-forming magmatic-hydrothermal  
1132 systems: *Geology*, v. 39, p. 731–734.

1  
2  
3  
4  
5  
6  
7  
8  
9  
10  
11  
12  
13  
14  
15  
16  
17  
18  
19  
20  
21  
22  
23  
24  
25  
26  
27  
28  
29  
30  
31  
32  
33  
34  
35  
36  
37  
38  
39  
40  
41  
42  
43  
44  
45  
46  
47  
48  
49  
50  
51  
52  
53  
54  
55  
56  
57  
58  
59  
60  
61  
62  
63  
64  
65

1133 Walker Jr, B. A., Miller, C. F., Lowery Claiborne, L., Wooden, J. L., and Miller, J. S.,  
1134 2007, Geology and geochronology of the Spirit Mountain batholith, southern Nevada:  
1135 Implications for timescales and physical processes of batholith construction: *Journal*  
1136 *of Volcanology and Geothermal Research*, v. 167, p. 239–262.

1137 Wallace, P. J., 2005, Volatiles in subduction zone magmas: concentrations and fluxes  
1138 based on melt inclusion and volcanic gas data: *Journal of Volcanology and*  
1139 *Geothermal Research*, v. 140, p. 217–240.

1140 Wang, R., Richards, J. P., Hou, Z., Yang, Z., and DuFrane, S. A., 2014a, Increased  
1141 magmatic water content—the key to Oligo-Miocene porphyry Cu-Mo ± Au formation  
1142 in the Eastern Gangdese Belt, Tibet: *Economic Geology*, v. 109, p. 1315–1339.

1143 Wang, R., Richards, J. P., Hou, Z.-q., Yang, Z.-m., Gou, Z.-b., and DuFrane, S. A., 2014b,  
1144 Increasing magmatic oxidation state from Paleocene to Miocene in the Eastern  
1145 Gangdese Belt, Tibet: Implication for collision-related porphyry Cu-Mo ± Au  
1146 mineralization: *Economic Geology*, v. 109, p. 1943–1965.

1147 Waters, L. E., and Lange, R. A., 2015, An updated calibration of the plagioclase-liquid  
1148 hygrometer-thermometer applicable to basalts through rhyolites: *American*  
1149 *Mineralogist*, v. 100, p. 2172–2184.

1150 Webster, J. D., 1997, Chloride solubility in felsic melts and the role of chloride in  
1151 magmatic degassing: *Journal of Petrology*, v. 38, p. 1793–1807.

1152 Webster, J. D., Kinzler, R. J., and Mathez, E. A., 1999, Chloride and water solubility in  
1153 basalt and andesite melts and implications for magmatic degassing: *Geochimica et*  
1154 *Cosmochimica Acta*, v. 63, p. 729–738.

1155 Webster, J. D., Tappen, C. M., and Mandeville, C. W., 2009, Partitioning behavior of  
1156 chlorine and fluorine in the system apatite–melt–fluid. II: Felsic silicate systems at 200  
1157 MPa: *Geochimica et Cosmochimica Acta*, v. 73, p. 559–581.

1158 Webster, J., Goldoff, B., Sintoni, M., Shimizu, N., and De Vivo, B., 2014, C–O–H–Cl–  
1159 S–F volatile solubilities, partitioning, and mixing in phonolitic–trachytic melts and  
1160 aqueous–carbonic vapor ± saline liquid at 200 MPa: *Journal of Petrology*, v. 55, p.  
1161 2217–2248.

1162 Webster, J. D., and Piccoli, P. M., 2015, Magmatic apatite: A powerful, yet deceptive,  
1163 mineral: *Elements*, v. 11, p. 177–182.

1164 Weis, P., Driesner, T., and Heinrich, C., 2012, Porphyry-copper ore shells form at stable  
1165 pressure-temperature fronts within dynamic fluid plumes: *Science*, v. 338, p. 1613–  
1166 1616.

1167 Wilkinson, J. J., 2013, Triggers for the formation of porphyry ore deposits in magmatic  
1168 arcs: *Nature Geoscience*, v. 6, p. 917–925.

1  
2  
3  
4  
5  
6  
7  
8  
9  
10  
11  
12  
13  
14  
15  
16  
17  
18  
19  
20  
21  
22  
23  
24  
25  
26  
27  
28  
29  
30  
31  
32  
33  
34  
35  
36  
37  
38  
39  
40  
41  
42  
43  
44  
45  
46  
47  
48  
49  
50  
51  
52  
53  
54  
55  
56  
57  
58  
59  
60  
61  
62  
63  
64  
65

1169 Winchester, J.A., and Floyd, P.A., 1977, Geochemical discrimination of different magma  
1170 series and their differentiation products using immobile elements: *Chemical Geology*,  
1171 v. 20, p. 325–343.

1172 Xu, L., Bi, X., Hu, R., Qi, Y., Tang, Y., Wang, X., and Zhu, J., 2016, Redox states and  
1173 genesis of magmas associated with intra-continental porphyry Cu–Au mineralization  
1174 within the Jinshajiang–Red River alkaline igneous belt, SW China: *Ore Geology*  
1175 *Reviews*, v. 73, Part 2, p. 330–345.

1176 Yang, Z., Hou, Z., White, N. C., Chang, Z., Li, Z., and Song, Y., 2009, Geology of the  
1177 post-collisional porphyry copper–molybdenum deposit at Qulong, Tibet: *Ore Geology*  
1178 *Reviews*, v. 36, p. 133–159.

1179 Zajacz, Z., Seo, J.H., Candela, P.A., Piccoli, P.M., and Tossell, J.A., 2011, The solubility  
1180 of copper in high-temperature magmatic vapors: A quest for the significance of  
1181 various chloride and sulfide complexes: *Geochimica et Cosmochimica Acta*, v. 75, p.  
1182 2811–2827.

1183 Zajacz, Z., Candela, P.A., Piccoli, P.M., Wälle, M., and Sanchez-Valle, C., 2012, Gold  
1184 and copper in volatile saturated mafic to intermediate magmas: Solubilities,  
1185 partitioning, and implications for ore deposit formation: *Geochimica et Cosmochimica*  
1186 *Acta*, v. 91, p. 140–159.

1187 Zhang, C., Holtz, F., Ma, C., Wolff, P. E., and Li, X., 2012, Tracing the evolution and  
1188 distribution of F and Cl in plutonic systems from volatile-bearing minerals: a case  
1189 study from the Liujiawa pluton (Dabie orogen, China): *Contributions to Mineralogy*  
1190 *and Petrology*, v. 164, p. 859–879.

1191 Zhang, D., and Audétat, A., 2017, What caused the formation of the giant Bingham  
1192 Canyon porphyry Cu-Mo-Au deposit? Insights from melt Inclusions and magmatic  
1193 sulfides: *Economic Geology*, v. 112, p. 221–244.

1194 Zimmer, M.M., Plank, T., Hauri, E.H., Yogodzinski, G.M., Stelling, P., Larsen, J., Singer,  
1195 B., Jicha, B., Mandeville, C., and Nye, C.J., 2010, The role of water in generating the  
1196 calc-alkaline trend: New volatile data for Aleutian magmas and a new Tholeiitic Index:  
1197 *Journal of Petrology*, v. 51, p. 2411–2444.

1198 Zhu, C., and Sverjensky, D. A., 1991, Partitioning of F-Cl-OH between minerals and  
1199 hydrothermal fluids: *Geochimica et Cosmochimica Acta*, v. 55, p. 1837–1858.

1  
2  
3  
4  
5  
6  
7  
8  
9  
10  
11  
12  
13  
14  
15  
16  
17  
18  
19  
20  
21  
22  
23  
24  
25  
26  
27  
28  
29  
30  
31  
32  
33  
34  
35  
36  
37  
38  
39  
40  
41  
42  
43  
44  
45  
46  
47  
48  
49  
50  
51  
52  
53  
54  
55  
56  
57  
58  
59  
60  
61  
62  
63  
64  
65

**1200 Figure Captions**

1201 Fig. 1. Major terranes in the south of the Canadian Cordillera, showing Triassic to  
1202 Jurassic magmatic belts and major associated porphyry deposits in the Stikine and  
1203 Quesnel terranes (modified from Nelson and Colpron, 2007; Nelson et al., 2013; original  
1204 graphics file provided by Joanne Nelson, British Columbia Geological Survey of Canada).  
1205 The age of the Red Chris deposit is from this study (Table 1), and the ages for the other  
1206 porphyry deposits are from Brown and Kahlert (1986; Red Mountain), Mortensen et al.  
1207 (1995; Mt. Polley), Scott et al. (2008; Schaft Creek), Duuring et al. (2009; Kemess  
1208 South), Taseko Mines Limited (2013; Gibraltar), Bath et al. (2014; Lorraine), Byrne and  
1209 Tosdal (2014; Galore Creek), Devine et al. (2014; Lorraine), Logan and Mihalynuk (2014;  
1210 Highland Valley, Copper Mountaine, Afton/Ajax, and Brenda), and Jago et al. (2014; Mt.  
1211 Milligan).

1212  
1213 Fig. 2. Simplified geological map of the Red Stock and Red Chris Cu-Au deposit,  
1214 showing the main mineralized zoned (named) and the locations of sampled drill holes  
1215 (modified from Rees et al., 2015). Universal Transverse Mercator coordinates are based  
1216 on the WGS84 datum.

1217  
1218 Fig. 3. Hand specimen photographs of samples of the P1, P2E, P2L, and P3 porphyry  
1219 intrusions, and two late basaltic to andesitic dikes. (A) P1 porphyry with anhedral to  
1220 subhedral altered amphibole and plagioclase phenocrysts, crosscut by pyrite-quartz veins  
1221 (sample RC13-35). (B) P2E porphyry showing crowded texture with chloritized  
1222 amphibole and plagioclase phenocrysts; plagioclase grains are rimmed or replaced by

1  
2  
3  
4  
5  
6  
7  
8  
9  
10  
11  
12  
13  
14  
15  
16  
17  
18  
19  
20  
21  
22  
23  
24  
25  
26  
27  
28  
29  
30  
31  
32  
33  
34  
35  
36  
37  
38  
39  
40  
41  
42  
43  
44  
45  
46  
47  
48  
49  
50  
51  
52  
53  
54  
55  
56  
57  
58  
59  
60  
61  
62  
63  
64  
65

1223 secondary K-feldspar. The brick-red color is due to fine-grained hematite (sample RC13-  
1224 107). (C) P2L porphyry composed of abundant fresh amphibole and plagioclase  
1225 phenocrysts, with quartz in the groundmass (sample RC13-32). (D) The P3 porphyry is  
1226 similar to P2L, but is distinguished by the absence of quartz in the groundmass (sample  
1227 RC13-78). (E) Andesitic dike with anhedral to subhedral amphibole phenocrysts, crosscut  
1228 by a small calcite vein (sample RC13-62). (F) Basaltic dike with chloritized amphibole  
1229 phenocrysts (sample RC13-106). See Digital Appendix Table A1 for sample locations.

1230

1231 Fig. 4. West-southwest–east-northeast cross section A–A’, and north-northwest–south-  
1232 southwest cross section B–B’ (location of sections shown in Fig. 2), modified from  
1233 Gillstrom et al. (2012) and Rees et al. (2015). Copper equivalent-grade zones, drill holes,  
1234 and the boundary between potassic and post-potassic zones are shown: Cu equivalent (%)  
1235 =  $\text{Cu (\%)} + 0.486 \times \text{Au (g/t)}$ .

1236

1237 Fig. 5. Hand specimen photographs and photomicrographs of alteration and vein minerals.  
1238 (A, B) P2E porphyry (samples RC13-81 and RC13-75) with potassic alteration and A-  
1239 type quartz veins comprising magnetite, secondary K-feldspar, and disseminated bornite  
1240 and pyrite. Potassic alteration is characterized by secondary K-feldspar veins and  
1241 selvages around A-veins. Late unmineralized carbonate veins cut the A veins. (C)  
1242 Amphibole phenocryst altered to secondary biotite, which has then been altered to  
1243 chlorite, reflecting potassic alteration overprinted by chlorite–sericite alteration (plane-  
1244 polarized transmitted light; P2E: sample RC13-30). (D) Plagioclase phenocryst partially  
1245 overprinted by sericite (cross-polarized transmitted light; P2E porphyry: sample RC13-

1  
2  
3  
4  
5  
6  
7  
8  
9  
10  
11  
12  
13  
14  
15  
16  
17  
18  
19  
20  
21  
22  
23  
24  
25  
26  
27  
28  
29  
30  
31  
32  
33  
34  
35  
36  
37  
38  
39  
40  
41  
42  
43  
44  
45  
46  
47  
48  
49  
50  
51  
52  
53  
54  
55  
56  
57  
58  
59  
60  
61  
62  
63  
64  
65

1246 11). (E) B-type quartz veins with centerline pyrite in P2L porphyry (sample RC13-44). (F)  
1247 Pyritic D vein in P1 porphyry (sample RC13-40). (G) High-grade ore in sheeted A-type  
1248 quartz-chalcopyrite-K-feldspar veins (sample RC13-31 in P2E porphyry). (H) Quartz-  
1249 carbonate-pyrite-molybdenite-chalcopyrite vein in P2E porphyry (reflected light; sample  
1250 RC13-88). Abbreviations: Amp = amphibole; Bi = biotite; Bn = bornite; Cbn = carbonate;  
1251 Chl = chlorite; Cpy = chalcopyrite; Kfs = K-feldspar; Mo = molybdenite; Mt = magnetite;  
1252 Pl = plagioclase; Py = pyrite; Qtz = quartz. See Digital Appendix Table A1 for sample  
1253 locations.

1254  
1255 Fig. 6. Zircon U–Pb Tera-Wasserburg concordia diagrams for (A) P1, (B) P2E, (C) P2L,  
1256 and (D) P3 porphyry samples dated by LA-MC-ICP-MS. Uncertainty ellipses and  
1257 calculated ages are shown at  $2\sigma$ .

1258  
1259 Fig. 7. Weighted mean Re-Os model age of three molybdenite vein samples from the Red  
1260 Chris Cu-Au deposit.

1261  
1262 Fig. 8. Zr/Ti vs. Nb/Y discrimination diagram (Winchester and Floyd, 1977) for porphyry  
1263 and basaltic–andesitic dike samples from Red Chris.

1264  
1265 Fig. 9. Selected whole-rock major element variation diagrams for porphyry and basaltic–  
1266 andesitic dike samples from Red Chris: (A) K<sub>2</sub>O, (B) Na<sub>2</sub>O, (C) TiO<sub>2</sub>, (D) Al<sub>2</sub>O<sub>3</sub>, (E)  
1267 total Fe<sub>2</sub>O<sub>3</sub>, and (F) MgO vs. SiO<sub>2</sub>.

1268

1  
2  
3  
4  
5  
6  
7  
8  
9  
10  
11  
12  
13  
14  
15  
16  
17  
18  
19  
20  
21  
22  
23  
24  
25  
26  
27  
28  
29  
30  
31  
32  
33  
34  
35  
36  
37  
38  
39  
40  
41  
42  
43  
44  
45  
46  
47  
48  
49  
50  
51  
52  
53  
54  
55  
56  
57  
58  
59  
60  
61  
62  
63  
64  
65

1269 Fig. 10. (A) Primitive mantle-normalized trace element, and (B) chondrite-normalized  
1270 rare earth element diagrams for porphyry and basaltic–andesitic dike samples from Red  
1271 Chris. The normalization values for primitive mantle chondrite are from Sun and  
1272 McDonough (1989).

1274 Fig. 11.  $\epsilon_{Nd}(t)$  vs. initial  $^{87}Sr/^{86}Sr$  ratios for porphyry and basaltic–andesitic dike samples  
1275 from Red Chris, calculated at  $t = 200$  Ma. All the samples fall in the field of Mesozoic  
1276 igneous rocks in the Stikine island arc terrane, clearly different from the Late Cretaceous  
1277 to Eocene plutons in the Northern Coast Plutonic Complex, which were derived from  
1278 evolved crust. The depleted MORB mantle field is from Pilet et al. (2011); the Stikinia  
1279 Mesozoic igneous rock field is from Samson et al. (1989); the Northern Coast Plutonic  
1280 Complex field is from Samson et al. (1991) and Patchett et al. (1998); all data are re-  
1281 calculated at 200 Ma.

1283 Fig. 12. Histogram and relative probability curve for zircon  $\epsilon_{Hf}(t)$  values from (A) P1, (B)  
1284 P2E, (C) P2L, and (D) P3 porphyry samples.

1286 Fig. 13. Classification diagram and plots of oxidation state, temperature, pressure, and  
1287 magmatic water content estimated from amphibole compositions from P2E and P2L  
1288 porphyry samples at Red Chris. A.  $C(Al^{VI} + Fe^{3+} + 2Ti^{4+})$  (apfu) vs.  $A(Na^{+} + K^{+})$  (apfu). B.  
1289  $\Delta FMQ$  vs. temperature. C.  $\Delta FMQ$  vs. pressure. D.  $\Delta FMQ$  vs. magmatic water content.  
1290 The classification diagram for calcic amphibole is given by the Excel spreadsheet of

1  
2  
3  
4  
5  
6  
7  
8  
9  
10  
11  
12  
13  
14  
15  
16  
17  
18  
19  
20  
21  
22  
23  
24  
25  
26  
27  
28  
29  
30  
31  
32  
33  
34  
35  
36  
37  
38  
39  
40  
41  
42  
43  
44  
45  
46  
47  
48  
49  
50  
51  
52  
53  
54  
55  
56  
57  
58  
59  
60  
61  
62  
63  
64  
65

1291 Locock (2014), and the superscript C and A represent C and A cations following the  
1292 general amphibole formula ( $AB_2C_5T_8O_{22}W_2$ ), respectively. Note that potassic-magnesian-  
1293 hastingsite is included in the field of magnesian-hastingsite.  $\Delta FMQ$  values, temperatures,  
1294 and magmatic water content were calculated from the spreadsheet of Ridolfi et al. (2010).  
1295 Amphibole crystallization pressures were calculated using the equation of Mutch et al.  
1296 (2016). The  $\Delta FMQ$  values were calculated following the equation of Myers and Eugster  
1297 (1983):  $\log fO_2 = -24,441.9/T (K) + 8.290 (\pm 0.167)$ . Abbreviation: apfu = atoms per  
1298 formula unit.

1299  
1300 Fig. 14. Photomicrographs (cross-polarized transmitted light), Backscattered electron  
1301 (BSE) images, and electron microprobe analysis profiles for FeO and anorthite proportion  
1302 ( $X_{An}$ ) for representative plagioclase crystals from the P2E, P2L, and P3 porphyries at Red  
1303 Chris. Red circles on photomicrographs and white circles on BSE images denote the  
1304 analyzed spots. The error bars for  $X_{An}$  and FeO analyses are smaller than the size of the  
1305 symbols. Abbreviations: Amp = amphibole; Ap = apatite; Pl = plagioclase; Ser = sericite.

1306  
1307 Fig. 15. Chondrite-normalized REE patterns for zircons from (A) P1, (B), P2E, (C) P2L,  
1308 and (D) P3 porphyry samples from Red Chris. Normalization values are from Sun and  
1309 McDonough (1989).

1310  
1311 Fig. 16. Zircon  $Eu_N/Eu_N^*$  vs. temperature diagram.  $Eu_N/Eu_N^*$  is the europium anomaly,  
1312 calculated as  $Eu_N/Eu_N^* = Eu_N/(Sm_N \times Gd_N)^{0.5}$ , using the chondrite normalization values



1  
2  
3  
4  
5  
6  
7  
8  
9  
10  
11  
12  
13  
14  
15  
16  
17  
18  
19  
20  
21  
22  
23  
24  
25  
26  
27  
28  
29  
30  
31  
32  
33  
34  
35  
36  
37  
38  
39  
40  
41  
42  
43  
44  
45  
46  
47  
48  
49  
50  
51  
52  
53  
54  
55  
56  
57  
58  
59  
60  
61  
62  
63  
64  
65

1313 of Sun and McDonough (1989). Oxidized suites have zircon  $Eu_N/Eu_N^*$  values  $>0.4$   
1314 (Dilles et al., 2015).

1315

1316 Fig. 17. Backscattered electron images of apatite crystals in samples from (A) P1 (RC13-  
1317 39), (B) P2E (RC13-107), (C) P2L (RC13-33), and (D) P3 (RC13-78). Concentrations of  
1318  $SO_3$  and Cl in apatite crystals are shown in wt. % ( $SO_3/Cl$ ); red circles represent the  
1319 analyzed spots. Higher concentrations are observed in apatites from P2E and P2L; some  
1320 apatite microphenocrysts from P2 porphyries show zoning from  $SO_3$ -Cl-rich cores to  
1321  $SO_3$ -Cl-poorer rims (C).

1322

1323 Fig. 18. Plots of (A) S, and (B) F vs. Cl contents for apatite microphenocrysts from P1 to  
1324 P3 porphyry samples at Red Chris. Abbreviation: apfu = atoms per formula unit. Data  
1325 from Digital Appendix Table A8.

Figure 1

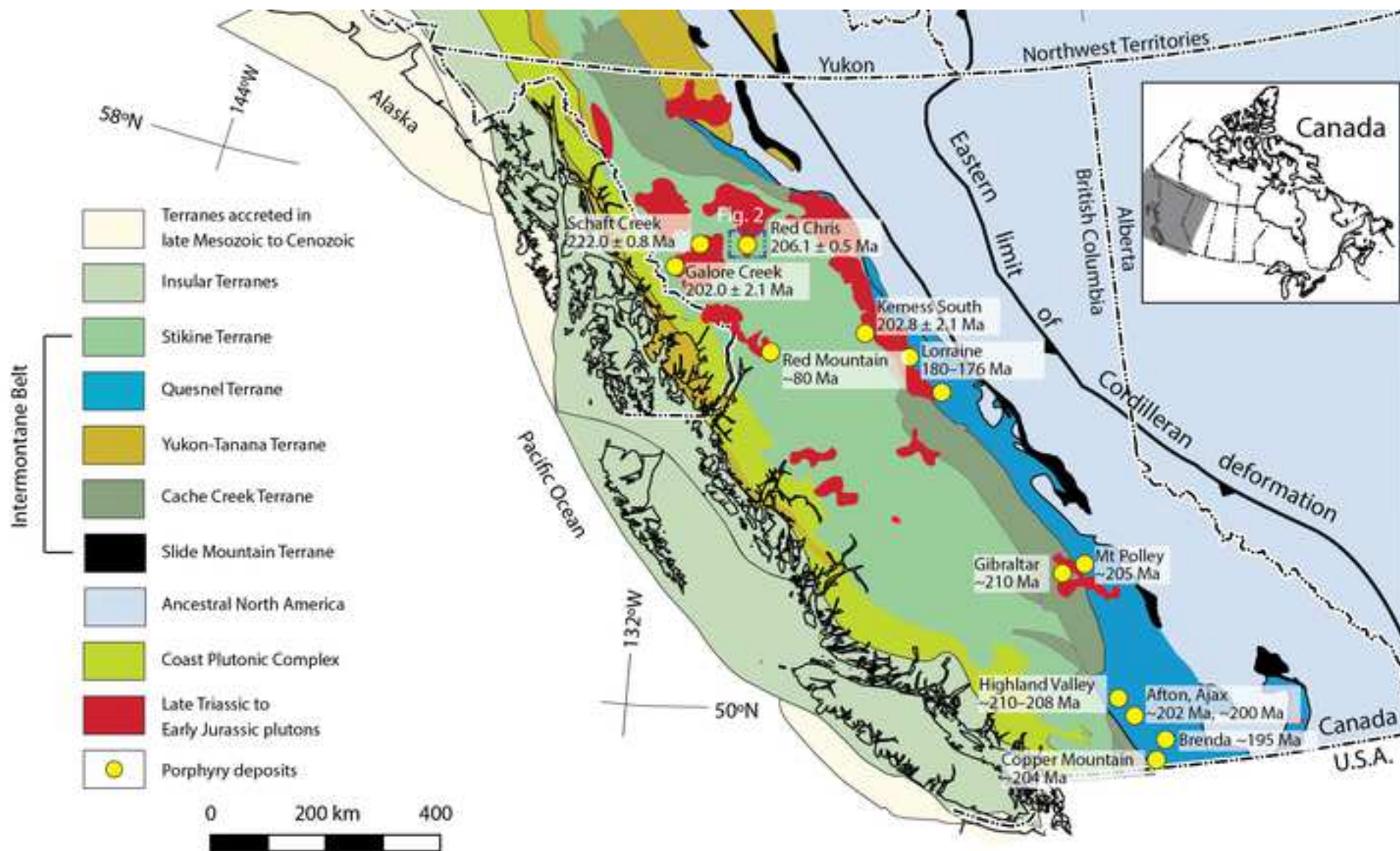
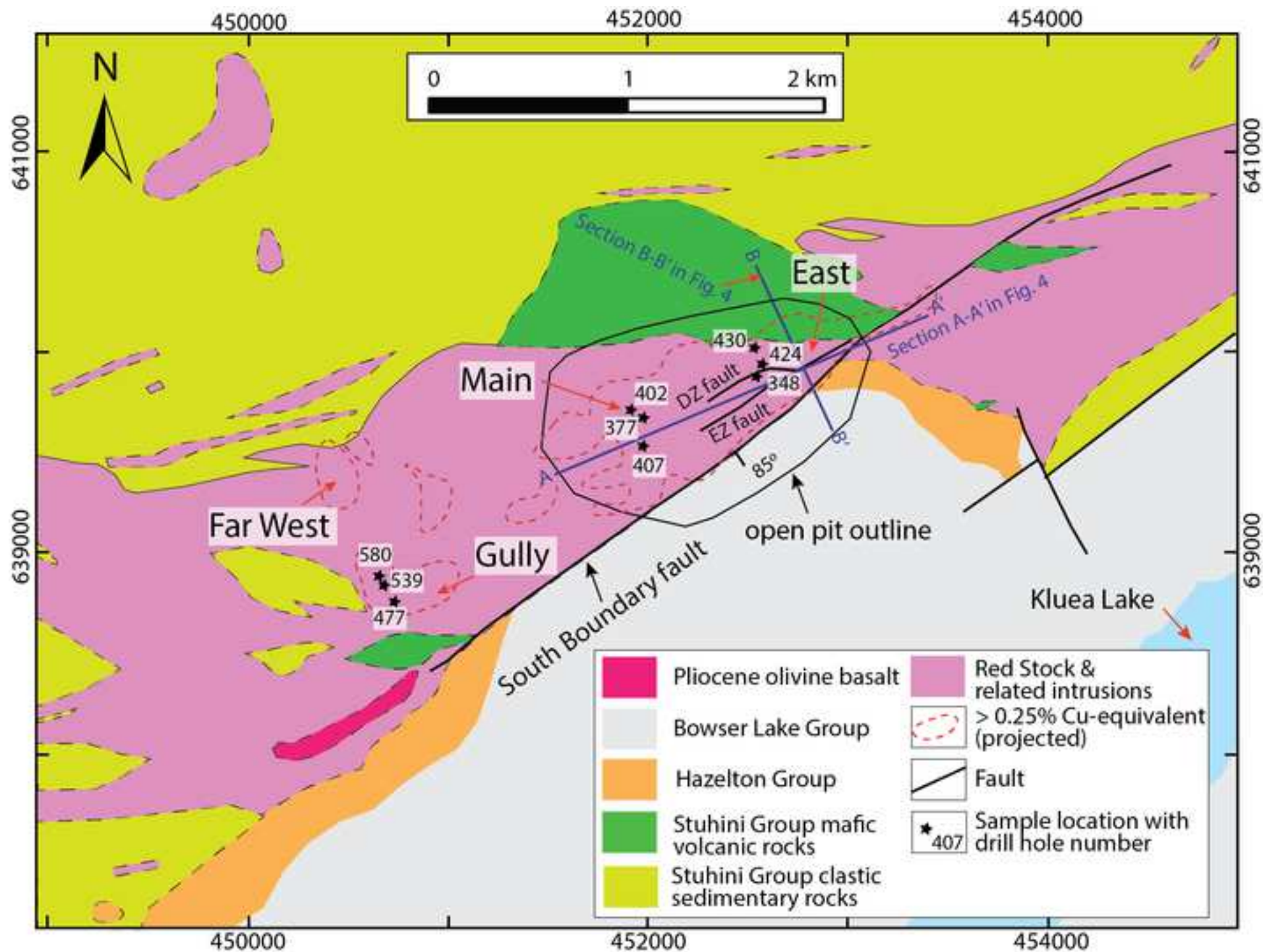
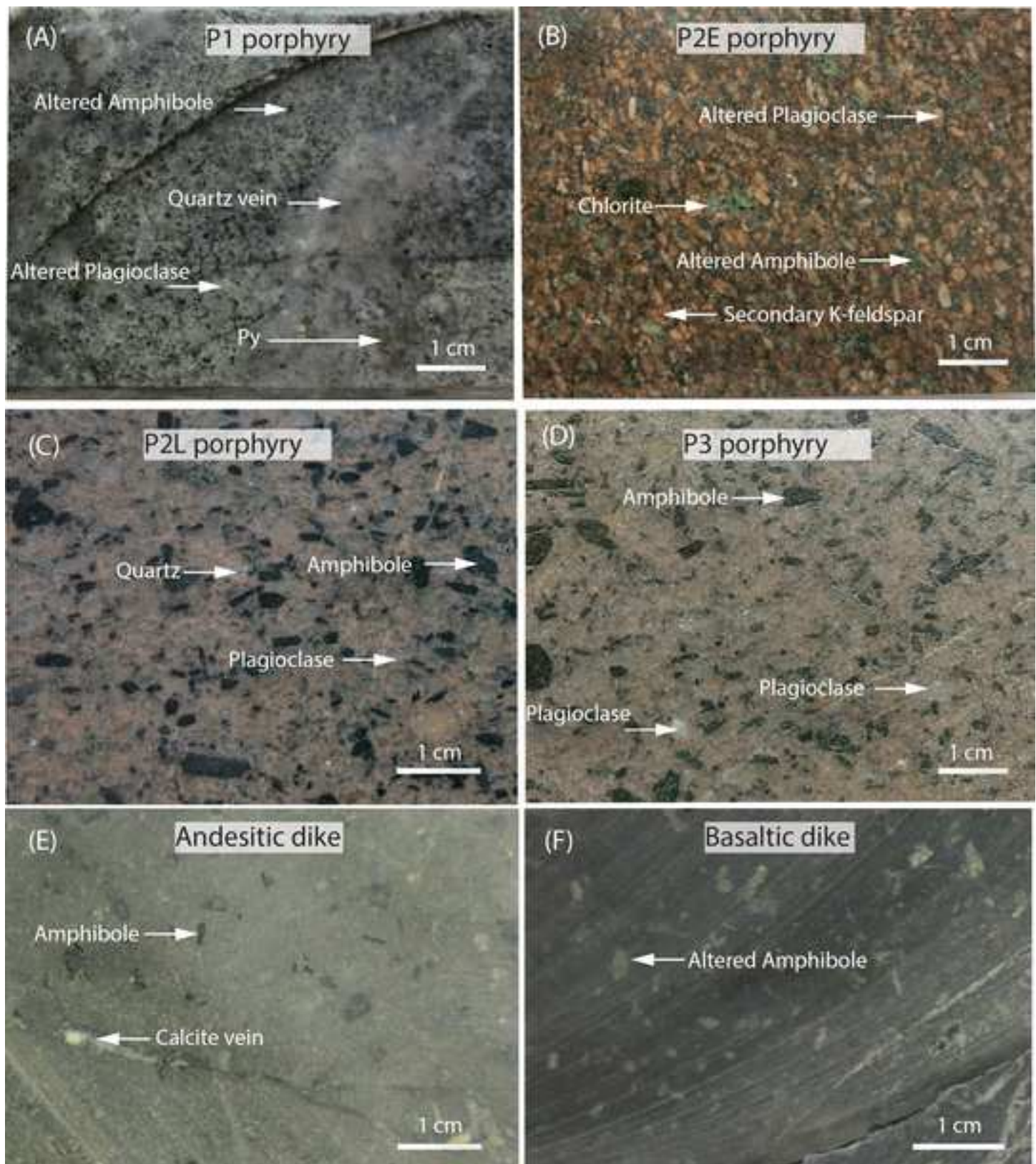
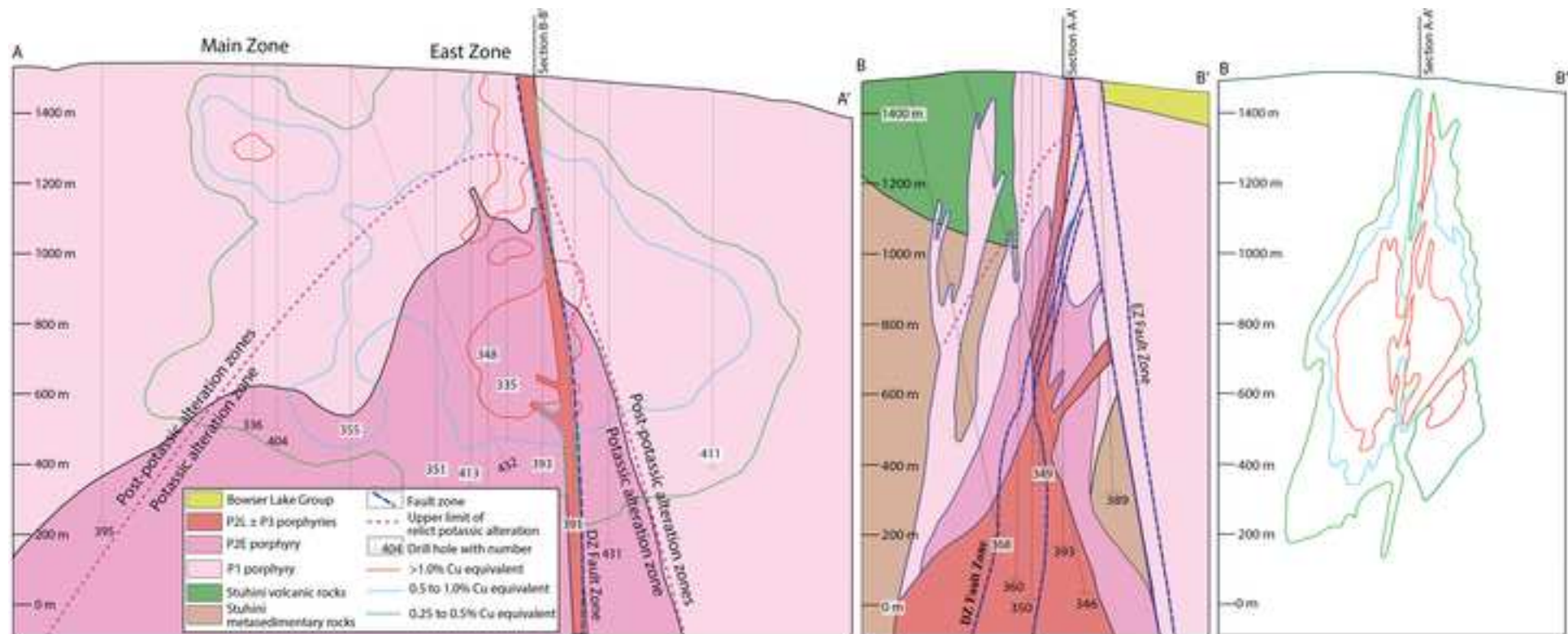


Figure 2

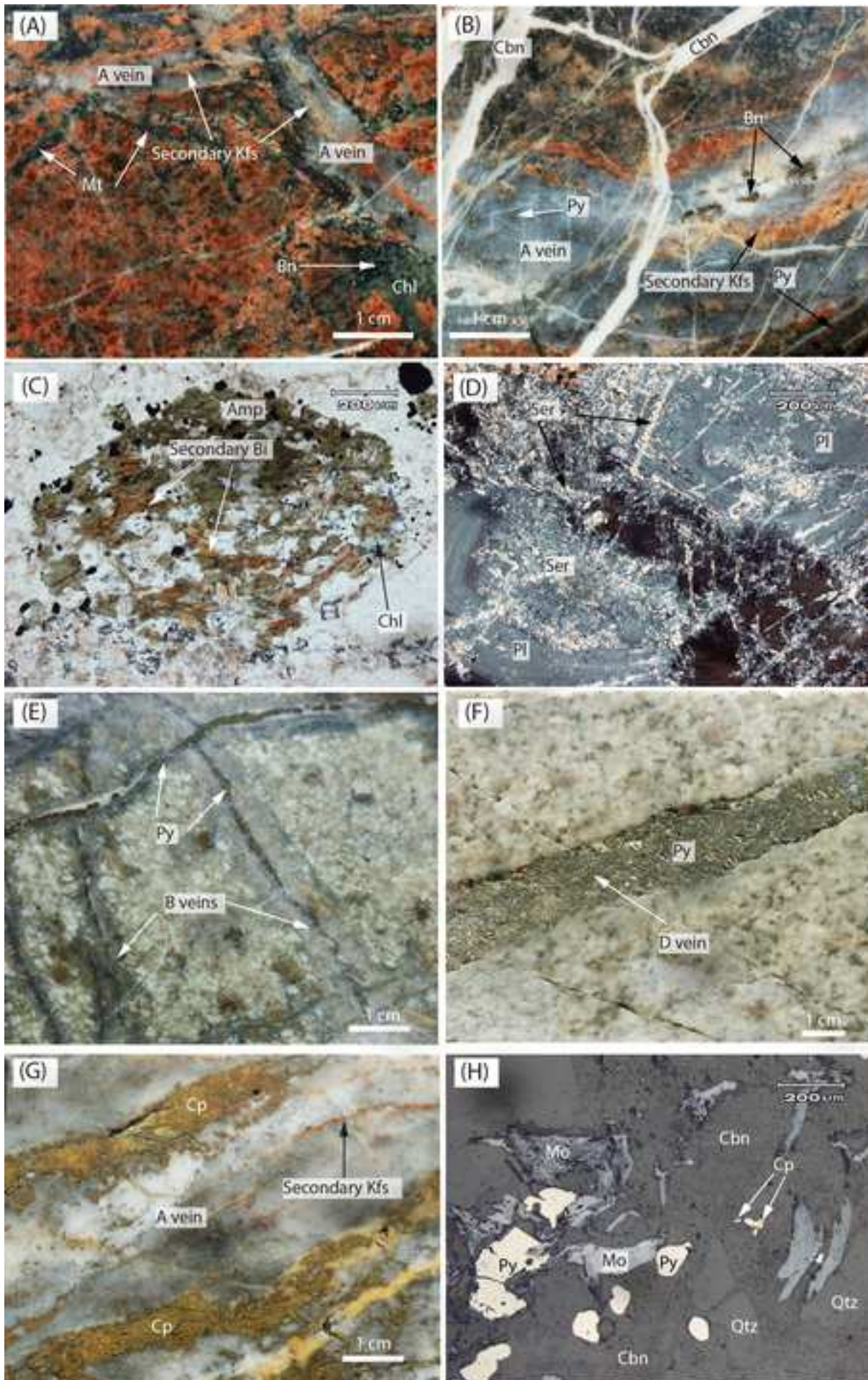




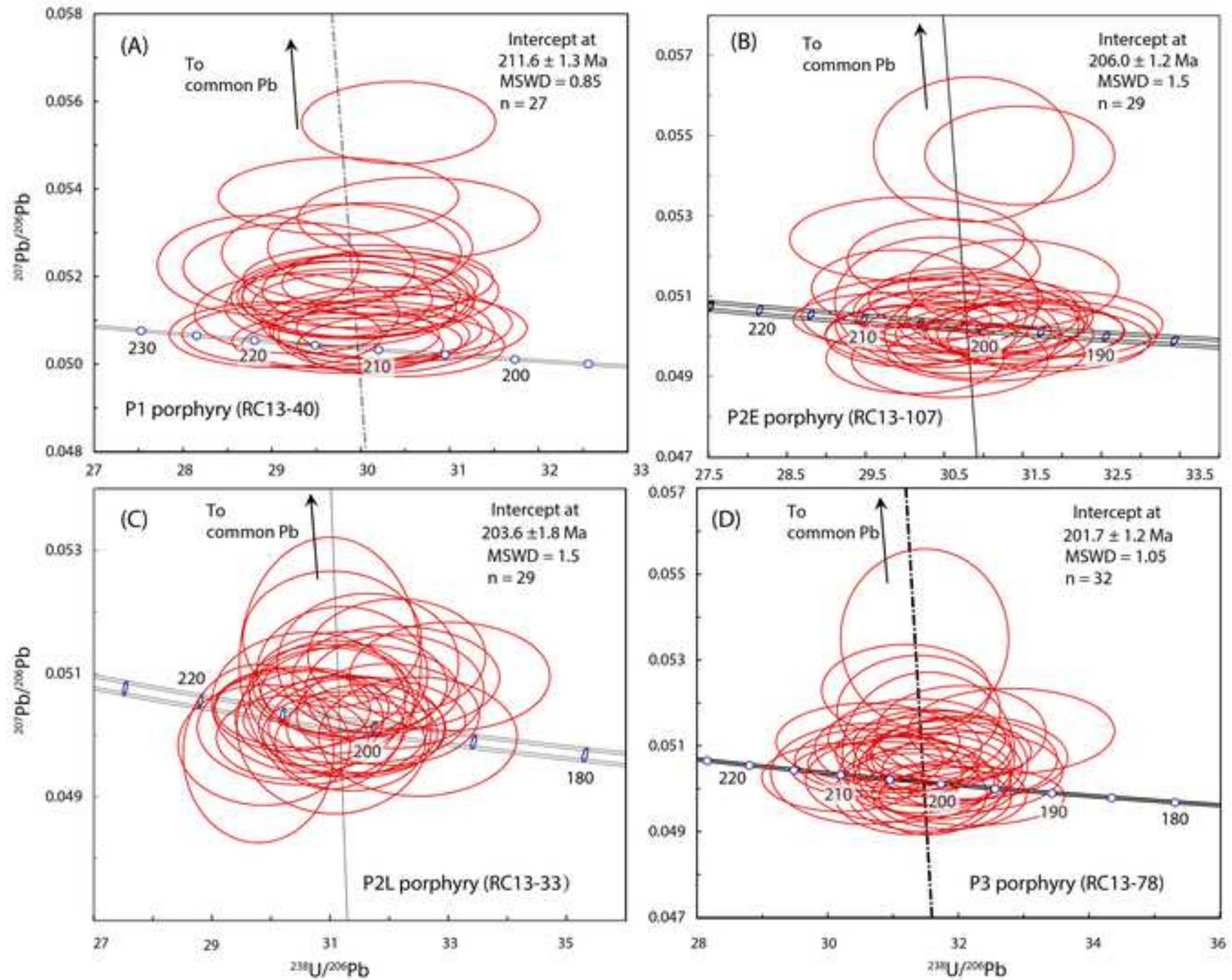












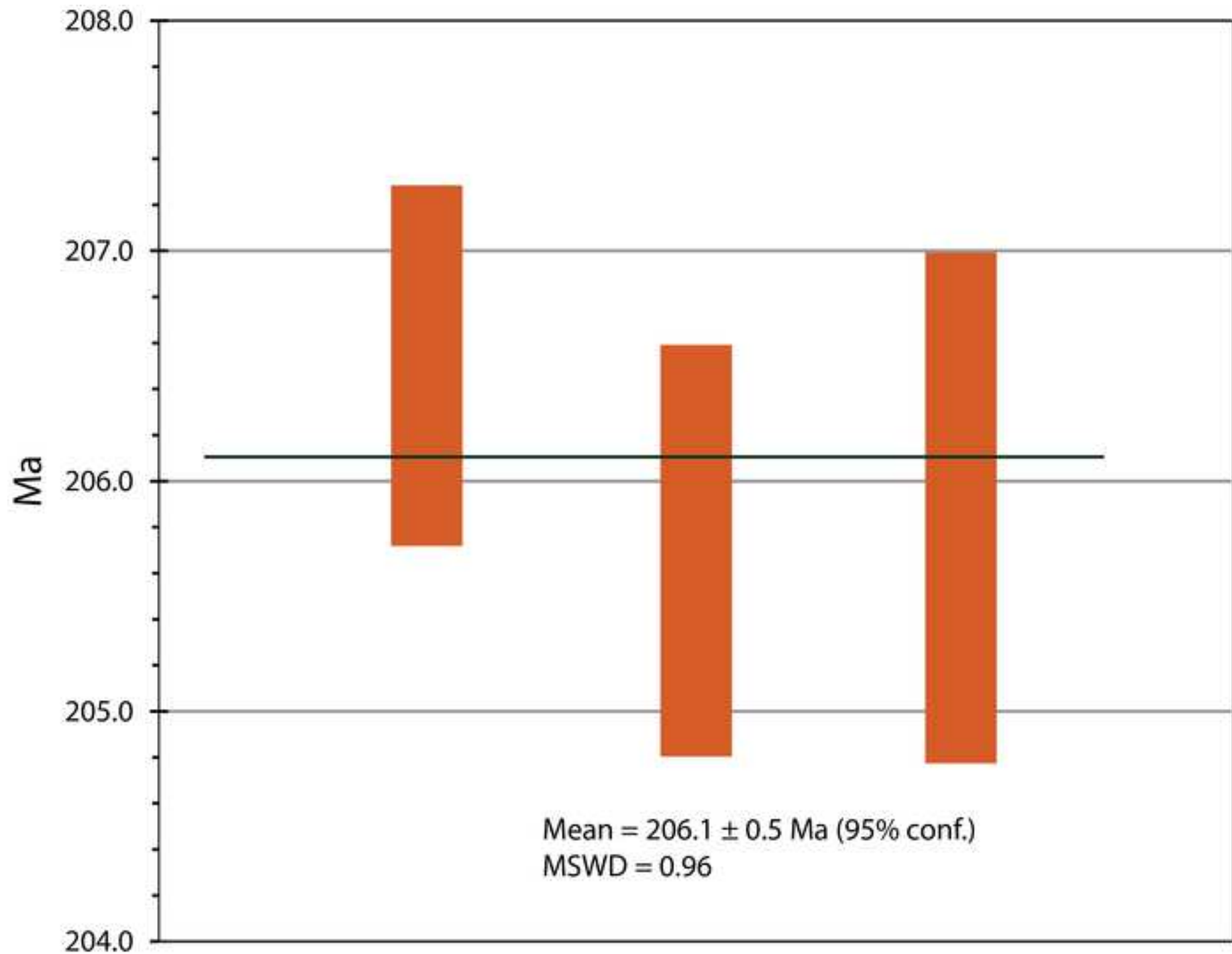
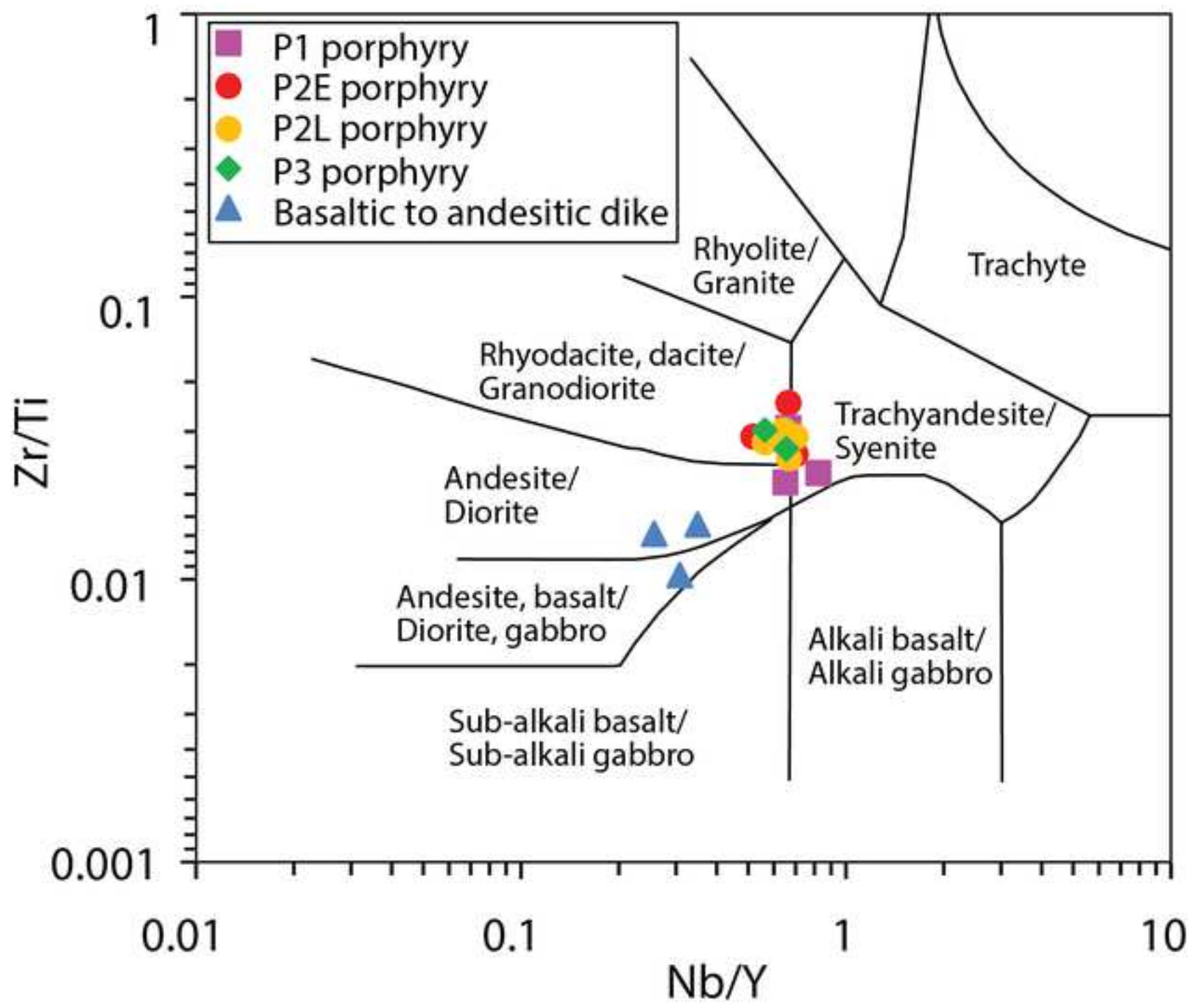
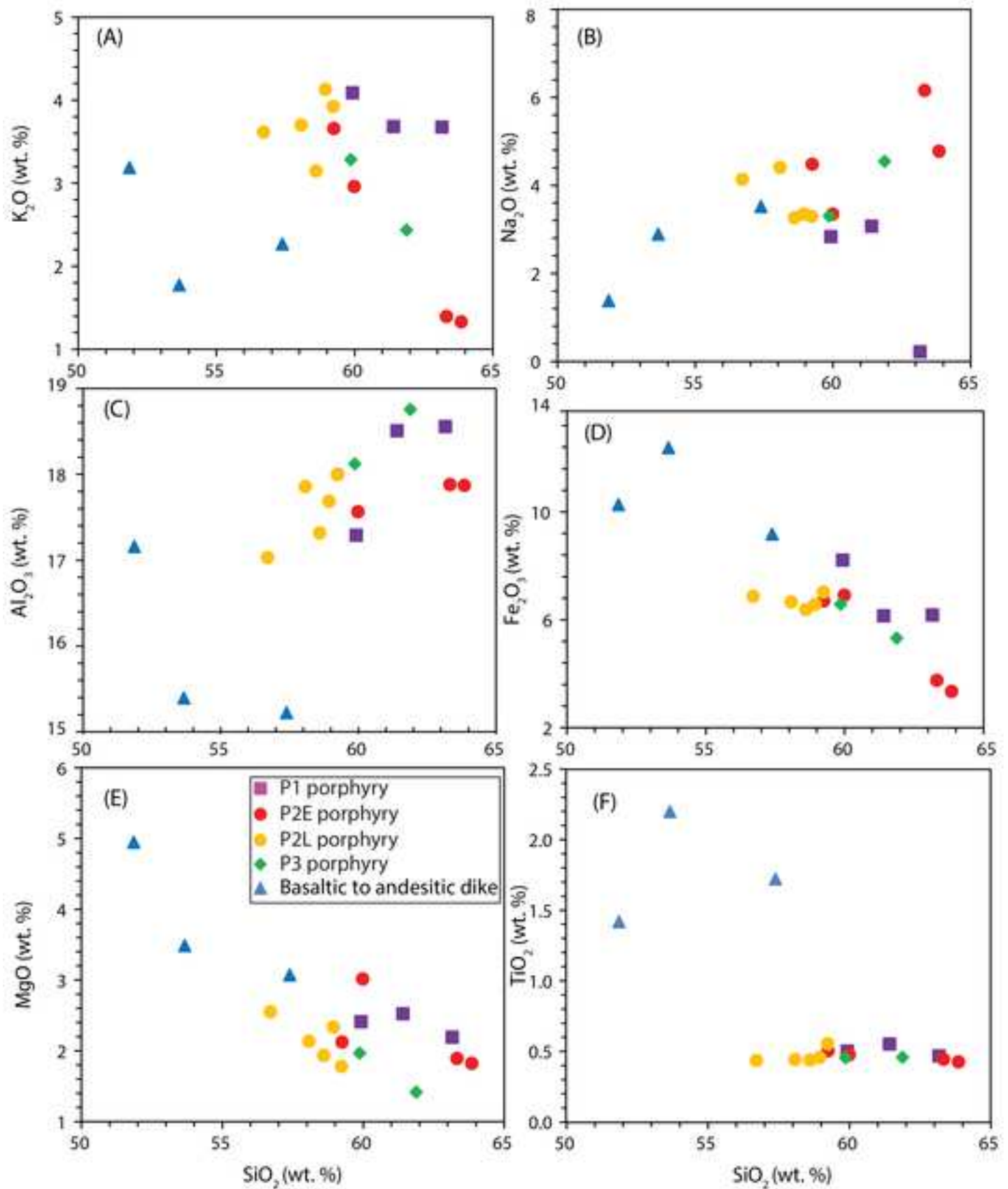
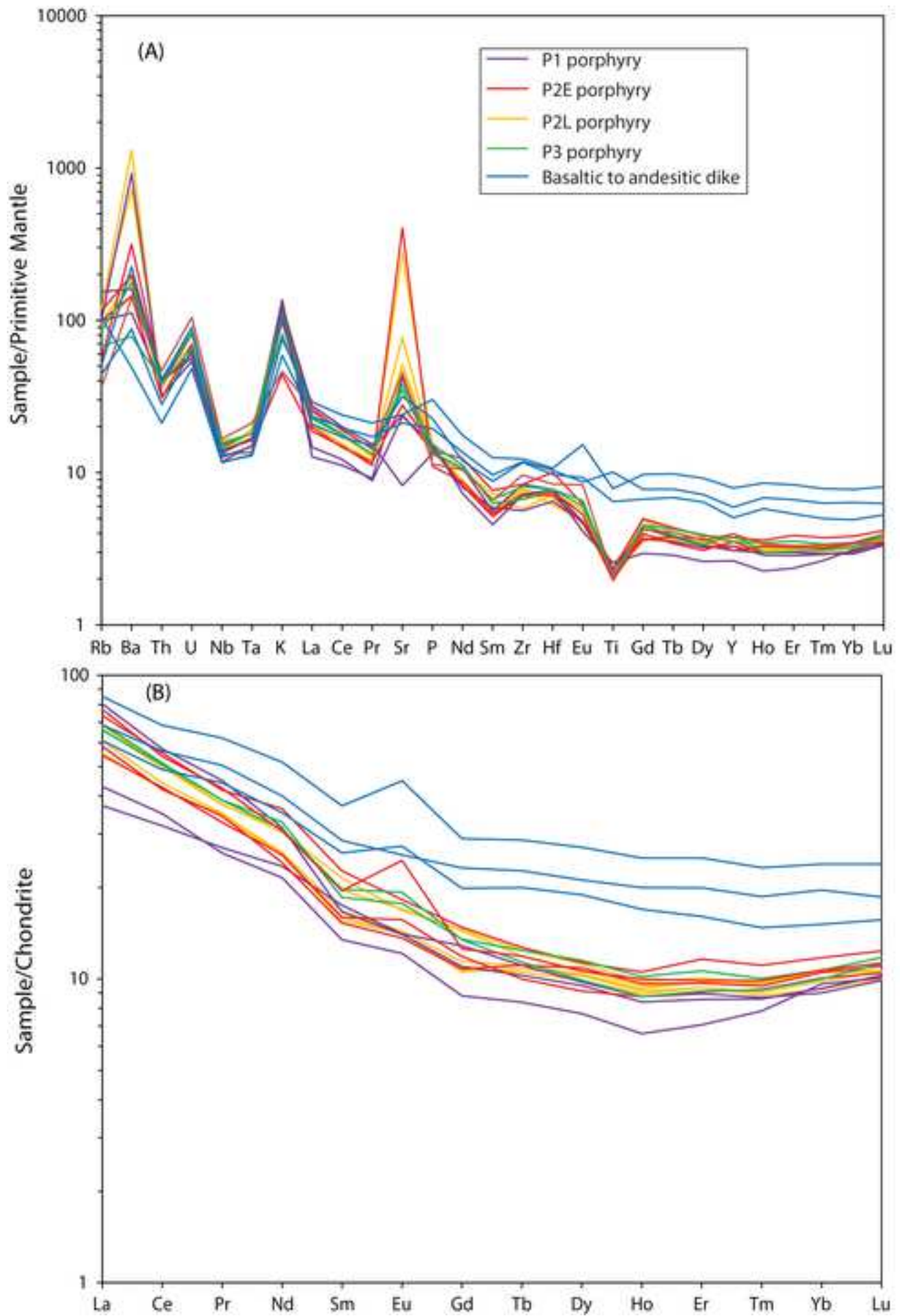


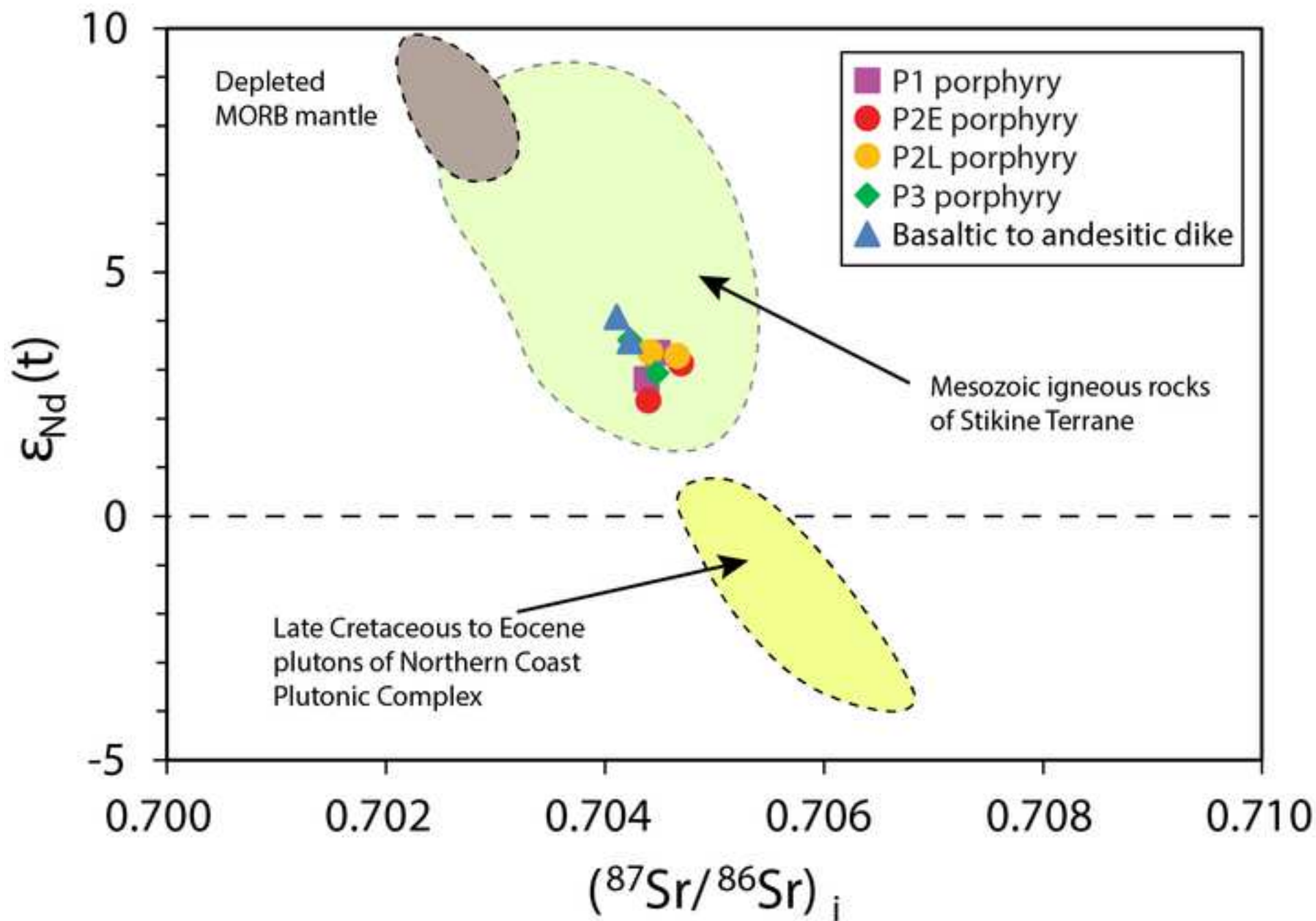


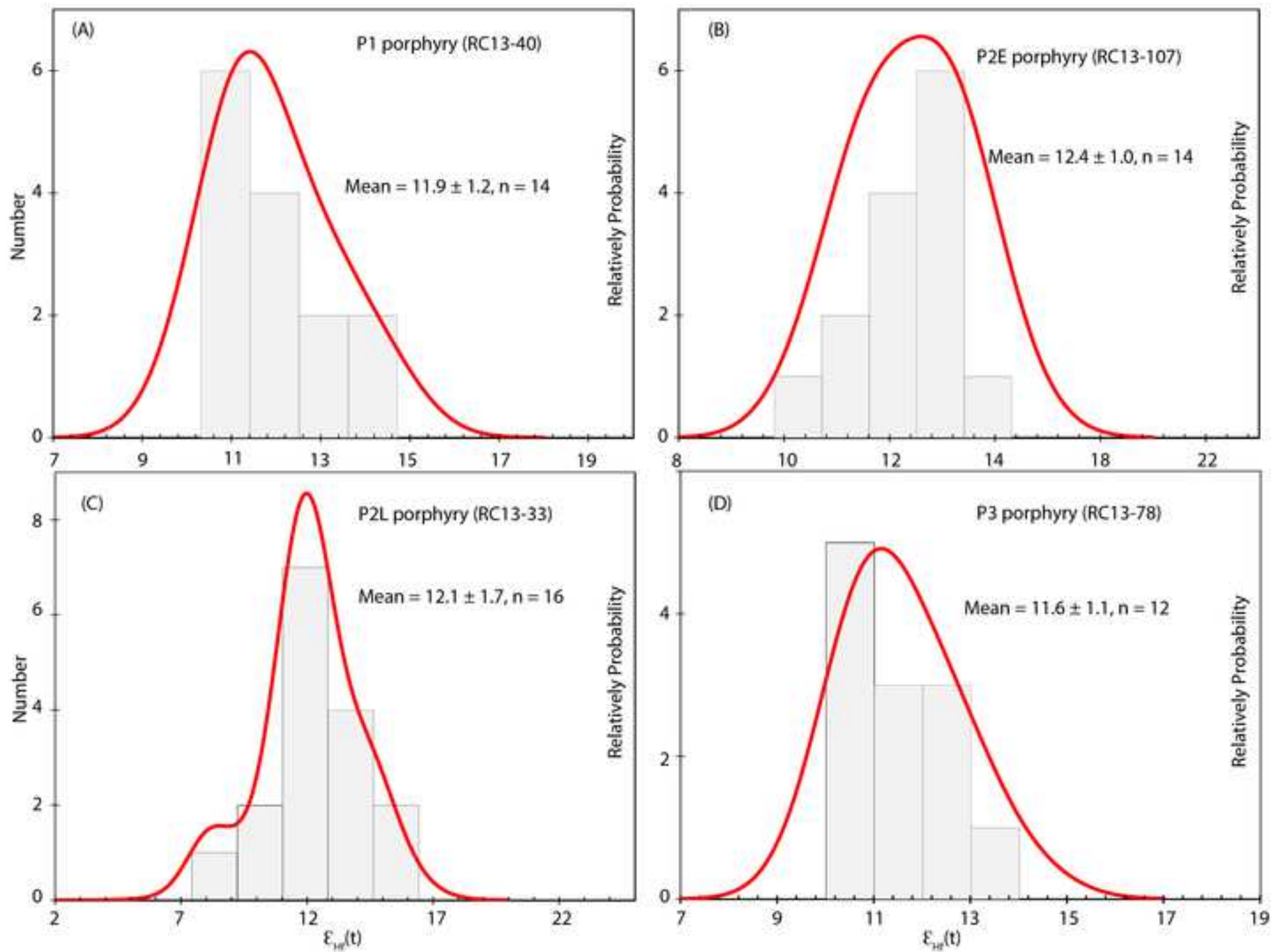
Figure 8



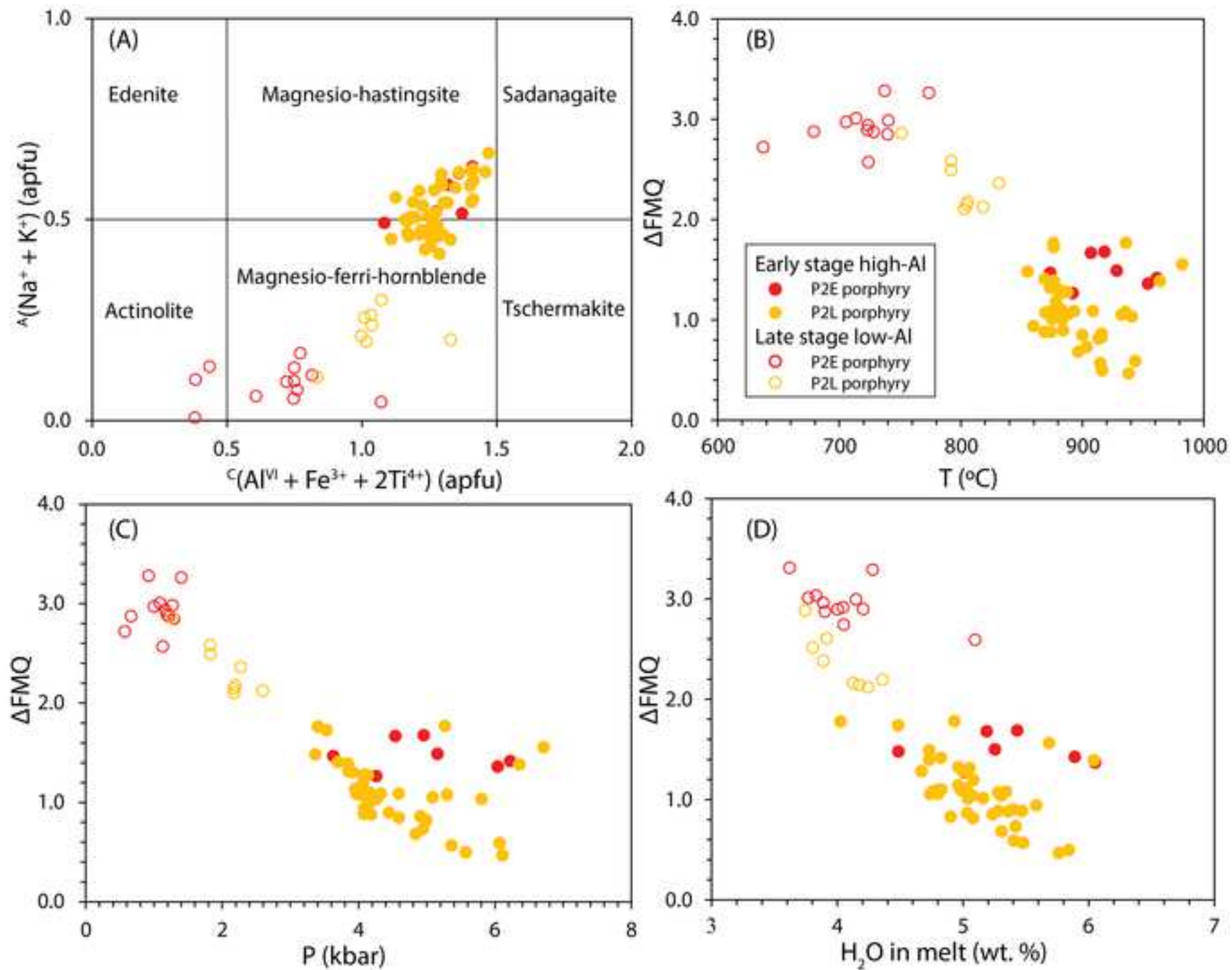


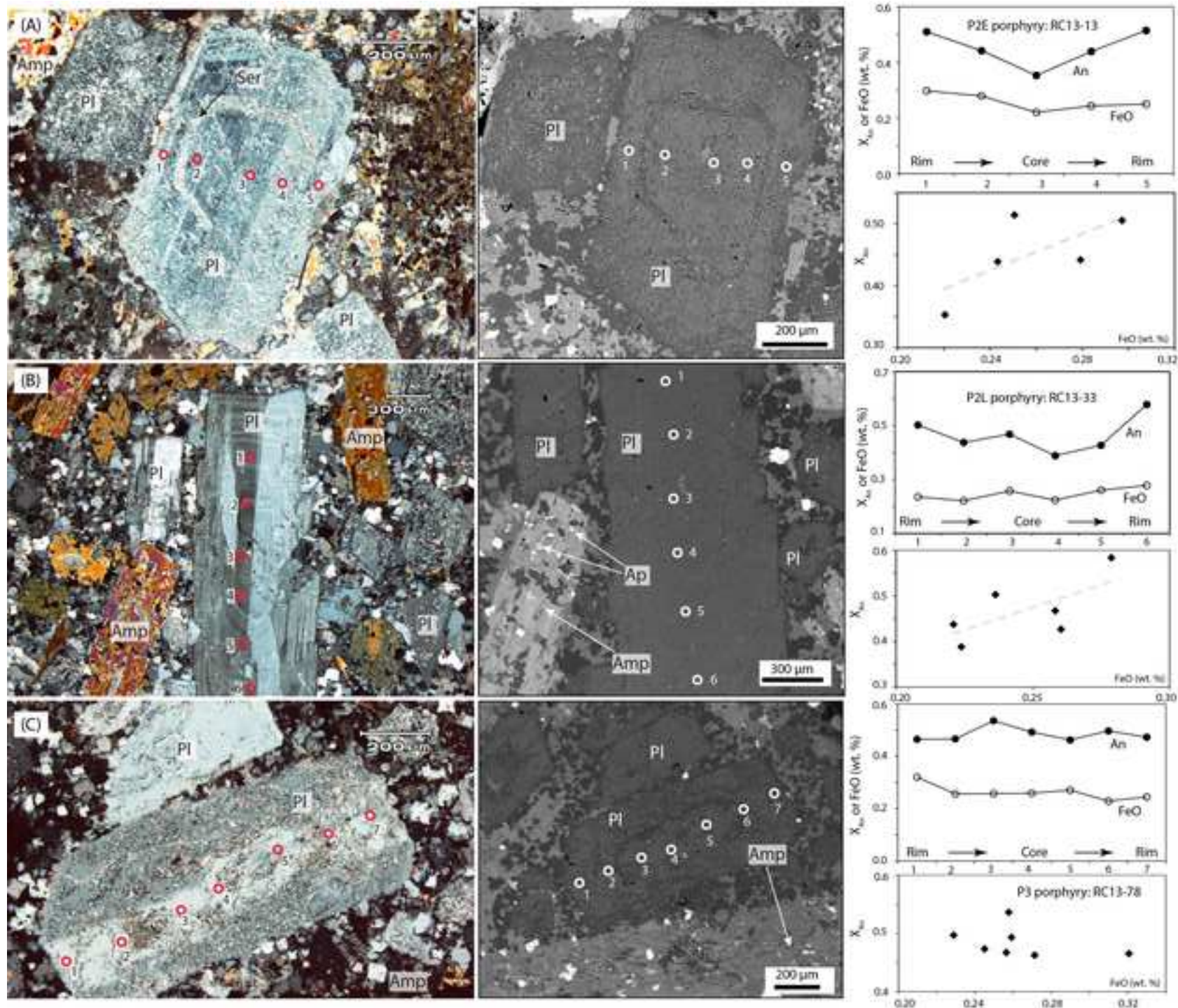














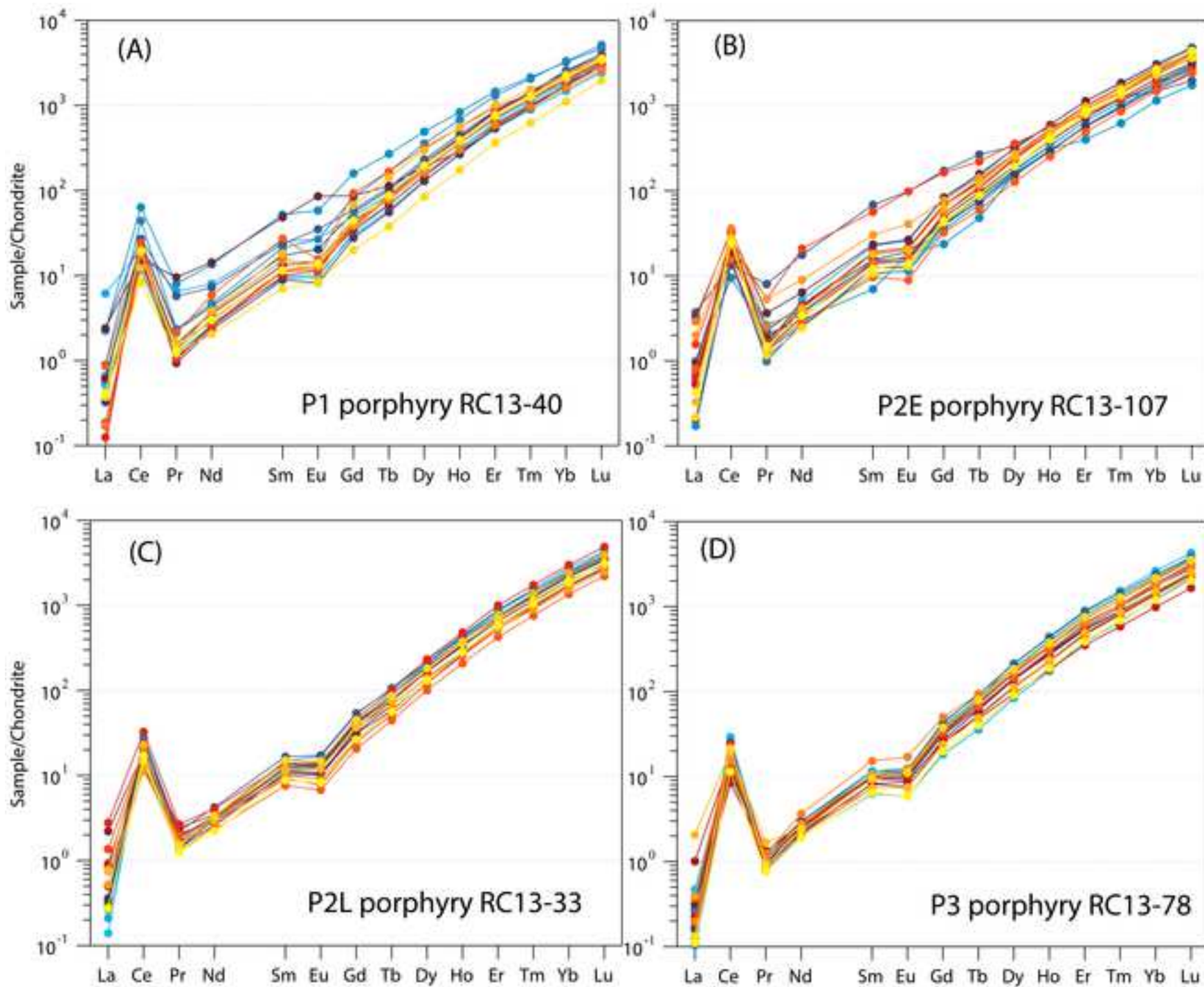
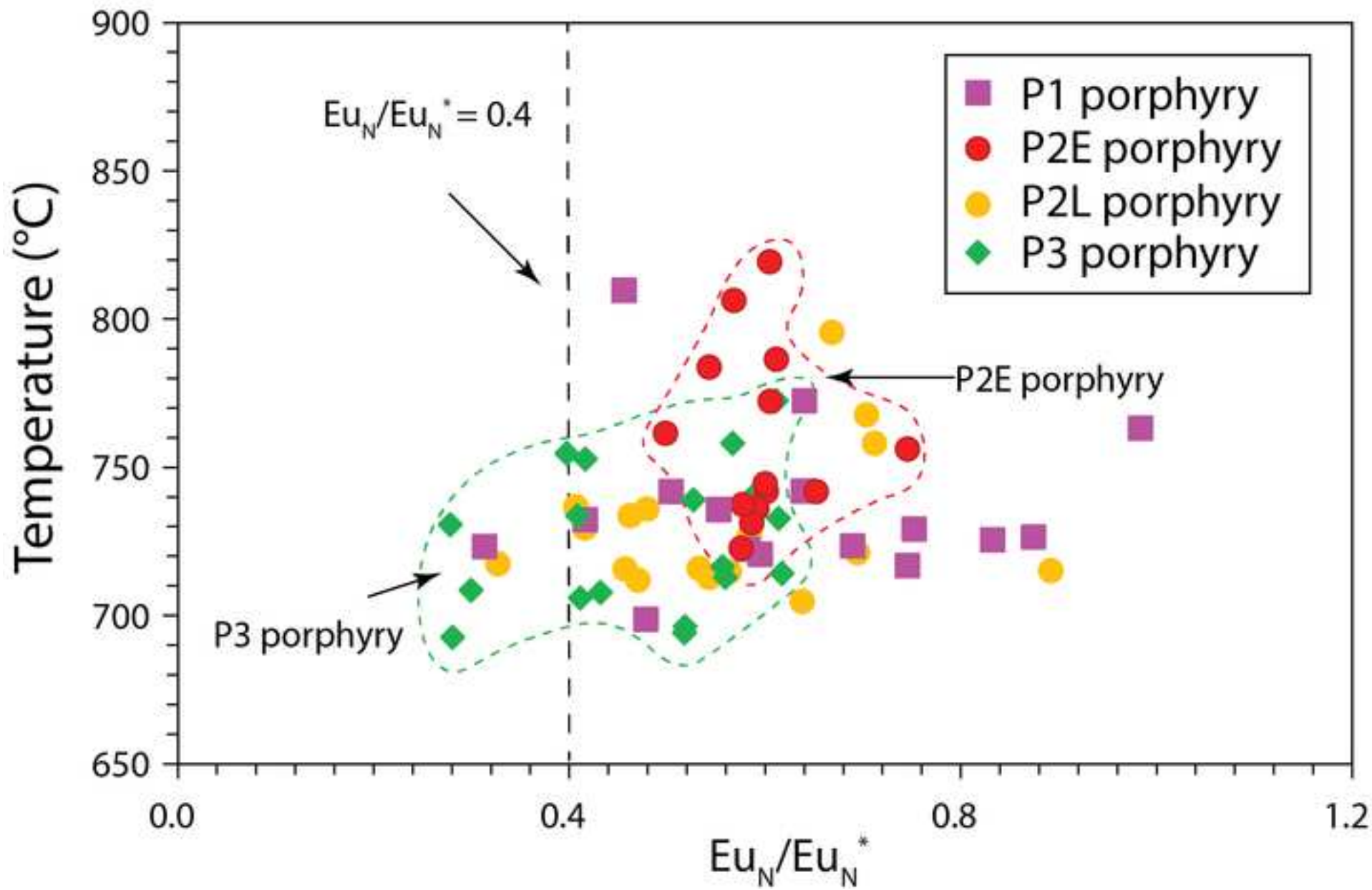
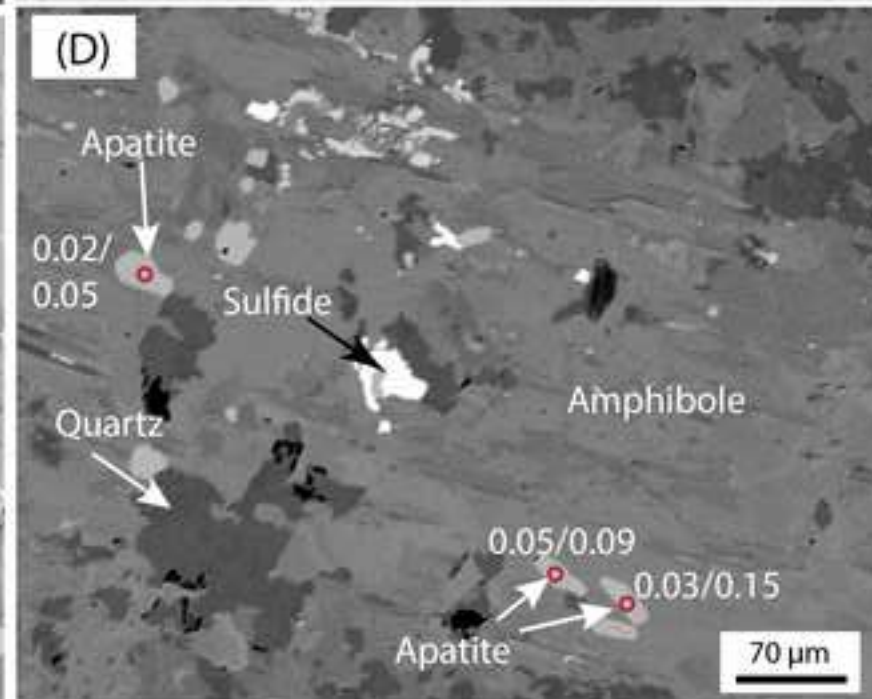
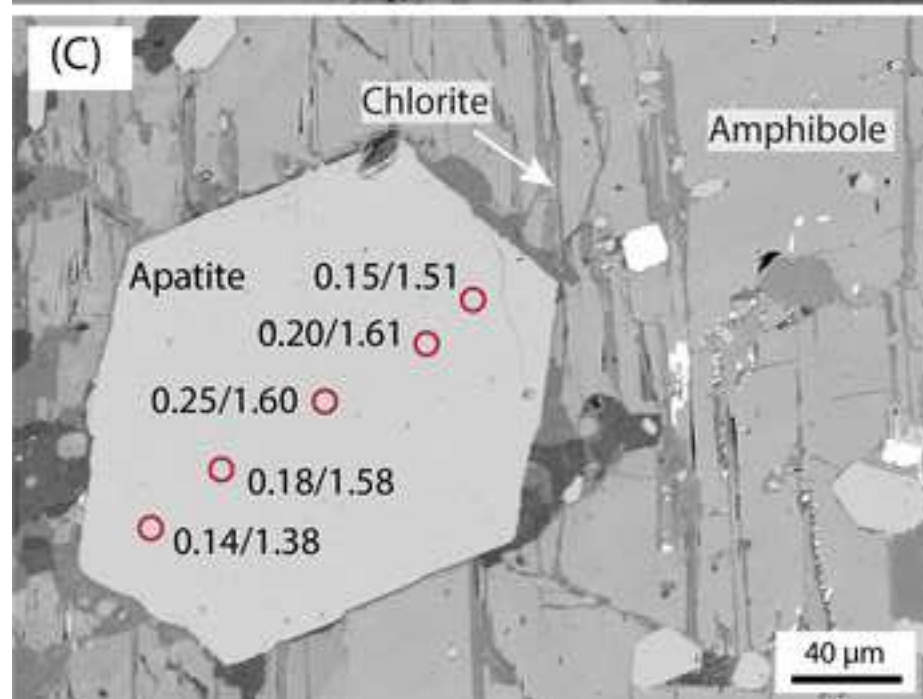
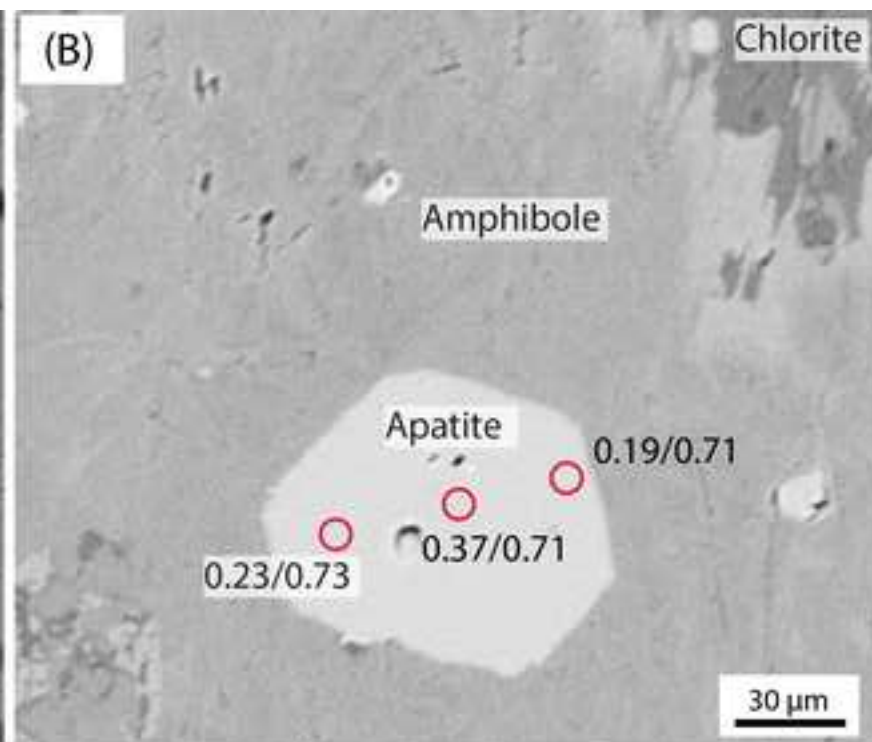
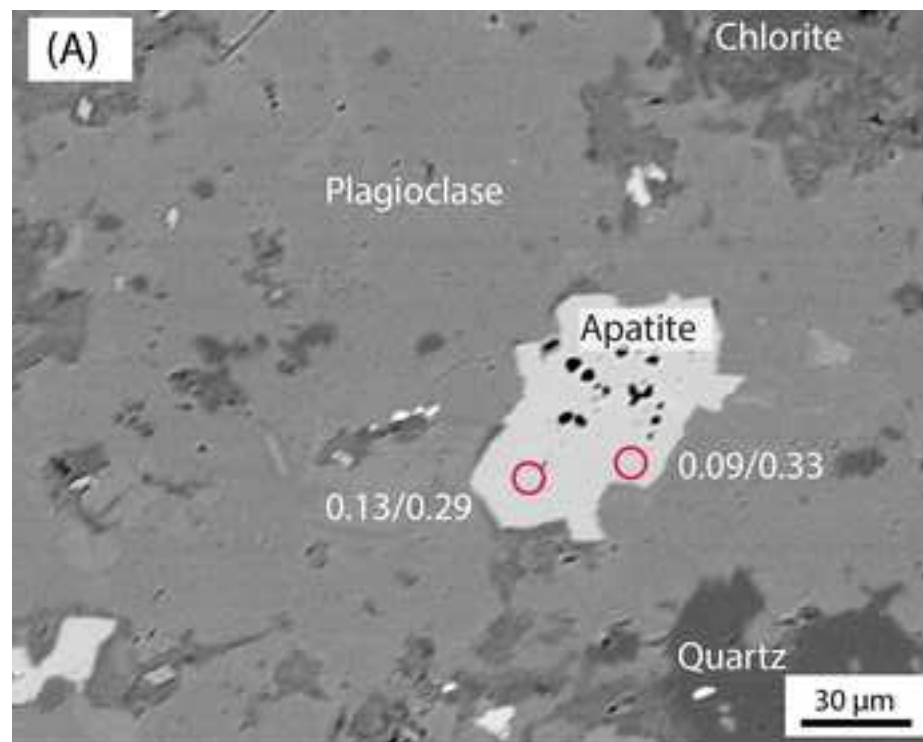
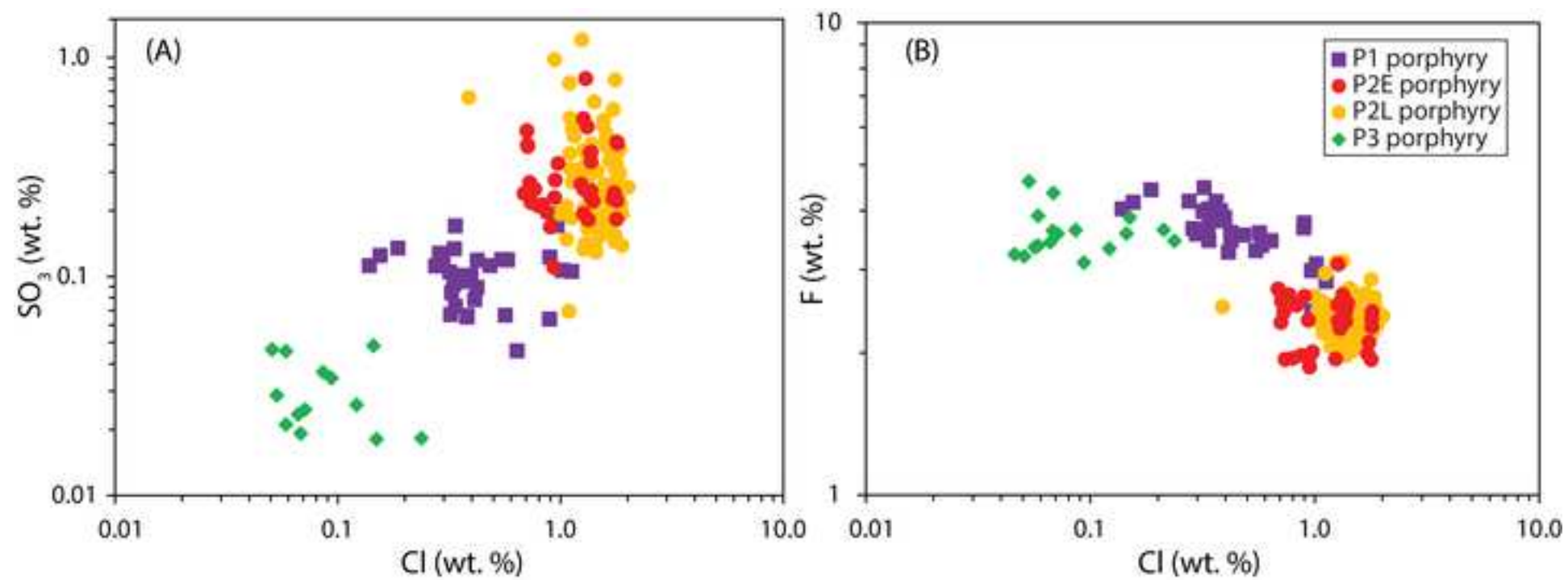




Figure 16







**Table 1. Re-Os Isotope Analyses for molybdenite from the Red Chris Cu-Au deposit**

Sample	Description	Re ( $\mu\text{g/g}$ )	$\pm 2\sigma$	$^{187}\text{Re}$ ( $\mu\text{g/g}$ )	$\pm 2\sigma$	$^{187}\text{Os}$ ( $\text{ng/g}$ )	$\pm 2\sigma$	Model Age (Ma)
RC13-82	Quartz-carbonate-pyrite-	497.8	1.3	312.9	0.8	1078	0.0	206.5
RC13-88	molybdenite-chalcopyrite	1771	5.0	1113	3.0	3821	2.0	205.7
RC13-103	vein in P2E porphyry	1124	3.0	706	1.8	2427	4.0	205.9

Note: See the Digital Appendix Table A1 for sample locations.

$\pm 2\sigma$ (Ma)
0.8
0.9
1.1

**Table 2. Major and trace element compositions of porphyry and basaltic to andesitic dike rocks**

Sample # - Detection	RC13-39	RC13-40	RC13-63	RC13-37	RC13-42	RC13-92	RC13-107	RC13-25	RC13-26	
Lithology	↓	P1	P1	P1	P2E	P2E	P2E	P2E	P2L	P2L
<i>Weight %</i>										
SiO <sub>2</sub>	0.01	55.43	56.57	58.25	55.54	58.61	61.29	56.4	53.86	56.05
Al <sub>2</sub> O <sub>3</sub>	0.01	15.94	16.57	17.5	16.21	16.35	17.25	17.08	16.12	17.18
Fe <sub>2</sub> O <sub>3</sub> (T)	0.01	7.59	5.53	5.83	6.4	3.06	3.63	6.38	6.52	6.42
MnO	0.001	0.067	0.079	0.107	0.135	0.028	0.057	0.152	0.134	0.125
MgO	0.01	2.23	1.96	2.39	2.79	1.67	1.83	2.02	2.42	2.06
CaO	0.01	2.54	3.12	2.11	5.53	3.86	3.63	3.47	4.78	4.57
Na <sub>2</sub> O	0.01	2.62	0.19	2.91	3.1	4.38	5.96	4.26	3.93	4.25
K <sub>2</sub> O	0.01	3.78	3.29	3.49	2.74	1.22	1.35	3.48	3.43	3.57
TiO <sub>2</sub>	0.001	0.463	0.419	0.523	0.441	0.39	0.429	0.48	0.414	0.426
P <sub>2</sub> O <sub>5</sub>	0.01	0.29	0.26	0.32	0.3	0.22	0.24	0.29	0.3	0.29
LOI		7.51	10.44	5.15	7.42	8.22	3.22	4.81	5.03	3.49
S	0.001	4.63	3.65	0.386	0.026	1.63	1.19	1.22	0.251	0.157
Total		98.45	98.43	98.57	100.6	98.02	98.9	98.81	96.94	98.43
<i>Parts per million</i>										
Ba	1	6440	783	1123	1012	2201	980	1382	9182	5082
Co	0.1	10.5	9.4	16.2	12.7	10.6	8.3	9.3	11.4	12
Cr	0.5	24.9	30.2	26.3	115	50.1	19.4	26	31.2	32.8
Cs	0.1	3.7	2.1	4.2	6.7	4.5	0.8	1.1	4.7	4.9
Ga	1	17	14	17	15	15	15	17	15	17
Ge	0.5	3.2	2.4	1.4	2	3.1	2	1.8	1.7	1.9
Hf	0.1	2	2.4	2.4	2.2	2.3	2.6	3.1	2.2	2.2
Nb	0.2	9	9.6	10	9.9	8.4	11.9	10.8	10.1	11.5
Ni	1	5	7	32	23	3	7	3	5	6
Pb	5	14	8 < 5	< 5	< 5	< 5	< 5	< 5	< 5	< 5
Rb	1	64	63	98	63	35	23	73	74	76
Sc	0.01	19.9	11.8	15	17.6	10.5	9.78	13	15.9	15.9
Sr	2	884	174	493	586	8516	944	508	5880	1639
Ta	0.01	0.61	0.69	0.67	0.68	0.62	0.87	0.74	0.67	0.73
Zr	1	63	94	80	79	81	108	94	85	65
Hf	0.1	2	2.4	2.4	2.2	2.3	2.6	3.1	2.2	2.2
U	0.01	1.13	1.72	1.19	1.46	1.26	2.2	1.75	1.31	1.69
Th	0.05	2.71	3.23	3.38	2.64	3.41	3.97	3.52	2.63	3.2
V	5	147	105	134	147	109	110	114	135	135
Y	1	14	15	12	14	16	18	17	14	16
Zn	1	724	123	58	101	29	32	56	72	79
Zr	1	63	94	80	79	81	108	94	85	65
Tl	0.05	0.59	1.02	0.6	0.51	0.17	0.12	0.12	0.28	0.06
La	0.05	8.74	18.9	10.1	13.7	12.8	18.1	17.3	13.7	15.6
Ce	0.05	19.8	35.5	21.7	26.1	26.5	33.5	34.4	26	30.9
Pr	0.01	2.54	4.23	2.44	3.23	3.08	3.99	3.93	3.24	3.52
Nd	0.05	10.8	14.5	9.9	11.1	11.8	14.1	16.7	11.7	14.4
Sm	0.01	2.62	2.49	2.02	2.29	2.39	2.93	3.4	2.33	2.94
Eu	0.005	0.801	0.799	0.691	0.778	0.893	1.4	1.04	0.805	0.968
Gd	0.01	2.57	2.2	1.76	2.16	2.37	2.51	2.96	2.11	2.88
Tb	0.01	0.41	0.38	0.31	0.41	0.37	0.44	0.47	0.4	0.44
Dy	0.01	2.44	2.38	1.92	2.72	2.28	2.65	2.83	2.56	2.67
Ho	0.01	0.49	0.47	0.37	0.54	0.49	0.56	0.59	0.51	0.53
Er	0.01	1.43	1.37	1.13	1.55	1.45	1.58	1.86	1.5	1.55
Tm	0.005	0.217	0.215	0.196	0.237	0.231	0.247	0.277	0.221	0.241
Yb	0.01	1.44	1.49	1.54	1.68	1.61	1.71	1.88	1.48	1.72

Lu	0.002	0.247	0.257	0.252	0.276	0.261	0.282	0.309	0.25	0.266
La/Yb		6.069	12.685	6.558	8.155	7.950	10.585	9.202	9.257	9.070
Sr/Y		63.143	11.600	41.083	41.857	532.250	52.444	29.882	420.000	102.438
Nb/Y		0.643	0.640	0.833	0.707	0.525	0.661	0.635	0.721	0.719
Zr/Ti		0.021	0.034	0.024	0.028	0.032	0.041	0.031	0.033	0.025
V/Sc		7.387	8.898	8.933	8.352	10.381	11.247	8.769	8.491	8.491
Eu <sub>N</sub> /Eu <sub>N</sub> *		0.938	1.037	1.114	1.063	1.140	1.569	0.996	1.103	1.011

Note: See the Digital Appendix Table A1 for sample locations.

**ocks at Red Chris**

RC13-32	RC13-33	RC13-83	RC13-77	RC13-78	RC13-62	RC13-79	RC13-97
P2L	P2L	P2L	P3	P3	Dike	Dike	Dike
57.57	56.05	57.38	58.47	57.45	46.23	49.38	54.17
17.22	16.51	17.38	17.67	17.34	15.25	14.12	14.32
6.41	6.09	6.8	5.02	6.31	9.15	11.39	8.66
0.13	0.107	0.116	0.066	0.11	0.108	0.168	0.19
2.28	1.85	1.72	1.34	1.89	4.41	3.21	2.9
5.66	6.6	6.04	4.84	6.1	7.78	7.3	5.72
3.27	3.12	3.19	4.29	3.17	1.23	2.66	3.32
4.03	3.01	3.8	2.3	3.15	2.84	1.63	2.14
0.444	0.418	0.536	0.432	0.436	1.25	2.008	1.608
0.28	0.3	0.3	0.28	0.32	0.44	0.39	0.62
2.33	4.36	3.13	5.51	4.03	10.85	7.97	5.61
0.296	0.053	0.155	0.633	0.112	0.231	0.255	0.092
99.63	98.4	100.4	100.2	100.3	99.53	100.2	99.28
1322	1323	1002	545	1232	343	614	1572
11.2	8.6	11.7	8	9.2	27.1	22.6	10.1
22.6	46.8	36	35.1	19.3	15.8	21.3	16.4
1.7	2.1	1.6	2.9	1.9	2.4	0.7	0.7
17	15	15	16	18	16	16	16
1.6	1.8	1.4	1.7	1.7	2.4	1.7	2
2.3	1.9	2.1	2.4	2.4	3	3.2	3.3
10.3	9.9	9.2	10.4	11.1	8.3	8.4	9.4
5	5	6	6	5	4	3	5
< 5	< 5	< 5	< 5	< 5	< 5	< 5	< 5
62	61	57	43	54	66	28	32
14.2	14.5	15.8	12.8	15.5	22.1	32	26.2
978	1083	985	737	800	668	447	507
0.69	0.79	0.6	0.75	0.74	0.54	0.53	0.56
74	86	88	91	75	131	132	138
2.3	1.9	2.1	2.4	2.4	3	3.2	3.3
1.46	1.71	1.27	1.74	1.38	1.01	1.34	1.89
3.48	3.01	2.7	3.45	3.26	1.8	2.39	3.46
129	130	148	122	132	221	480	129
17	14	15	18	16	23	27	36
66	52	60	36	50	84	99	111
74	86	88	91	75	131	132	138
0.06	0.24	0.2	0.14	0.08	0.61	0.14	0.17
16	14.3	13	16.2	15.5	14.3	16.1	20
31.4	27.4	26.1	31.9	31.5	30.3	34.9	42.4
3.54	3.3	3.26	3.64	3.64	4.16	4.75	5.84
14	11.7	12	14.3	15.1	16.2	18.4	23.8
3.22	2.4	2.51	2.96	2.78	3.9	4.28	5.57
0.958	0.798	0.818	1.1	1.01	1.56	1.46	2.56
2.91	2.14	2.28	2.69	2.7	3.98	4.64	5.8
0.46	0.39	0.41	0.42	0.46	0.74	0.84	1.06
2.8	2.47	2.59	2.48	2.88	4.73	5.29	6.78
0.55	0.5	0.52	0.49	0.57	0.95	1.12	1.4
1.61	1.5	1.56	1.46	1.7	2.57	3.19	4
0.243	0.226	0.241	0.23	0.251	0.369	0.467	0.581
1.71	1.57	1.68	1.6	1.71	2.42	3.14	3.82



0.282	0.265	0.264	0.281	0.294	0.391	0.465	0.597
9.357	9.108	7.738	10.125	9.064	5.909	5.127	5.236
57.529	77.357	65.667	40.944	50.000	29.043	16.556	14.083
0.606	0.707	0.613	0.578	0.694	0.361	0.311	0.261
0.027	0.033	0.027	0.033	0.028	0.016	0.010	0.014
9.085	8.966	9.367	9.531	8.516	10.000	15.000	4.924
0.951	1.070	1.039	1.185	1.120	1.203	0.996	1.369

---

**Table 3. Whole-rock Nd-Sr isotopic results for the porphyry and basaltic to andesitic dike rocks**

Sample	Rb ( $\mu\text{g/g}$ )	Sr ( $\mu\text{g/g}$ )	$^{87}\text{Rb}/^{86}\text{Sr}$	$^{87}\text{Sr}/^{86}\text{Sr}$	$\pm 2\sigma$	T (Ma)	$(^{87}\text{Sr}/^{86}\text{Sr})_T$	Sm ( $\mu\text{g/g}$ )	Nd ( $\mu\text{g/g}$ )
<b>P1 porphyry</b>									
RC13-39	44.10	640.50	0.199213	0.705022	0.000020	211.6	0.7044	2.29	9.96
RC13-40	36.38	96.01	1.096378	0.707480	0.000032	211.6	0.7042	2.94	15.77
<b>P2E porphyry</b>									
RC13-92	18.75	703.50	0.077095	0.704633	0.000019	206.0	0.7044	3.06	15.31
RC13-107	43.23	320.70	0.390074	0.705837	0.000037	206.0	0.7047	2.97	14.70
<b>P2L porphyry</b>									
RC13-32	27.07	509.50	0.153691	0.705103	0.000035	203.6	0.7047	2.65	12.77
RC13-33	47.40	846.00	0.162098	0.704873	0.000017	203.6	0.7044	2.63	12.87
<b>P3 porphyry</b>									
RC13-77	37.47	531.70	0.203855	0.704991	0.000016	201.7	0.7044	2.80	14.06
RC13-78	25.78	427.70	0.174403	0.704748	0.000024	201.7	0.7042	2.67	13.03
<b>Mafic to andesitic dike</b>									
RC13-97	23.90	385.10	0.179519	0.704792	0.000020	200.0	0.7043	6.22	25.72
RC13-79	15.73	252.40	0.180303	0.704741	0.000030	200.0	0.7042	4.81	20.18

Notes: <sup>1</sup>N/A = no data; the used ages for calculations are from zircon U-Pb dating results for porphyry rocks, and assuming  $T_{\text{DMI}} = (1/\lambda) \times \text{Ln}[\frac{(^{143}\text{Nd}/^{144}\text{Nd})_{\text{sample}} - (^{143}\text{Nd}/^{144}\text{Nd})_{\text{DM}}}{(^{147}\text{Sm}/^{144}\text{Nd})_{\text{sample}} - (^{147}\text{Sm}/^{144}\text{Nd})_{\text{DM}} + 1}]$ . See Appendix and depleted mantle. See the Digital Appendix Table A1 for sample locations.

### at Red Chris<sup>1</sup>

$^{147}\text{Sm}/^{144}\text{Nd}$	$(^{143}\text{Nd}/^{144}\text{Nd})_0$	$\pm 2\sigma$	$\epsilon_{\text{Nd}}(t = 0)$	$(^{143}\text{Nd}/^{144}\text{Nd})_T$	$T_{\text{DMI}} \text{ (Ga)}$	$\epsilon_{\text{Nd}}(T)$
0.139132	0.512732	0.000009	1.8	0.512540	0.88	3.4
0.112591	0.512672	0.000010	0.7	0.512516	0.74	2.9
0.120965	0.512659	0.000007	0.4	0.512496	0.83	2.4
0.122321	0.512700	0.000010	1.2	0.512535	0.77	3.2
0.125462	0.512713	0.000008	1.5	0.512546	0.78	3.3
0.123603	0.512713	0.000010	1.5	0.512548	0.76	3.4
0.120209	0.512686	0.000012	0.9	0.512527	0.78	2.9
0.123767	0.512727	0.000010	1.7	0.512564	0.74	3.6
0.146221	0.512751	0.000006	2.2	0.512559	N/A	3.5
0.144047	0.512766	0.000011	2.5	0.512578	N/A	3.9

200 Ma for basaltic to andesitic dikes based on geological relationship, see text for details.

ix 1 for the  $^{143}\text{Nd}/^{144}\text{Nd}$  and  $^{147}\text{Sm}/^{144}\text{Nd}$  values of present day chondrite

Table 4. Estimates of magmatic temperature and sulfur–chlorine content from igneous apatite and whole-rock compositions

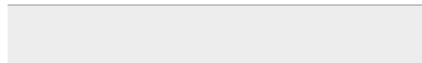
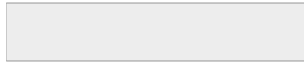
Porphyry Phase	Sample	Whole rock SiO <sub>2</sub> (wt. %) <sup>1</sup>	Whole rock P <sub>2</sub> O <sub>5</sub> (wt. %) <sup>1</sup>	AST <sup>2</sup> (°C)	Apatite SO <sub>3</sub> (wt. %) (n) <sup>3</sup> [maximum, minimum]	Apatite Cl (wt. %) (n) <sup>3</sup>	Apatite F (wt. %) (n) <sup>3</sup>	Apatite Molar S/Cl (n) <sup>3</sup>	Apatite Molar Cl/F (n) <sup>3</sup>	Average magmatic S content (wt. %) <sup>4</sup> [maximum]	Average magmatic S content (wt. %) <sup>5</sup> [maximum]	Average magmatic Cl content (wt. %) <sup>6</sup>
P1	RC13-39	59.93	0.31	921	0.11 ± 0.03 (34) [0.05, 0.19]	0.51 ± 0.3 (34)	3.64 ± 0.48 (34)	0.13 ± 0.08 (34)	0.08 ± 0.06 (34)	0.010 ± 0.003 [0.017]	0.002 ± 0.0004 [0.003]	0.63 ± 0.38
P2E	RC13-13 <sup>7</sup>	63.33	0.25	932	0.28 ± 0.10 (19) [0.11, 0.46]	1.47 ± 0.22 (19)	2.32 ± 0.29 (19)	0.09 ± 0.03 (19)	0.35 ± 0.10 (19)	0.030 ± 0.010 [0.050]	0.006 ± 0.004 [0.015]	1.84 ± 0.27
	RC13-107	59.25	0.30	909	0.32 ± 0.17 (15) [0.18, 0.80]	0.82 ± 0.10 (15)	2.36 ± 0.30 (15)	0.17 ± 0.09 (15)	0.19 ± 0.05 (15)	0.031 ± 0.017 [0.078]	0.014 ± 0.031 [0.012]	1.02 ± 1.13
P2L	RC13-26	58.08	0.30	892	0.30 ± 0.22 (48) [0.07, 1.2]	1.57 ± 0.33 (48)	2.23 ± 0.22 (48)	0.11 ± 0.20 (48)	0.39 ± 0.10 (48)	0.017 ± 0.013 [0.070]	0.0490 ± 0.2380 [1.6168]	1.96 ± 0.41
	RC13-33	58.61	0.31	905	0.28 ± 0.13 (52) [0.14, 0.79]	1.37 ± 0.17 (52)	2.40 ± 0.21 (52)	0.09 ± 0.04 (52)	0.31 ± 0.05 (52)	0.020 ± 0.009 [0.056]	0.008 ± 0.017 [0.117]	1.71 ± 0.21
P3	RC13-78	59.86	0.33	928	0.03 ± 0.01(13) [0.02, 0.05 ]	0.02 ± 0.02 (17)	3.60 ± 0.40 (17)	0.16 ± 0.09 (13)	0.01 ± 0.01 (17)	0.003± 0.001 [0.005]	0.001 ± 0.0001 [0.001]	0.12 ± 0.07

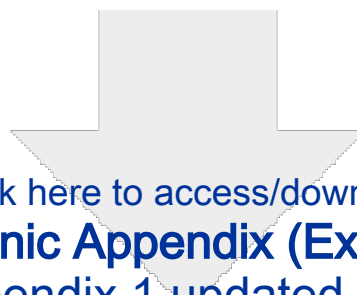
## Notes:

1. Normalized to 100 wt. % (Digital Appendix Table A3).
2. Apatite saturation temperature (AST) calculated from whole-rock SiO<sub>2</sub> and P<sub>2</sub>O<sub>5</sub> concentrations using the equation of Piccoli and Candela (1994).
3. Average of all igneous apatite analyses (Digital Appendix Table A8).
4. Estimated from apatite SO<sub>3</sub> contents (Digital Appendix Table A8) using the temperature-dependent apatite–melt partition coefficient formula of Peng et al. (1997):  
 $\ln K_D = 21130/T - 16.2$  (where T is in Kelvin).
5. Estimated from apatite SO<sub>3</sub> contents (Digital Appendix Table A8) using the temperature-dependent apatite–melt partition coefficient formula of Parat et al. (2011):  
 $SO_3 \text{ apatite (wt. \%)} = 0.157 \times \ln SO_3 \text{ glass (melt, wt.\%)} + 0.9834$  ( $r^2 = 0.62$ ).
6. Estimated from apatite Cl contents (Digital Appendix Table A8) using the apatite–melt partition coefficient value (mass ratios) of Mathez and Webster (2005), which is 0.8 for basaltic melt (51.1 wt. % SiO<sub>2</sub>) and tends to be similar for rhyodacitic melt at 200 MPa (Webster et al., 2009).
7. SiO<sub>2</sub> and P<sub>2</sub>O<sub>5</sub> compositions for this sample taken from sample RC13-92 with same lithology as RC13-13 but less altered (Digital Appendix Table A3).



Click here to access/download  
**Electronic Appendix (Excel etc.)**  
Appendix tables.xlsx





Click here to access/download  
**Electronic Appendix (Excel etc.)**  
Appendix 1 updated.docx

